NON-INTRUSIVE SENSING AND FEEDBACK CONTROL OF SERPENTINE INLET FLOW DISTORTION

Jason M. Anderson

Dissertation submitted to the Faculty of the
Virginia Polytechnic Institute and State University
in partial fulfillment of the requirements for the degree of

Doctor of Philosophy
in
Mechanical Engineering

Dr. Ricardo Burdisso, Co-Chairman
Dr. Wing Ng, Co-Chairman
Dr. Alfred Wicks
Dr. William Saunders
Dr. Jeffrey Borggaard

April, 2003
Blacksburg, Virginia

Keywords: Active Flow Control, Inlet Flow Distortion, Adaptive Filtering,
Wall-pressure Fluctuations

Non-Intrusive Sensing and Feedback Control of Serpentine Inlet Flow Distortion

Jason Anderson

(ABSTRACT)

A technique to infer circumferential total pressure distortion intensity found in serpentine inlet airflow was established using wall-pressure fluctuation measurements. This sensing technique was experimentally developed for aircraft with serpentine inlets in a symmetric, level flight condition. The turbulence carried by the secondary flow field that creates the non-uniform total pressure distribution at the compressor fan-face was discovered to be an excellent indicator of the distortion intensity. A basic understanding of the secondary flow field allowed for strategic sensor placement to provide a distortion estimate with a limited number of sensors. The microphone-based distortion estimator was validated through its strong correlation with experimentally determined circumferential total pressure distortion parameter intensities (*DPCP*).

This non-intrusive *DPCP* estimation technique was then used as a *DPCP* observer in a distortion feedback control system. Lockheed Martin developed the flow control technique used in this control system, which consisted of jet-type vortex generators that injected secondary flow to counter the natural secondary flow inherent to the serpentine inlet. A proportional-integral-

derivative (PID) based control system was designed that achieved a requested 66% reduction in *DPCP* (from a *DPCP* of 0.023 down to 0.007) in less than 1 second. This control system was also tested for its ability to maintain a *DPCP* level of 0.007 during a quick ramp-down and ramp-up engine throttling sequence, which served as a measure of system robustness. The control system allowed only a maximum peak *DPCP* of 0.009 during the engine ramp-up. The successful demonstrations of this automated distortion control system showed great potential for applying this distortion sensing scheme along with Lockheed Martin's flow control technique to military aircraft with serpentine inlets.

A final objective of this research was to broaden the non-intrusive sensing capabilities in the serpentine inlet. It was desired to develop a sensing technique that could identify control efforts that optimized the overall inlet aerodynamic performance with regards to both circumferential distortion intensity *DPCP* and average pressure recovery *PR*. This research was conducted with a new serpentine inlet developed by Lockheed Martin having a lower length-to-diameter ratio and two flow control inputs. A cost function based on *PR* and *DPCP* was developed to predict the optimal flow control efforts at several Mach numbers. Two wall-mounted microphone signals were developed as non-intrusive inlet performance sensors in response to the two flow control inputs. These two microphone signals then replaced the *PR* and *DPCP* metrics in the original cost function, and the new non-intrusive-based cost function yielded extremely similar optimal control efforts.

Acknowledgements

I would like to express my extreme gratitude to my research advisors, Dr. Burdisso and Dr. Ng. Without their support the successes of this research would not have been possible, and more importantly my maturation as a researcher would not have been possible. In similar fashion, the guidance and insights provided by Dr. Wicks, Dr. Saunders, and Dr. Borggaard were greatly appreciated. Lockheed Martin's role in this research was vital in that they provided the test inlet, active flow control technique, and an inlet test facility. This research was funded in majority by the Air Force Research Laboratories, and I consider myself fortunate to have worked for the most supportive AFRL program manager, Mr. Skip Gridley. I would like to thank the employees of Techsburg for all of their technical support in this research. I am especially grateful for the research contributions from my research colleague Angie Rabe, who helped in obtaining some of the aerodynamic data presented in this dissertation. I would also like to thank my fellow graduate students who provided sound advice over the past three years: Jinwei Feng, Todd Bailie, Leonardo Molisani, and Jose Alonso.

Most importantly I wish to express my extreme gratitude to my parents. I would not be at this point in my life without their love and support. While enduring the day-to-day struggles with this research, my girlfriend, Karen, provided the love and inspiration that carried me to the completion of this dissertation. Finally, I want to thank Michael James for his friendship and support throughout our years of college together.

Contents

List of Figures

List of Tables

Nomenclature

AIP	Aerodynamic Interface Plane, exit plane of inlet where measurements are obtained
A_v	Signal gain of Amplifier
A/D	Analog-to-Digital
D/A	Digital-to-Analog
DC	Direct Current
b	Gradient calculated from gradient-searching algorithm
b_{cr}	Critical gradient upon which a control decision D_i is based
$D(z)$	Discrete Controller Transfer Function
D_i	Decision of gradient searching control algorithm
$DPCP$	Circumferential Distortion Intensity According to SAE 1420
DSP	Digital Signal Processor
e	Error Signal
$E[\cdot]$ or $\langle\cdot\rangle$	Expected Value or Average
f_n	Acoustic Natural Frequency
F	Drift Term in Plant Dynamic Model
FIR	Finite Impulse Response
FRF	Frequency Response Function
g_{ss}	Steady-state Gain
G_{xx}	Autospectrum of Signal $X(f)$
G_{xy}	Cross-spectrum of Signals $X(f)$ and $Y(f)$
$G(s)$	Transfer Function of Plant
H	Wall-pressure-based Distortion Observer (units of Volts)
$\tilde{H}$	Wall-pressure-based Distortion Observer (units of Pa^2)
H_1	Microphone measurement from Array 1 in Optimal Inlet Performance Sensing Technique
H_2	Microphone measurement from Array 2 in Optimal Inlet Performance Sensing Technique
HCF	High Cycle Fatigue
J	Inlet Performance Cost Function (based on PD and $DPCP$)

p'_w .....Wall-pressure fluctuation

PID .....Proportional-Integral-Derivative Control Algorithm

K_P, K_I, K_D .....Proportional, Integral, and Derivative Control Gains

LMS .....Least Mean Square

M .....Mach Number

MSE .....Mean Square Error

PD .....Average AIP Pressure Deficit

PR.....Average AIP Pressure Recovery

Q_x , Q_u.....State and Control Weighting Coefficients in J

q_1 , q_2 , q_3 , q_4 .....Weighting Coefficients in J

$q(x,y,z,t)$.....Spatial distribution of turbulent pressure sources as a function of time

R .....Resistor

$R(\tau)$.....Autocorrelation Function

R^2.....Pearson Product Moment Correlation Coefficient (agreement of linear curve-fit)

RMS .....Root-Mean-Square

SISO.....Single-Input, Single-Output System

s .....Microphone sensitivity

s_k.....Output Signal from Adaptive Filter

Δs .....Span-wise Microphone Spacing

S.....Step size in gradient-searching control algorithm

std. dev. .....Standard deviation

TBL.....Turbulent Boundary Layer

T_s .....Settling Time

$\tilde{u}$ .....Instantaneous Velocity

U.....Average Velocity

u' .....Fluctuating Velocity Component

u_x,u_y .....x and y velocity components

$U(s)$ .....Control Signal Laplace Domain

u_{fwd}.....Forward Affecter Control Effort (% by mass)

u_{aft}.....Aft Affecter Control Effort (% by mass)

V ..... Voltage Signal

VDC ..... Direct Current Voltage

VG ..... Vortex Generator

$\underline{w}_k$ ..... Vector of Adaptive Filter Weights

$\underline{w}_o$ ..... Vector of Optimal Adaptive Filter Weights

x_k ..... Auxiliary Signal in Adaptive Filter Network

y_k ..... Primary Signal in Adaptive Filter Network

y_1 ..... Feedback signal associated with u_{fwd} in Optimal Inlet Performance Sensing Technique

y_2 ..... Feedback signal associated with u_{aft} in Optimal Inlet Performance Sensing Technique

∇ ..... Gradient Operator

∇^2 ..... Laplacian Operator

Λ ..... Turbulence integral length scale

ℓ ..... Large-scale turbulence length scale

ε ..... Rate of Turbulent kinetic energy dissipation

η ..... Kolmogorov microscale

μ ..... Step size of Steepest Descent Algorithm to Determine MSE

$\gamma^2_{x,y}$ ..... Ordinary Coherence between signals $X(f)$ and $Y(f)$

τ_w ..... Shear Stress at the Wall

ζ ..... System damping ratio

ω_n ..... System natural frequency

Ω ..... Resistance

Chapter 1

Introduction

This chapter presents the background information and motivation for the research presented in this dissertation. First, the serpentine inlet design is addressed in Section 1.1. Stealth characteristics are presented as the prime motivation for serpentine jet-engine inlet designs. Then the aerodynamic drawbacks of the serpentine inlets are discussed. Section 1.1 concludes with the active flow control techniques that have been shown to greatly improve the inlet airflow quality. In Section 1.2 the motivations and objectives of this research are presented. Finally, Section 1.3 outlines the organization of this dissertation.

1.1 Serpentine Inlets

1.1.1 Purpose of Serpentine Design

Prior to the mid 1980's aerodynamic performance was emphasized in inlet designs for military aircraft [1]. The inlet aerodynamic performance was characterized by its efficiency (total pressure recovery and installed drag) and engine compatibility (distortion and turbulence). In recent years the military has transferred the inlet design emphasis from aerodynamic performance to aircraft survivability. Survivability referred to bringing back pilots and aircraft intact, and survivability has been improved through the implementation of stealth technologies. Past stealth designs have included the use of irregular surface designs, radar absorbent paint, engine exhaust scattering, and enclosed weapons bays to reduce the aircraft radar cross-section. Despite all these stealth advancements aircraft are still detectible by the rotating components of the jet engine. Serpentine inlet designs arose from the necessity to hide the jet engine's rotating blades from enemy radar.

Inhibiting a direct line-of-sight into the jet engine for radar beams serves as the major design premise for the serpentine inlet. Radar beams entering a serpentine diffuser undergo a series of reflections on the highly curved inner walls of the duct. A radar absorbent paint lines the inner walls of the serpentine inlet to dissipate the radar beam's energy with each reflection preventing escape of the beam back to the enemy receiver for possible detection [2].

Moreover, the serpentine inlet design provides several aerodynamic benefits as well as operation cost savings. The serpentine inlet design shortens the length of the diffuser, thereby reducing the overall length of the aircraft, which has produced an air vehicle with lower life cycle costs [3]. Shortening the aircraft provides two major benefits: improved maneuverability and lowered operation costs. Improved maneuverability results directly from the reduced inertial properties associated with this compact design. The reduced operation costs result from improved fuel economy associated with the light weight design.

1.1.2 Effects of Flow Distortion on Engine Performance

While serpentine inlets increase survivability by reducing aircraft radar cross-section, they unfortunately also introduce engine operability and performance penalties. The aggressively curved flow paths through these diffusers spoil the air ingested by the engine compressor. Serpentine diffusers deliver a non-uniform (distorted) airflow to the compressor as indicated by the total pressure recovery contour [4] (Figure 1.1, low pressure recoveries in dark blue), which consists of total pressures measured at the exit plane of a serpentine inlet.

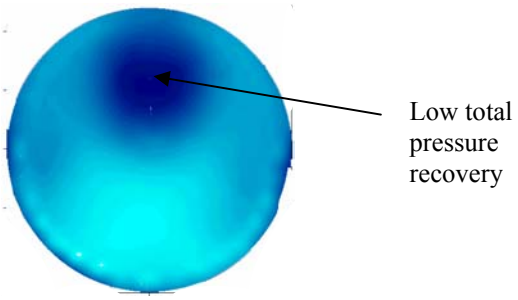

Figure 1.1: Serpentine Inlet Exit-Plane Measured Total Pressures Normalized by Stagnation Pressures Upstream of Inlet

Compressor blades are loaded and unloaded with every rotation in the presence of a distorted flow field. Since jet engine compressors spin at high angular rates (15-23 kRPM), the loading cycles on the blades increase rapidly, which leads to high cycle fatigue (HCF) blade failure. In the past decades, it has been cited that 55% of the United States Air Force's engine-related mishaps and 30% of the total maintenance cost was related to HCF. In fact the United States Air Force estimated an expenditure of about $100 million each year to inspect and repair HCF related problems [5]. In addition to the damaging effects on the compressor blades, distortion degrades the overall performance of the jet engine. The distorted airflow delivered to the compressor promotes the onset of a flow breakdown at the compressor blades in that particular sector. This flow breakdown phenomenon is known as stall, and in severe cases can develop into a rotating stall that degrades the operation of the entire compression system. Once the entire compression becomes affected a flow stoppage or a flow reversal known as surge is imminent if the pressure ratios are smaller than the design compressor ratio [6]. Since the aerodynamic factor of safety is low with serpentine inlets, they are currently only being considered for installation in unmanned aircraft. A typical Unmanned Combat Air Vehicle (UCAV) proposed for the US Navy that incorporates a serpentine inlet design into the top of the aircraft is shown in Figure 1.2. In order to reap the stealth benefits from the serpentine design, the flow distortion mechanisms must be understood in order to sense and control this problem.

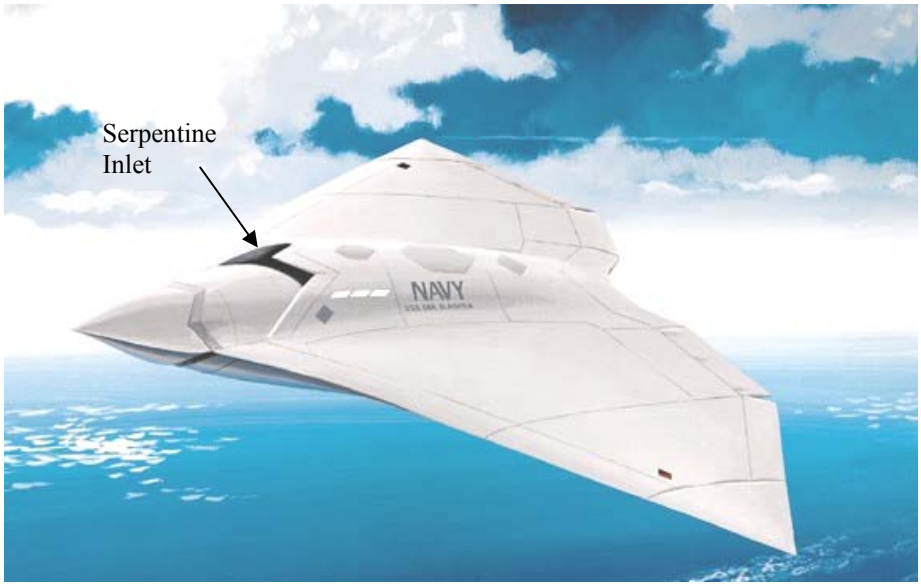

Figure 1.2: Serpentine Inlets Considered for Unmanned Combat Air Vehicle (UCAV)

1.1.3 Causes of Flow Distortion

There are primarily two fluid mechanisms that create distorted total pressure distributions at the outlet planes of serpentine inlets, turbulent boundary layer (TBL) separation and secondary flow development. The TBL separation phenomenon and its effect on total pressure losses will be discussed first since it is easier to understand. Diffusers are designed to create adverse pressure gradients, which are sufficient alone in causing a boundary layer to separate. A half-section view of a serpentine inlet along with a view of the inlet exit-plane looking downstream is shown in Figure 1.3 highlighting the curvature of the inlet. The aggressive flow curvature in the serpentine inlet causes the TBL to separate just downstream of the major bend in the inlet (Figure 1.3). As a result of the TBL separation, the low-momentum TBL fluid is afforded the ability to interact with a large region of the free-stream flow. Consequently, a large region of

low total pressure flow results at the inlet exit-plane (Figure 1.3), which creates a non-uniform pressure field for the compression system to ingest.

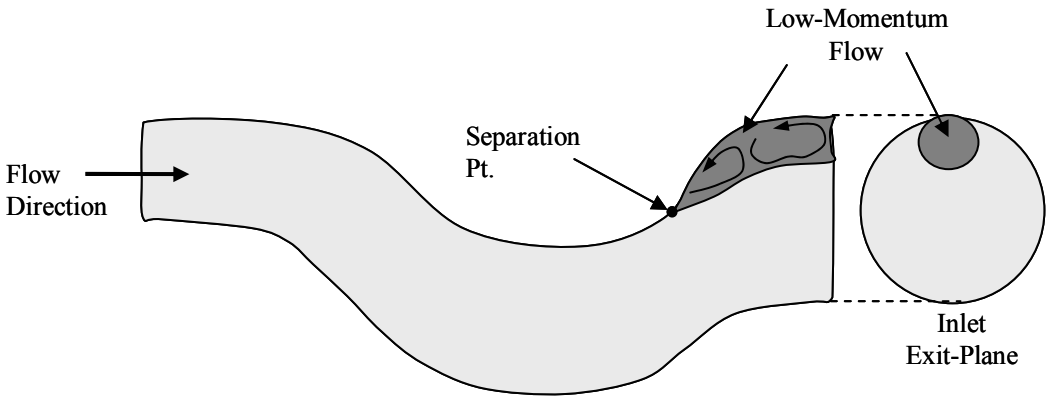

Figure 1.3: TBL Separation in Serpentine Inlets

Secondary flow was labeled as the other primary contributor to the creation of total pressure distortion in serpentine inlets. Due to tangential accelerations, as governed by the normal component of Euler's equation of motion, the high-momentum flow will move toward the outside wall of a bend, and the low-momentum flow will tend toward the inside of a flow bend [7]. A complete analysis of this phenomenon is located in Appendix A. This migration of flow normal to the axial flow velocity characterized by a vortical flow pattern is known as secondary flow. The three major bends of the serpentine inlet design are shown in Figure 1.4. The secondary flow effects can be analyzed at each of the three bends in the serpentine inlet (Figure 1.4). Then the secondary flows from each bend can be superimposed to yield the resulting secondary flow pattern at the inlet exit-plane, which is shown in Figure 1.5.

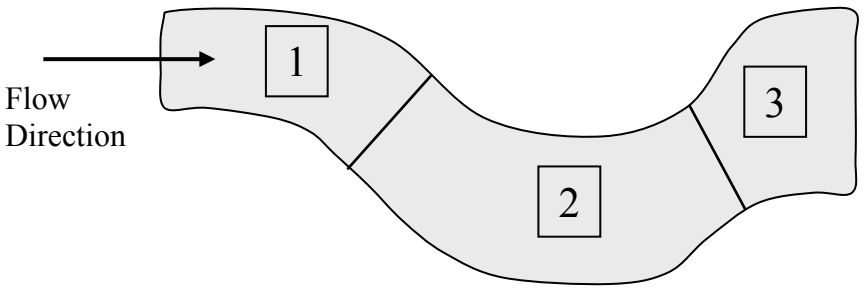

Figure 1.4: Bends in Serpentine Inlet that Create Secondary Flows

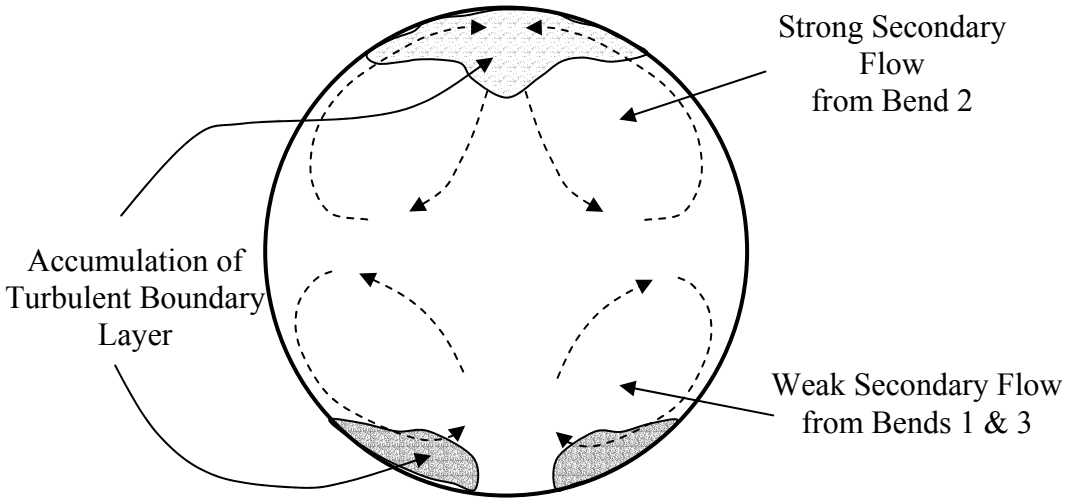

Figure 1.5: Secondary Flow Field at the Inlet Exit Plane

This secondary flow analysis reveals the accumulated regions of low-momentum, TBL flow at the inlet exit plane. The low-momentum flow from bend 2 combines with the separated flow yielding the large sector of low total pressure flow at the top-center portion of the inlet exit plane (Figure 1.5). Secondary flow analysis also provides an explanation of the low total pressures measured in the lower half of the exit plane, which are caused by secondary flows originating in

bends 1 and 3 (Figure 1.5). This understanding of secondary flow development provided a basis for recently implemented flow control techniques

1.1.4 Secondary Flow Control Technique

As it is currently understood, the secondary flow development as described in Section 1.1.3 is the primary contributor to the distorted flow pattern that serpentine inlets deliver to the compressor. In light of this knowledge, recent flow control concepts have proposed methods of thwarting secondary flow development. These flow control concepts were based on creating a secondary flow that counters the secondary flow inherent to the serpentine duct using vortex generators (VG's). The first generation of vortex generators (VG's) consisted of an array of vanes mounted on the inner surface of the serpentine duct [8]. Much effort was devoted toward determining the vane VG design (vane height, angle of incidence, and streamwise location) that yielded optimal distortion reduction over a wide range of Mach numbers. Despite the robust flow control abilities of vane-type VG's to provide favorable distortion reduction over a fairly wide range of Mach numbers, the thrust of the secondary flow control research turned toward jet-type vortex generators that could be adjusted to provide optimal control for any given Mach number [9]. Another motivation for departing from the vane-type VG approach was their added radar signature associated to intrusion into the duct. The effectiveness of the jet-type flow control technique in removing the large spoiled airflow in the top-center region of the inlet exit plane can be seen from the total pressure recovery contours with 1% flow control and without flow control shown in Figure 1.6 [10]. The orientation of the control air vorticity is designated by the red arrows in Figure 1.6 (b). These control air vortices spin in the opposite direction of the naturally occurring vortices in order to reduce the overall magnitude of the secondary flow in

the inlet. With the strength of the secondary flow reduced by the flow control, the low-momentum flows on both sides of the inlet do not converge at the top-center of the inlet exit-plane. The terminal angular position of the low-momentum flow was approximately 30^{o} for the 1.0% flow control scenario (Figure 1.6 (b)). The mass flow rate delivered to the jet-type VG's determined the vorticity strength of the secondary flow control. It should also be noted that this flow control technique maintains TBL attachment by mixing high and low momentum flows upstream of the usual point of separation.

Since this flow control method could be adjusted as needed, the need arose for an automated system that could detect the distortion intensity and appropriately control the vorticity of the VG's. The major obstacle to overcome in developing such a control system was finding a sensor that could detect the distortion intensity without disturbing the inlet airflow. The research presented in this dissertation provides a non-intrusive sensor that can close the loop of an automated distortion control system.

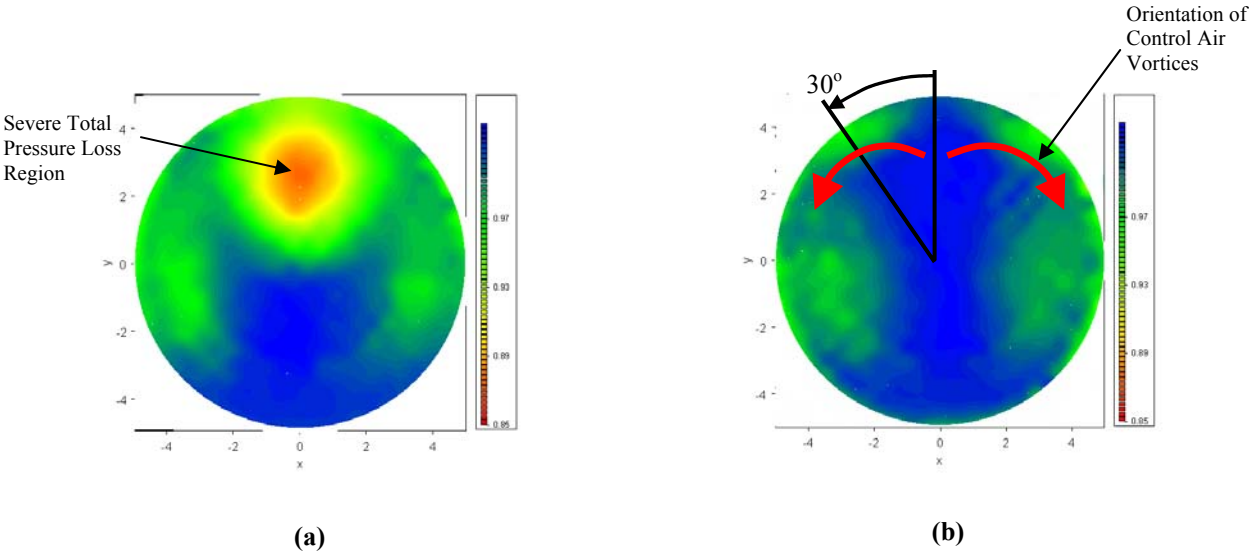

Figure 1.6: Total Pressure Recovery at Inlet Exit Plane with **(a)** no Flow Control and **(b)** 1.0% Flow Control; Low Pressure Recoveries are in Red

1.1.5 Non-Intrusive Sensor Options

Past efforts to non-intrusively sense serpentine inlet distortion were based on the location of the TBL separation point. A separation location further upstream was suggested to correlate with higher degrees of distortion [11], because the TBL would interact with the mean flow over a longer length of the flow path. There are several drawbacks with this sensing approach: the separation phenomenon only partially explains the distortion levels as described in Section 1.1.2, and the number of sensors required to locate the separation location could reach an unmanageable amount [12]. The most accurate method of detecting a separation point is to locate the minimum wall shear stress. The near-wall velocities in the vicinity of a boundary layer separation location are shown in Figure 1.7, as well as the wall shear stress magnitude at this singularity point.

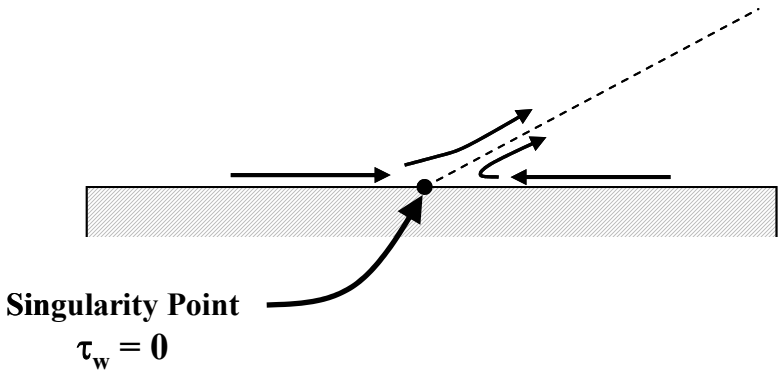

Figure 1.7: Locating a TBL Separation (Singularity) via Wall Shear Stress

The minimum wall shear stress indicates the singularity where the near-wall low velocity fluid both upstream and downstream is forced toward the separation [12] (Figure 1.7). Past applications of wall shear stress sensors to locate separation points in serpentine inlets have

required hundreds of wire film sensors and immense efforts in the signal processing to extract the singularity point.

A sensing approach that required less sensors and signal processing was desired; as a result, the separation location technique was abandoned. Thus, this research was based on studying the capabilities of using wall-pressure fluctuation measurements obtained at the inlet exit-plane to describe the non-uniformity of the total pressure field here. It is commonly known that large-scale turbulence provides a measure of the mean flow energy dissipation [13]. An array consisting of a minimal number of microphones could be placed at the inlet exit plane to determine which sectors contained the lowest total pressures. The relative microphone measurements could provide an indication of total pressure spatial distortion.

1.2 Motivations and Objectives of the Research

1.2.1 Research Motivations

As described earlier, jet-type VG's provide the ability to deliver the appropriate control effort to minimize distortion over a wide range of Mach numbers. Since the jet engine compressor would serve as the high pressure air supply for the jet-type VG, the required bleed

air to operate the flow control system needed to remain below 2% of the total air mass flow through the propulsion system. Recent developments have produced a feasible jet VG that now requires less than 2% of the propulsion system's total air mass to achieve 70% reductions in distortion intensity for all Mach numbers below 0.7 [9].

Now with this jet-type flow control technique proven to be feasible, it became imperative to find a sensor that could provide distortion intensity feedback to an automated system controlling the jet VG's. The major stipulation on the sensor was that it could not protrude into the inlet airflow, because it would create even more distortion by its presence. A sensor was needed that could infer the distortion within the flow merely from the wall measurements. In addition to this task, the sensor would need to demonstrate a quick response to the ever-changing flow environments inside inlets of highly maneuverable military aircraft. If such a sensor could be developed to operate in conjunction with the jet-type VG flow control technique, then and only then, could the many advantages provided by serpentine inlets be realized in military aircraft.

1.2.2 Research Objectives

A primary objective of this research is to develop a non-intrusive sensing technique that infers the distortion levels at the exit-plane of serpentine inlets. Wall-pressure fluctuation measurements will be investigated for their ability to indicate bulk flow quantities. The key components of the measured turbulence related to total pressure losses are to be identified and used to develop a measurement that infers the circumferential total pressure distortion *DPCP*

[14]. To use this wall-pressure fluctuation distortion indicator in an automated distortion control system, this signal needs to be simple enough that it can be computed by a digital signal processor in real-time. This design limitation requires strategic sensor placement in order to capture the distortion intensity with a minimal number of sensors. In addition the algorithm used to compute this distortion estimator signal should not be computationally intensive in light of digital signal processor limitations. Finally, this distortion estimation signal should be repeatable, or statistically stationary, in order to increase reliability.

Of equal importance to the non-intrusive distortion sensor development, another primary objective of the research is to demonstrate an automated distortion control system. There is no literature open to the public indicating a prior demonstration of a closed-loop system to control distortion, thus this closed-loop control system demonstration will be a major contribution to the airframe design community. In developing this active flow control system, the following elements need to be addressed: integration of feedback signal processing hardware, development of actuator system to operate the jet-type VG's, and finally integration of the digital signal processor containing the control algorithms with all other system components. This distortion control system will be tested for its response time to sudden desired distortion level changes and for its ability to maintain desired distortion levels while the inlet airflow velocity is quickly accelerated and decelerated.

The final objectives of this research are associated with advanced applications of this non-intrusive sensing technique. A wall-pressure based technique is to be developed that senses the flow improvements from two jet-type VG arrays installed in a serpentine inlet. Along with

this multiple control input sensing study, an optimal sensing scheme is to be developed that considers the improvements in distortion and average pressure recovery at the expense of the flow control demand.

1.3 Dissertation Outline

The remaining chapters of this dissertation are organized in the following manner.

Chapter 2 describes the experimental setup and research facilities used to conduct the active flow distortion control experiments. The experimental setup is presented to provide a reference to all components used in this research to sense and characterize serpentine inlet flow distortion. The primary research facilities include a stereo lithograph test inlet manufactured by Lockheed Martin, an Allied Signal F109 jet engine that pulls air through the inlet, and digital controllers.

Chapter 3 presents the basic concepts of wall-pressure fluctuation measurements and how they can detect inlet flow distortion. The transfer of mean flow energy down through progressively smaller turbulence length-scales is discussed, and large-scale turbulence is shown to be the key indicator of mean flow total pressure losses. Wall-pressure fluctuation

measurements are presented that support this fact. Finally, a signal from a combination of wall-pressure fluctuation sensors is presented that infers distortion intensity *DPCP*.

Chapter 4 presents an automatic distortion intensity control system that uses the wall-pressure distortion estimator developed in Chapter 3 as feedback. The system dynamic modeling is presented to serve as a basis for the control algorithm design. Finally, the successful control system demonstration results are presented.

Chapter 5 presents advanced wall-pressure-based techniques to infer inlet aerodynamic performance. A wall-pressure sensing technique is developed to measure the flow improvements from two flow affecters, as opposed to one flow affecter described earlier. This new sensing technique provides the capability of detecting the optimal control efforts from the two flow affecters. Another distinct advantage in this advanced sensing technique is that it is independent of Mach number. While resources for a closed-loop control system demonstration were not available, the architecture for a MIMO control system is proposed for future work.

Chapter 6 provides a summary of the major contributions from this research. A discussion on the possible future work of this sensing and control technique is also included.

Chapter 2

Research Facilities

This chapter describes the experimental setup and the important components of the research facility that were used for the sensing and control experiments in this research. First, the experimental setup is introduced in Section 2.1 in order to provide an overall view of the inlet test facility. The ensuing sections of the chapter describe the individual components of the facility in further detail. Section 2.2 describes the serpentine inlet equipped with the jet-type VG flow affecters designed and fabricated by Lockheed Martin. Then in Section 2.3 the jet engine that draws the airflow through the inlet test section is described. The aerodynamic and wall-pressure measurement techniques are then explained in Section 2.4. The flow control air supply

and delivery system is presented in Section 2.5. Finally, the capabilities of the digital signal processing board are presented in Section 2.6.

2.1 Experimental Setup

This experimental setup was constructed for the purpose of measuring the effects of active flow control in reducing spatial total pressure distortion in serpentine inlets. A schematic of this facility is presented in Figure 2.1.

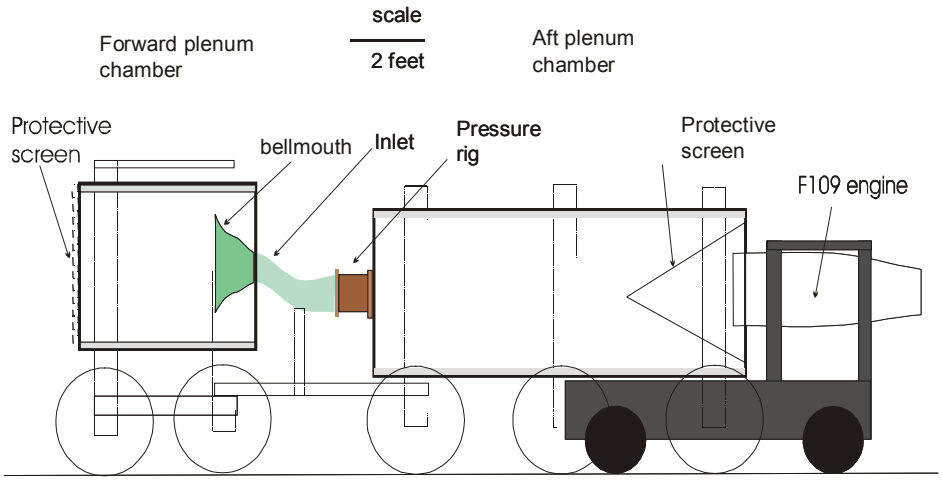

Figure 2.1: Schematic of Test Facility

This test facility is essentially a continuously-running wind tunnel that accommodates large test sections. In the case of these experiments, the test section was a serpentine inlet designed and

fabricated by Lockheed Martin Aeronautics, Co. An Allied Signal F-109 turbofan jet engine stationed at the rear of the facility pulled airflow through the inlet. By using a jet engine as the source for this wind tunnel, experiments could be conducted continuously over a span of several hours; as opposed to blow-down wind tunnels that provide only a 10 second window for data collection.

This facility was housed in a chamber with overhead doors at the front and rear that allowed for ambient air to enter the wind tunnel and the jet engine to exhaust into the ambient air at the rear. Since this was an outdoor facility, the facility could not be operated during inclement weather or even high relative humidity because moisture would collect in the total pressure probes and bias the measurements. However, the wall-pressure fluctuation measurements were determined to be insensitive to the ambient relative humidity, which is an essential attribute for implementing this sensing technology into aircraft. As seen in Figure 2.1, the serpentine inlet was mounted between two large plenum chambers. The forward plenum chamber prevented the ingestion of ground vortices and helped to straighten the airflow before it entered the inlet. Protruding into the front plenum chamber, the inlet bellmouth provided a smooth transition for the airflow to enter the inlet from the plenum chamber. This cylindrical forward plenum chamber was 5-feet long and 4-feet in diameter. Downstream of the inlet, the aft plenum chamber coupled the inlet to the jet engine. This cylindrical plenum was 10-feet long and 4-feet in diameter. Since the inlet exit plane diameter was 10-inches and the jet engine diameter was 20-inches, the aft plenum was designed to diffuse the inlet exhaust jet to ensure that this exhaust jet did not impinge only on the center of the jet engine intake. The aft plenum was constructed of 1/2-thick steel in order to withstand the 2-psi vacuum created inside the plenum. Finally, a

protective cone-screen was installed in front of the engine to prevent the ingestion of foreign objects into the engine.

The exit plane of the serpentine inlet served as the artificial compressor fan-face cross-section. As this would normally be the plane at which the compressor would be stationed, the total pressure measurements were obtained at this aerodynamic interface plane (AIP) to characterize the distorted flow that would enter the compression system. A straight, steel duct section was inserted here to mount and operate the pressure measurement instrumentation (Pressure Rig in Figure 2.1). The measure instrumentation inserted into the pressure rig along with the other important facility devices will be explained in further detail in the subsequent sections of this chapter.

2.2 Inlet

As mentioned before the serpentine inlet test article used in this research was designed and fabricated by Lockheed Martin Aeronautics, Co. This test article was fabricated via a stereo lithographic rapid prototyping process in several sections that were bolted together to form the entire inlet. The inlet used in this research could not be presented due to proprietary restrictions, but an older generation test article constructed in a similar manner is pictured in Figure 2.2.

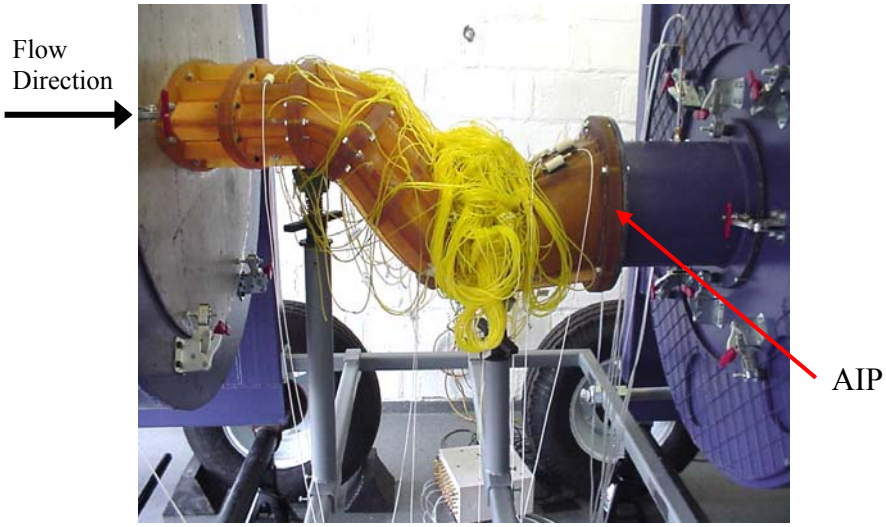

Figure 2.2: Older Generation Serpentine Inlet Test Article

The inlet shown in Figure 2.2 was equipped with vane-type VG flow affecters, but the current inlet was equipped with jet-type VG flow affecters. The air supply was delivered through two orifices on either side of the inlet. This high pressure air was stagnated in a small plenum incorporated into the wall of the inlet to ensure that equal mass flow rates were ejected from each of the jet holes in the VG jet array. Static pressure taps were installed at various locations down the length of the inlet to monitor the airflow. The microphone measurements at the AIP were also obtained via these static pressure taps.

2.3 Engine

This inlet test facility provided the unusual characteristic of being powered by a turbofan jet engine. A picture of the Allied Signal F109 turbofan jet engine mounted on its cart and inserted into the rear of the downstream plenum chamber is shown in Figure 2.3.

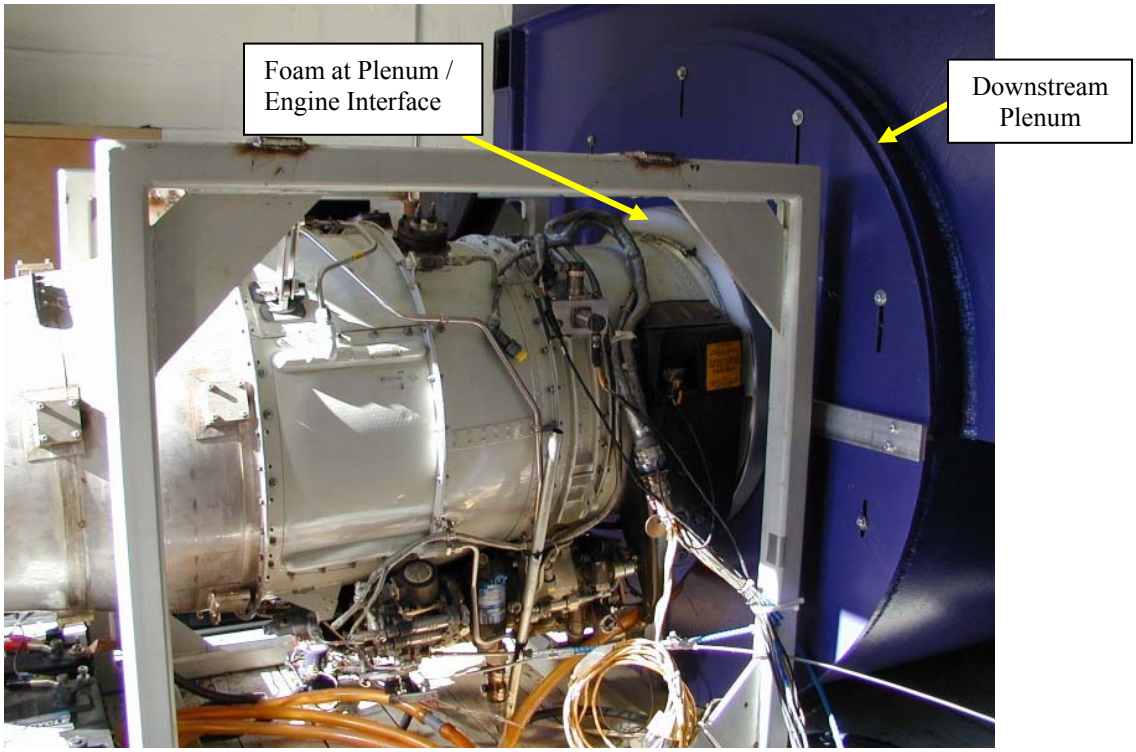

Figure 2.3: Allied Signal F109 Turbofan Jet Engine (flow from right to left)

In order to isolate the engine vibrations from the aft plenum and ultimately the brittle, stereo lithograph inlet, the engine was mounted onto a separate cart and inserted into an orifice at the rear of the aft plenum with a stiff foam providing the only physical contact between the engine

and the plenum(Figure 2.3). The Allied Signal F109 turbofan jet engine provided continuously operating suction to pull air through the inlet. The F109 engine produces 1330 lbs of thrust when breathing 23 lbm/sec of air at full throttle. This engine generates this power with a 5:1 bypass ratio, a 2-stage centrifugal compressor, and two stages of high-pressure and low-pressure turbines. The air is ingested through a 20-inch diameter intake [15]. With this engine the maximum continuous inlet throat Mach number achieved was 0.55. A variety of lower throat Mach numbers were achieved through the adjustment of a manual throttle.

2.4 Measurement Techniques

This section describes the total pressure measurement and wall-pressure fluctuation measurement techniques obtained at the AIP. The total pressure measurements were obtained to compute the inlet performance metrics *PR* and *DPCP*, which served as baseline performance indices upon which the wall-pressure fluctuation measurements were compared.

2.4.1 AIP Total Pressure Measurements

The flow quality delivered to the artificial fan-face plane (AIP) was characterized by a fine grid of total pressure measurements. The 20-Kiel-probe rake that was used to obtain the AIP total pressure measurements is shown in Figure 2.4.

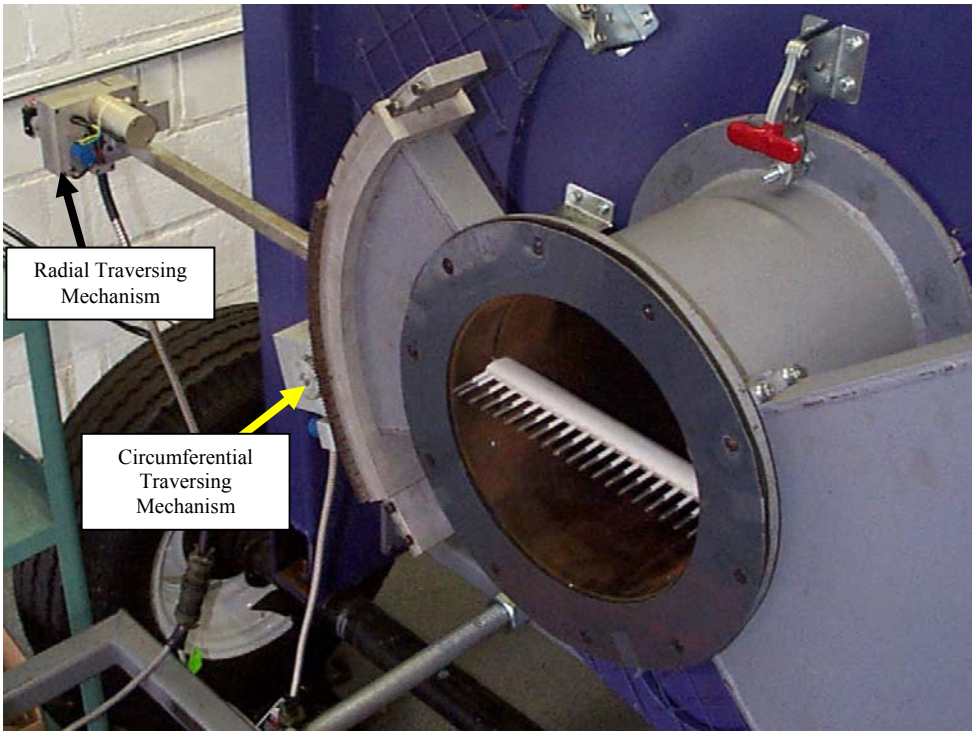

Figure 2.4: 20-Probe Rake with Circumferential and Radial Traverses for AIP Total Pressure Measurements

This 20-probe rake positions in the AIP were manipulated by motorized circumferential and radial traversing mechanisms. Traditional Pitot total pressure probes are sensitive to flow angularity. The Kiel probe design was chosen for its ability to sense total pressures even when the flow is at a large angle (more than 30^{o}) with respect to the tip of the probe.For each flow control effort and Mach number, the total pressure was measured at 720 locations within the 10-inch diameter AIP [10]. The total pressure measurements were obtained at 20 equally-spaced radial locations at 10^{o} circumferential intervals.

These total pressure measurements obtained for each combination of control effort and inlet throat Mach number were used to compute the inlet performance indices, average pressure

recovery *PR* and circumferential total pressure distortion *DPCP* [14]. The average pressure recovery is simply the average of all the total pressures measured at the AIP normalized by the stagnation pressure upstream of the inlet. This metric indicates the remaining total pressure at the AIP as a percentage of the airflow total pressure before entering the inlet. The *PR* provides a measure of efficiency for the inlet. The *DPCP* is slightly more difficult to compute, and its detailed explanation is unnecessary for the purpose of this discussion. Basically it characterizes the severity of the non-uniformity in the total pressure distribution in the circumferential direction. This metric is significant in that it characterizes the total pressure cyclic loading on the fan blades for each revolution. The *DPCP* can be used to explain HCF fan blade failure and reduced compressor surge margins.

2.4.2 Wall Microphone Measurements

This research utilized a novel approach in obtaining the wall-pressure fluctuation measurements. Typically when making wall-pressure fluctuation measurements a hole is drilled through the duct wall so that when a microphone is inserted its membrane is flush with the inner wall surface. Since the inside of the duct is inaccessible when assembled in the test facility, determining the flushness of the microphone membrane with the inner wall surface becomes extremely difficult. Because of this complication the microphones were not mounted flush to the wall for these experiments. The alternative microphone mounting approach is shown in

schematic form in Figure 2.5, and a photograph of this mounting technique is shown in Figure 2.6.

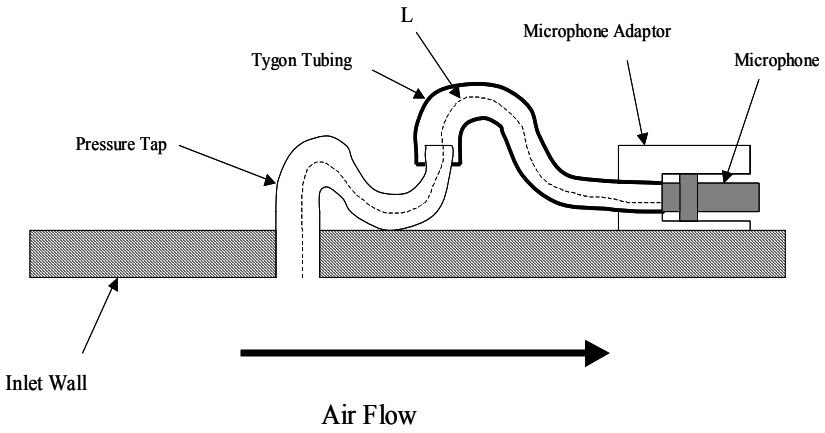

Figure 2.5: Connection of Microphone to Inner Wall Surface

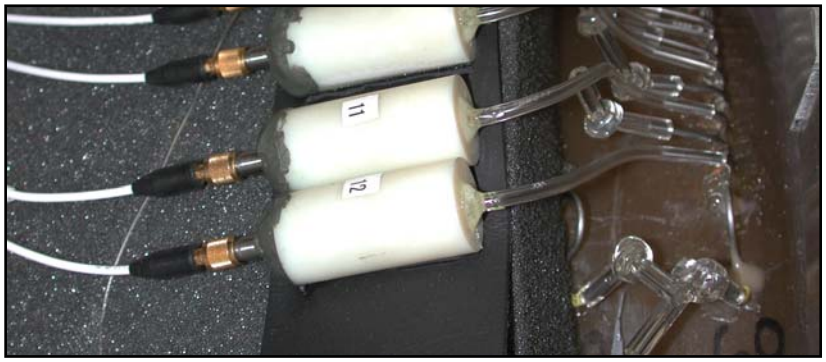

Figure 2.6: Picture of Microphone Measurement Technique

With the measurement techniques shown in Figures 2.5 and 2.6, the microphones sensed the wall-pressure fluctuations through plastic tubing connected to small pressure taps drilled into the inlet walls. A microphone adapter was fabricated to house the microphone and connect it with the plastic tubing that delivered the wall-pressure fluctuations to the microphone (Figure 2.5).

This adapter was simply a cylindrical piece of Delrin® bored on one end to allow for microphone insertion and drilled through the opposite end to allow for insertion of the plastic tubing. An adapter was dedicated to each microphone allowing each microphone to be moved with ease.

Several advantages became quickly apparent with the use of this measurement technique. The pressure tap orifice diameters were only 1.6-mm compared to the 13-mm diameter of a microphone membrane. This allowed for a higher sensor spatial resolution which usually plagues wall-pressure measurement experiments with flush-mounted sensors. Changing the sensor locations became as simple as moving the plastic tubing from one pressure tap to another taking only a few seconds. No detailed alignment was necessary as would be the case with a flush-mounted configuration. As for implementation into an actual aircraft inlet, these small pressure taps are much easier to position around the structural members of the inlet frame. Also, the use of the small pressure taps requires less material removal for each sensor installation, which allows for the installation of additional backup sensors for the event of a sensor failure. This tubing connection technique has one drawback, the tubes act as quarter-wave acoustic resonators. With this in mind the tubing length (L in Figure 2.5) was chosen to be 4-inches in order to yield a plane wave cut-on frequency of 800-Hz [16], which was above the bandwidth of interest.

2.5 Control Air Injection System

The entire control air injection system is shown in Figure 2.7. The air supply for this flow control system in an actual aircraft would be the low-pressure stage of the compressor. The option of bleeding air from the F109 compressor was considered, but the complications in conditioning this high temperature air and overworking the engine were not desired. As an alternative a Kaeser compressor was purchased to supply high-pressure for the VG jets. This screw-type compressor produces 82 scfm of air at 110 psi. This compressed air is stored in a 250-gallon storage tank, which provides a more constant delivery of air by its capacitance. The air is piped to the test facility through a 1.5-inch diameter 150-foot hose that produces a 40-psi pressure drop. The air mass flow rate was measured by the calibrated pressure drop across an orifice plate. The pneumatic valve that regulates the air mass flow rate was stationed downstream of the orifice plate. This pneumatic Mark 70 valve was actuated by a current-to-pressure transducer that received a 4-20 mA electrical signal for full range of operation. The air mass regulated by the valve then enters a 1-gallon plenum that equally splits mass flow to the two sides of the flow affecter plenum that is contained in the wall of the inlet.

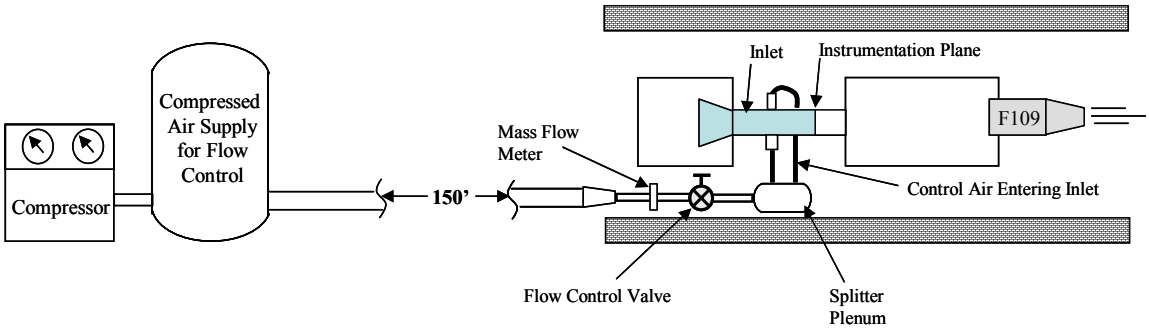

Figure 2.7: Flow Control Air Delivery System

2.6 Digital Signal Processing Board

The control algorithms for the distortion control system demonstrations were implemented with a digital signal processing board manufactured by Spectrum Signal Processing, Inc. The processor chip placed on this board was the TMSC320C30 manufactured by Texas Instruments. This processor operates with a 33.3 MHz clock capable of 33 million floating point operations per second when the floating point multiplier and adder are operated in parallel. The A/D and D/A boards are both 16 channels with 16-bit resolution. The input voltage range is ±2.5 Volts, and the output voltage range is ±8.2 Volts with very little associated amperage. The channels are grouped in sets of four for simultaneous sampling, and the four channel groups are multiplexed at a small delay of 3 μsec [17]. The DSP, A/D and D/A boards are all mounted in a host personal computer. Software was developed in C to provide menu-driven interaction with the DSP.

Chapter 3

Inferring Total Pressure Distortion from Wall-Pressure Fluctuations

This chapter describes the development of a wall-pressure fluctuation sensing technique that estimates *DPCP* at the exit-plane of serpentine inlets. The wall-pressure sensing technique was based on the basic flow physics in serpentine inlets. Section 3.1 identifies the large-scale turbulence as the mechanism that dictates mean flow total pressure losses. Section 3.2 presents the basic physics governing wall-pressure fluctuations. Section 3.3 then combines all the basic flow physics presented up to that point to support the placement of the microphones in identifying the total pressure distortion. Experimental results are also presented in this section that led to the development of a microphone signal capable of estimating *DPCP* for symmetric,

level flight conditions (i.e., symmetry distortion pattern at AIP). This sensing strategy is then statistically validated in Section 3.4, and then tested for its sensitivity to background acoustic noise in Section 3.5. Finally, Section 3.6 summarizes the key results from the development of this non-intrusive distortion sensing technique.

3.1 Turbulent Internal Flow Physics

The greatest total pressure losses occur in the regions of turbulent boundary layer accumulation and separated turbulent boundary layers. As this was the case, the fundamentals of turbulent flows were reviewed to determine the mechanisms by which total pressures are dissipated by turbulence. A key turbulent component responsible for total pressure loss was sought after. These turbulent components indicative of total pressure losses were to provide a basis for the wall-pressure sensing technique to infer total pressure distortion.

3.1.1 Coherent Turbulent Structures

The existence of turbulence within serpentine inlet airflows is practically guaranteed given the curvature of the flow path coupled with the intended flow speeds of Mach 0.5 to 0.7.

Recall that an instantaneous flow velocity measurement $\tilde{u}$ could be decomposed into an average velocity *U* and a turbulent fluctuating velocity *u'* according to

$$\tilde{u} = U + u' \tag{3.1}$$

In classical studies of fluid mechanics, there is little understanding of turbulent fluctuating velocities other than classifying them as random in nature. However, later in the 1970's and the 1980's it was recognized that turbulent flows contained dominant organized flow patterns, or more commonly coherent structures [18]. This concept of coherent turbulent structures provided an understanding of the flow mechanisms creating turbulence, which allowed for the development of turbulent flow control techniques. It was the objective of this research to base a non-intrusive distortion sensing technique upon the same basic fundamentals of coherent turbulent structure analysis that yielded prior flow control techniques.

Coherent turbulent structures vary in size and location within the flow field. For the most part, turbulence in internal flows is created near the walls of the duct, and tends to remain near the wall as the flow progresses downstream. Sizes of coherent turbulent structures are measured by the integral length scale Λ. The integral length scale is defined as:

$$\Lambda = U \int_0^{R(\tau)=0} R(\tau)\, d\tau$$
$$\text{where,} \quad R(\tau) = \frac{u'(t)\, u'(t+\tau)}{u'^2} \tag{3.2}$$

Combining the facts that the average of fluctuating velocities is zero and that $\lim_{\tau\to\infty} R(\tau) = \langle u' \rangle^2$, the upper limit of integration of equation 3.2 is the largest time lag τ that yields zero autocorrelation. For the purpose of this discussion the length scales defined by equation 3.2 will be subdivided into two categories as either being large-scale structures or small-scale structures. Large-scale structures are denoted as ℓ, and these large-scale structures fluctuate at low frequency. Large-scale structures are generally located near the potential flow at the outer part of the boundary layer, and this has been experimentally verified by the collapse of low frequency wall pressure fluctuation spectra when using a non-dimensional frequency scaled by the outer boundary layer variables [19]. At the other end of the spectrum, the smallest-scale structures are termed the Kolmogorov microscale and symbolized by η. Kolmogorov microscale turbulence fluctuates at relatively high frequencies and has been proven to exist close to the wall by the collapse of wall pressure spectra at high frequencies using a non-dimensional frequency scaled by the inner boundary layer variables [19]. As just described, wall pressure fluctuation measurements can be used to distinguish the turbulence levels attributed to large-scale turbulence and those attributed to small-scale turbulence. In light of this capability, an understanding of the effects each length scale has on energy extraction from the mean flow was needed to help build a basis for a wall-pressure fluctuation measurement method of detecting total pressure losses that cause distortion.

3.1.2 Mean Flow Energy Dissipation

The turbulent structures being carried along the length of the duct by the mean flow extract energy from the mean flow creating total pressure losses. It has been known that the lost total pressure is dissipated in the form of heat, but the process by which the energy reaches the point of dissipation has been somewhat a mystery. Recently Holmes et al. [18] has suggested that the energy is extracted from the mean flow by the large-scale, or energy-containing, turbulent structures. This energy then flows to the Kolmogorov microscale structures where the energy is dissipated in the form of heat. Holmes et al. [18] further adds that the common notion that viscosity dictates the amount of energy dissipation is invalid. Rather, flow energy dissipation is governed by the large, energy-containing turbulent structures. This point is quantified as

$$\varepsilon = u'^2 \left(\frac{u'}{\ell} \right) \tag{3.3}$$

where ε represents the dissipation rate of turbulent kinetic energy per unit mass. In words, the dissipation rate of turbulent kinetic energy is equal to the product of the turbulent kinetic energy (u'^2) and the inverse time scale $\left(\frac{u'}{\ell} \right)$ of the large-scale turbulence. In addition, most turbulent flows exist at an equilibrium state, where the rate of mean flow energy extraction rate balances the dissipation rate of turbulent kinetic energy. Given this energy budget, the mean flow energy dissipation could be identified by sensing the energy of the large amplitude turbulent fluctuations.

In this research, the energy-containing turbulence scale will be identified via wall-pressure fluctuation measurements. With each microphone sensing the local reduction in large-scale turbulent pressure fluctuation levels in response to flow control, an array of microphones positioned around the perimeter of the AIP could then indicate the spatial distribution of total pressure losses, which is an indirect measure of the circumferential distortion parameter *DPCP*. This concept will serve as the basis for the wall-imbedded microphone sensing technique to detect total pressure distortion.

3.2 Fundamentals of Wall Pressure Fluctuation Measurements

Fundamental fluid mechanics analysis suggested that the turbulent flow field is the source for wall-pressure fluctuations. Turbulence rarely is compressible, even in the case of supersonic mean flows [18]. Thus, Wark et al. [20] analyze the wall-pressure / flow structure relationship using Poisson's equation:

$$\nabla^2 p' = \frac{\partial u_x}{\partial y}\frac{\partial u_y}{\partial x} \tag{3.4}$$

which describes the turbulent pressure fluctuations for incompressible flows. Wark et al. [20] further simplified this expression by assuming the flow to be homogeneous in the spanwise (z-direction) direction and to confine the region of analysis to the boundary layer resulting in:

$$\nabla^2 p' = \frac{dU}{dy}\frac{\partial v'}{\partial x} + \frac{\partial u_x'}{\partial y}\frac{\partial u_y'}{\partial x} = q(x_s, y_s, z_s, t) \tag{3.5}$$

where $q(x_s, y_s, z_s, t)$ represents the spatial distribution of the turbulent fluctuation source strength at time t. This simplified expression (Eq. 3.5) can then be integrated over the boundary layer flow domain to yield an expression for the sensed wall-pressure fluctuations p'_w :

$$p'_w(x_0, y_0, z_0, t) = \iiint \frac{q(x_s, y_s, z_s, t)}{\sqrt{(x_0 - x_s)^2 + (y_0 - y_s)^2 + (z_0 - z_s)^2}} dV_S \tag{3.6}$$

The denominator of the volume integral in equation 3.6 is the distance between the turbulent pressure source and the wall sensor location. This aspect states that the amplitude of the radiated pressure wave from the inflow source decays according to the inverse of the distance between the measurement and the source, which resembles the behavior of a spherical pressure wave. Because of this spatial decay characteristic researchers have long believed that only those turbulent pressure fluctuation sources very close to the wall could be sensed. If this notion was valid the wall-pressure fluctuation sensor would be limited to describing only boundary layer flow dynamics, which account for a very small percentage of the entire airflow through the inlet. Disproving this theory, Moss and Oldfield [21] verified that wall sensors could detect freestream turbulent sources when the freestream integral length scales were comparable to the boundary layer length scales. Due to the abundance of freestream turbulence present in serpentine inlets the sphere of influence on each wall-pressure sensor will extend deep into the core flow field, giving the microphones a better capability of detecting all of the large, high amplitude turbulent structures responsible for total pressure losses.

3.3 Wall-Pressure Sensor Development

This section presents the results of a wall-pressure sensing study that intended to lay the foundation for the development of a reduced set of measurements that would correlate well with the *DPCP* parameter. The strategic placement of the 12-microphone array in the sector of the AIP that was affected by the flow control is explained. Then the next subsection presents the determination of the frequency band from the microphone signals that indicate the effectiveness of the flow control's ability in reducing and redistributing total pressure losses in the troubled flow sector. Finally, the RMS microphone array signals from the selected frequency band are shown to capture the improving trend of the flow quality with the application of flow control.

3.3.1 Sensor Placement

As in any automatic control system, the sensor placement needs to coincide with the regions of controllability by the actuation system. Total pressure distributions of the entire AIP were measured at several control efforts in order to determine the actual regions of controllability with the vortex generator flow affecters. Prior to the research conducted at the Virginia Tech / Techsburg Inlet Test Facility, this serpentine inlet was tested at the NASA Glenn Research Center producing AIP total pressure recovery distributions for an inlet throat Mach number of 0.65 flow at control efforts of 0%, 0.628%, 0.827%, 1.04%, and 1.2% control efforts. These total pressure recovery distributions at these control efforts are shown in Figure 3.1 a-e.

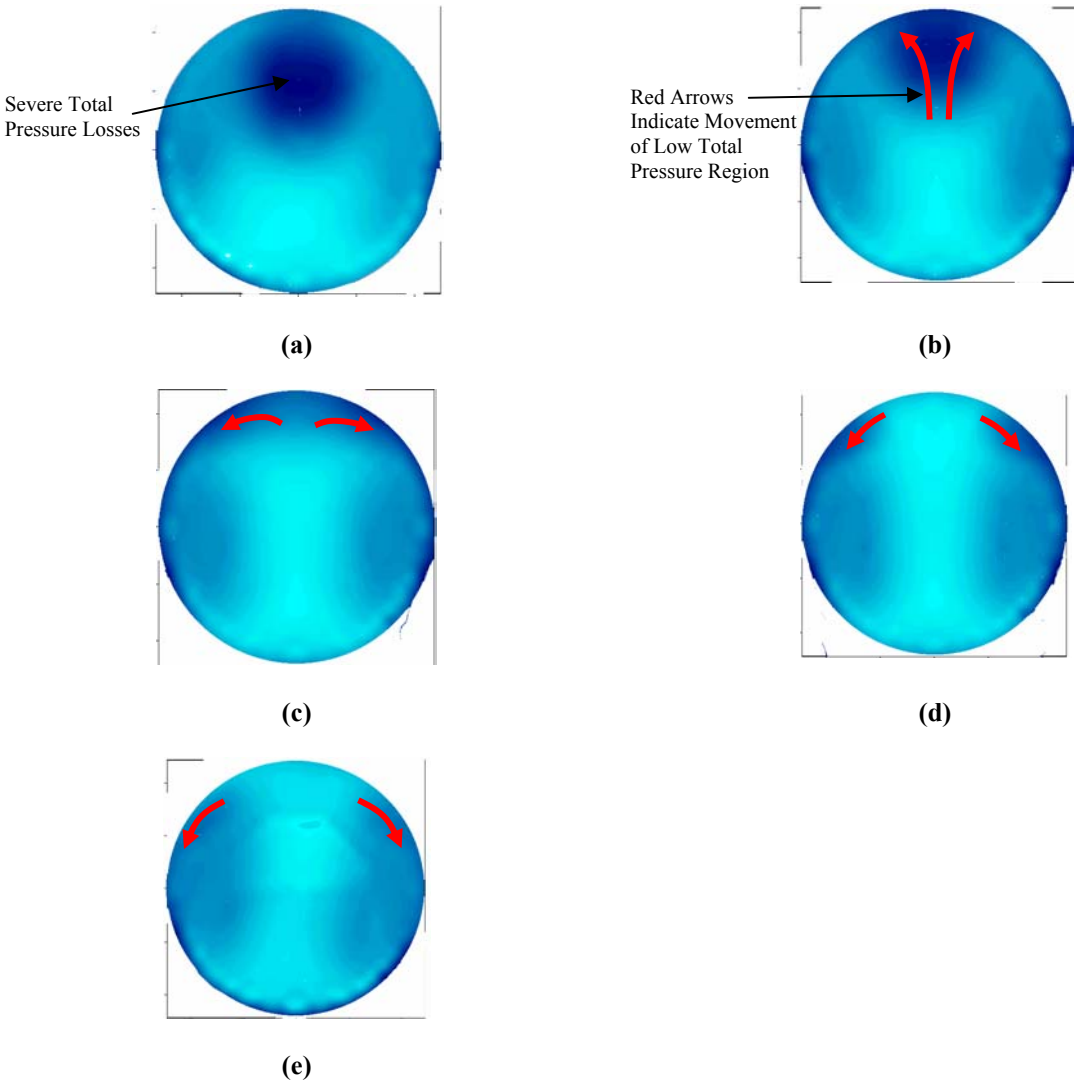

Figure 3.1: AIP Total Pressure Recovery Contours at Mach 0.65 for Control Efforts of: **(a)** 0%, **(b)** 0.628%, **(c)** 0.827%, **(d)** 1.04%, and **(e)** 1.2%

The flow control effectively removed the sector of low pressure recovery at the top-center region of the AIP with a control effort of 1.04% (Figure 3.1). The vortex generators thwarted the secondary flow development preventing the heavy accumulation of low-momentum flow to reach the top-center of the AIP, which was highlighted by the red arrows in Figure 3.1. After studying the relocation of the low-momentum flow in response to flow control (Figure 3.1), the flow region of controllability by the VG flow affecters was ascertained to be the sector between 0^{o} and 69^{o}, which is the grey region in Figure 3.2.

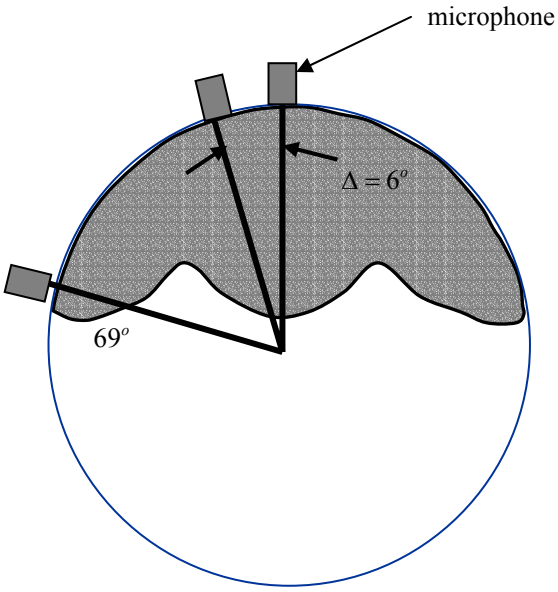

Figure 3.2: Region of Flow Controllability (in grey) and Microphone Array Placement at AIP

In accordance with this finding, a 12-microphone array was positioned at 6^o intervals subtending the angle between 3^o and 69^o to monitor the effectiveness of the flow control in this sector of the AIP.

3.3.2 Sensor Responses to Flow Control

Microphone array time histories were recorded for a Mach 0.55 flow with control efforts of 0%, 0.8%, 0.9%, 1.0%, and 1.2%. These time histories were transformed into the frequency domain where the auto spectra were analyzed to determine the frequency band that best indicated the severity of the total pressure losses in the controllable sector. The microphone array integrated RMS wall-pressures from the selected frequency band were then analyzed to determine if they captured the essence of the flow improvement due to flow control.

3.3.2.1 Sensor Spectral Analysis

It was described in Section 3.1.2 that the amplitudes of the large-scale, low frequency turbulence would dictate the degree of mean flow energy dissipation. In light of this fact, large amplitude RMS pressure fluctuations were expected to be sensed by the microphones in the vicinity of the severe low total pressure regions at lower frequencies. In order to capture this phenomenon, the RMS pressure spectra for the microphones located near the region of low total pressure recovery (microphone at 3°) and the region of high total pressure recovery (microphone at 69°) are shown in Figure 3.3 for the frequency range between 20 and 800 Hz.

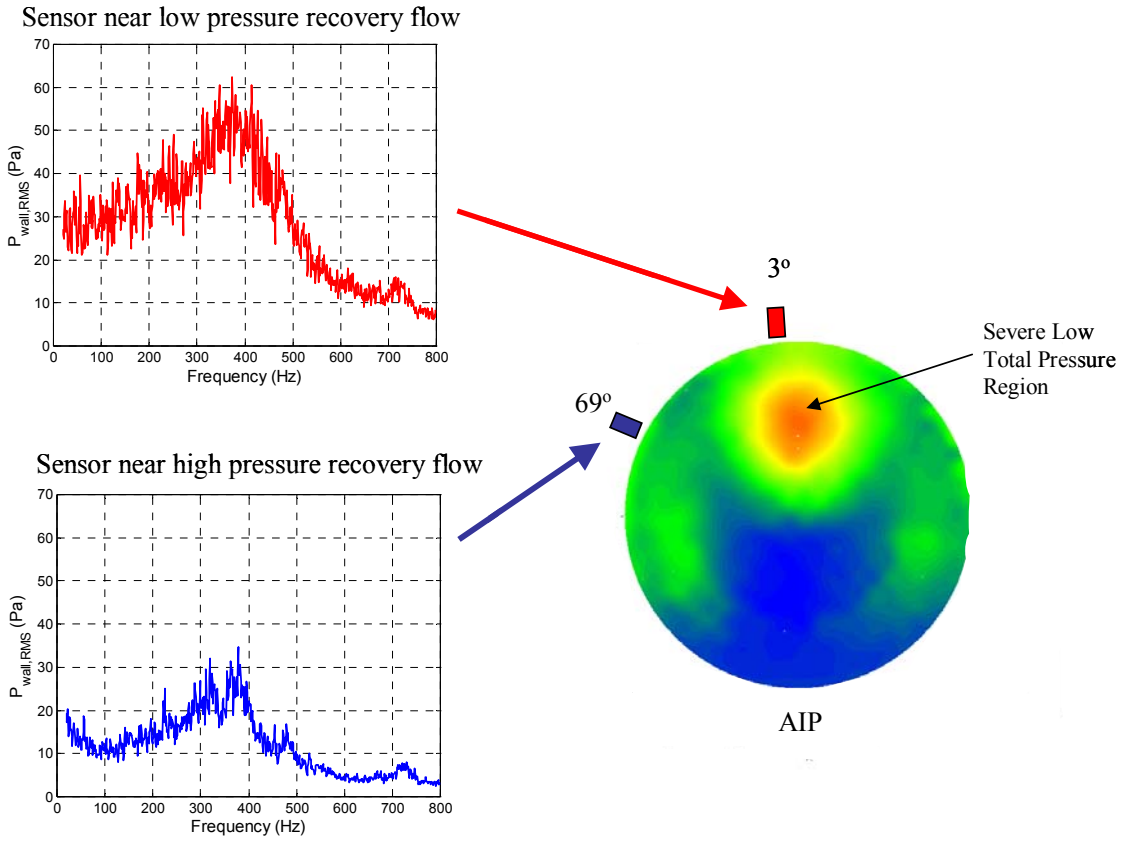

Figure 3.3: Comparison of RMS pressure spectra from microphones located near low and high total pressure recovery regions, No Flow Control at Mach 0.55

In accordance with the expectations, the RMS pressure fluctuations recorded near the region of low total pressure recovery were higher in amplitude compared to those measured near the region of high total pressure recovery (Figure 3.3). In fact, the measured RMS pressure fluctuations near the low total pressure flow were approximately 2.5 times greater in amplitude compared to those measured beneath high total pressure flow. For completeness, the RMS pressure spectra for the entire 12-microphone array over the same frequency range are shown as a contour plot in Figure 3.4.

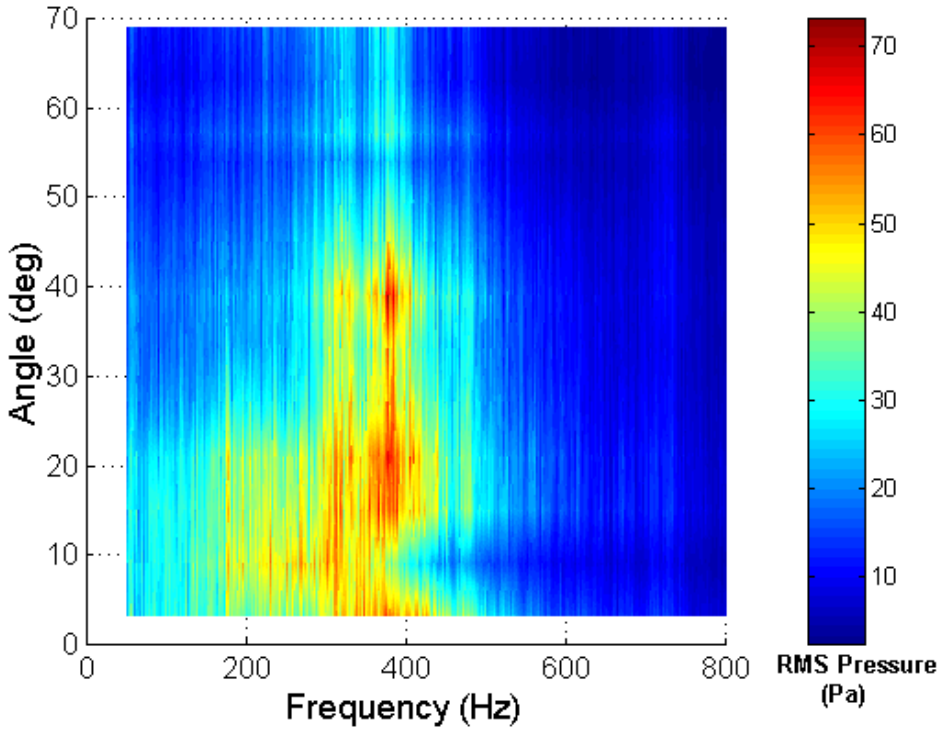

Figure 3.4: RMS Wall-Pressure Spectra for Baseline Flow at Mach 0.55

All microphones in the array recorded the largest pressure fluctuations below 400 Hz (Figure 3.4). For the microphones located at 3°, 9°, 15°, 21°, and 27° large amplitudes were recorded

well below 300 Hz (Figure 3.4) indicating an abundance of large-scale turbulence in this sector, which explained the severe total pressure losses in this upper sector of the AIP (Figure 3.1). Moving out to the sector between 27^o and 54^o these microphones recorded only large amplitude pressure fluctuations between 300 and 400 Hz, which suggests that the dominant turbulent length-scales are smaller than those between 3^o and 27^o. This result supports the fact that less total pressure is dissipated in this sector compared to the 3^o to 27^o sector. Finally, the sector beyond 54^o contained low amplitude pressure fluctuations across the entire bandwidth correctly indicating minimal total pressure losses in this sector.

Then it was desired to study the microphone spectrums under the influence of flow control. In order to determine if the microphones were capable of sensing that the flow control effectively removed the low total pressure region at the top-center portion of the AIP, the microphones at 0^o and 69^o were studied for their responses to flow control. The RMS pressure spectrums measured by the microphone near the original region of spoiled airflow at 3^o are shown in Figure 3.5 for control efforts of 0%, 0.8%, and 1.2%. The RMS pressure spectrums measured by the microphone near the region high total pressure at 69^o are then shown in Figure 3.6 for the same control efforts.

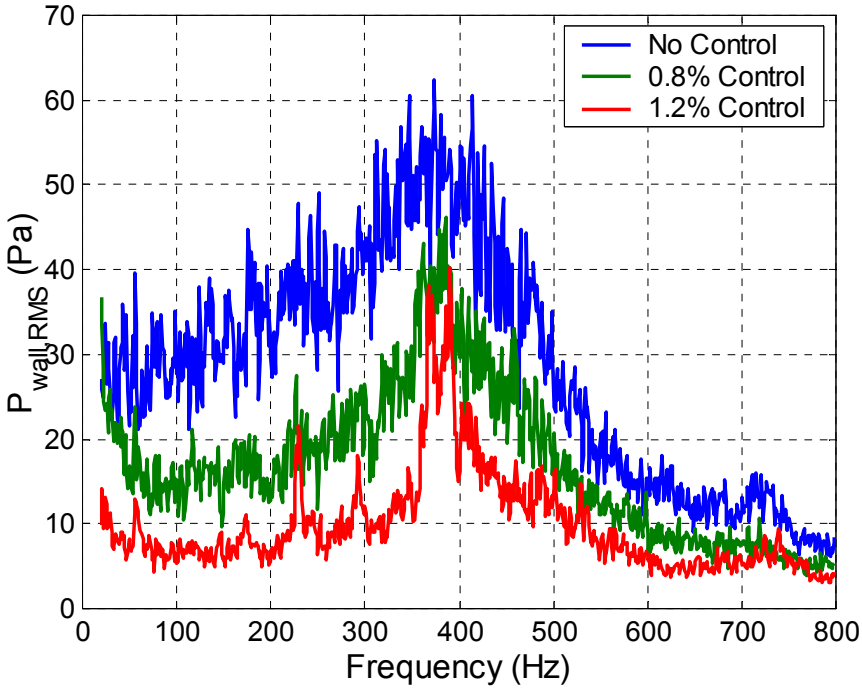

Figure 3.5: Spectral Results of Sensor (Located at 3°) Near Severely-Distorted Flow in Response to Flow Control

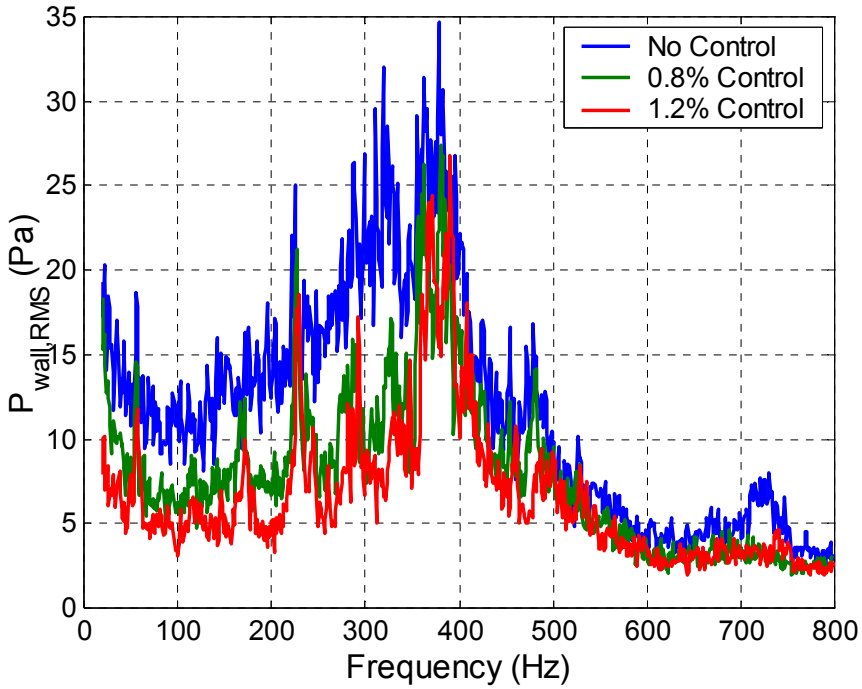

Figure 3.6: Spectral Results of Sensor (Located at 69°) Near Undistorted Flow in Response to Flow Control

The response to flow control from the microphone located near the distorted flow (Figure 3.5) showed considerable attenuation below 350 Hz. The microphone located near the high total pressure also recorded the greatest attenuations due to flow control at frequencies below 350 Hz (Figure 3.6), but the reductions in RMS pressure were considerably less than those recorded from the microphone at 3^o. Since the region near 3^o experienced greater improvements in total pressure recovery, these findings (Figures 3.5 & 3.6) suggested that the sensors were capable of distinguishing the levels in improvement of total pressure recovery. It should also be noted that as the flow control reduced turbulence levels, sharp tones at specific frequencies became noticeable. These tones were almost certainly not related to turbulence, since turbulence is more random in nature. These tones will be later defined as acoustic tones related to the facility in Section 3.5, and their effect on the turbulence measurements will be assessed. See Appendix B to examine the spectral results of the entire array in response to flow control. The stationarity of these wall-pressure signals is also presented in Appendix B. The stationarity analysis shown in Appendix B concluded that the typical coefficient of variation (the quotient of the standard deviation and the mean) for each spectral line between 50 and 800 Hz was between 12 and 18%. These low coefficients of variation suggest that the wall-pressure signals are at least weakly stationary, which should be more than adequate for control design purposes.

Then the trend in the attenuation of the RMS pressure spectra were analyzed for the entire array at increasing control efforts to identify the frequency band that best indicates the improvement in the total pressure distribution form the baseline case. The attenuation of the RMS pressure spectra from the baseline case are shown for the 0.8%, 0.9%, and the 1.2% control efforts in Figures 3.7, 3.8, and 3.9, respectively.

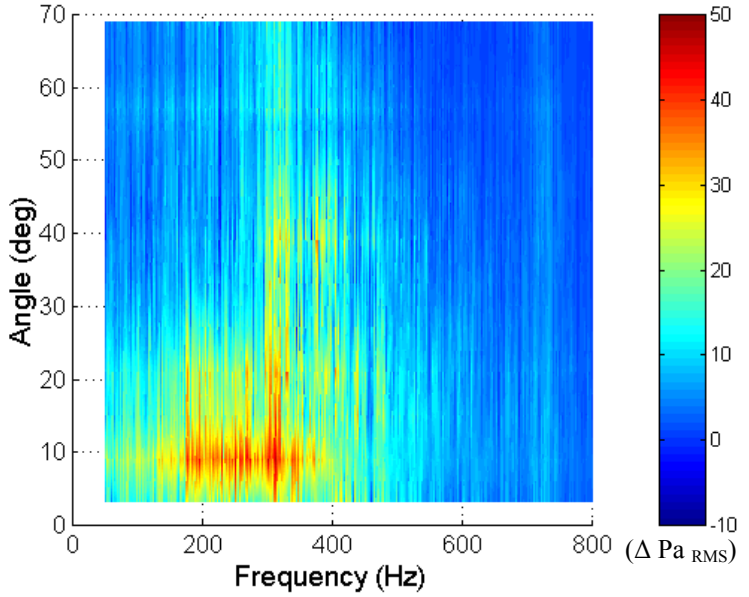

Figure 3.7: RMS Pressure Reductions from Baseline to 0.8% Control, Mach 0.55

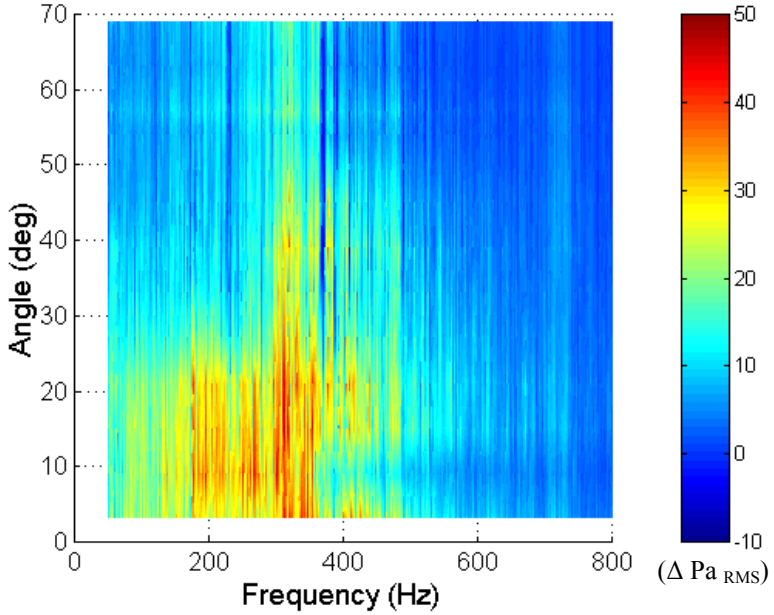

Figure 3.8: RMS Pressure Reductions from Baseline to 0.9% Control, Mach 0.55

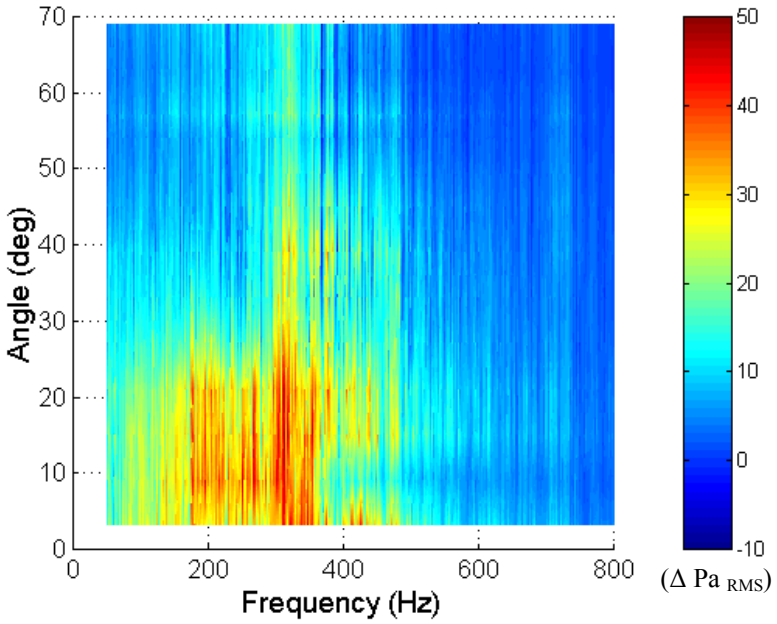

Figure 3.9: RMS Pressure Reductions from Baseline to 1.2% Control, Mach 0.55

Under the influence of a 0.8% control effort, the microphone array recorded attenuations between 30 and 50 Pascals for the 3^o and 9^o sensors (Figure 3.7), which equated to a 50% reduction in turbulence levels from the baseline case. The significant reductions shown from these sensors correctly detected that the pressure recovery in this region had been drastically improved by the 0.8% flow control effort. Again the reductions for these two sensors primarily occurred at frequencies below 400 Hz. The sensors from the remainder of the array sensed more modest reductions in RMS pressures, which captured the fact that the 0.8% control effort allowed the secondary flow to carry turbulent, low momentum flow though this sector. Injection of a 0.9% control effort achieved considerable reductions in RMS pressure amplitudes for the entire array (Figure 3.8). Again, the greatest attenuation occurred at frequencies below 350 Hz. The wall sensors indicated that 0.9% control reduced the strength of the inlet secondary flow,

allowing the accumulated turbulent, low-momentum flow to reach a position of approximately 30°. Finally at a 1.20% control effort, the microphone array sensed only slight improvements in the flow quality when compared to the 0.9% flow control scenario (Figure 3.9). From these observations, it was decided that the frequency range between 50 and 350 Hz would best indicate the total pressure recoveries in the vicinities of the microphones.

3.3.2.2 Array RMS Pressure Responses to Flow Control

The array distributions of total RMS wall-pressures between 50 and 350 Hz were then compared to the pressure recovery contours at each flow control condition. The total RMS wall-pressures from the 12-microphone array between 50 and 350 Hz are shown in Figure 3.10.

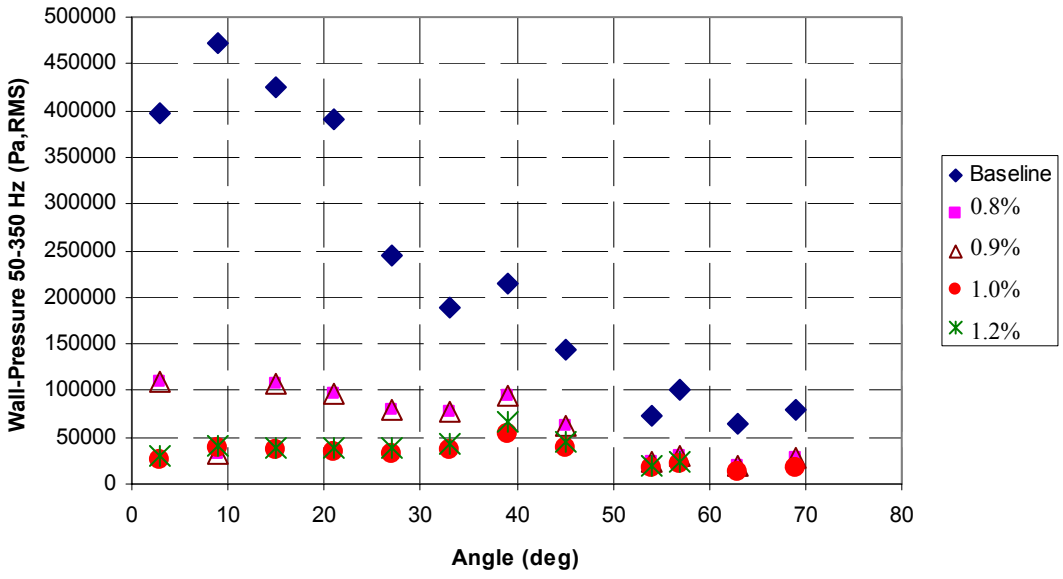

Figure 3.10: Microphone Array Responses to Flow Control, Mach 0.55

The RMS pressure distributions from the microphone array (Figure 3.10) show that the flow control instates uniformity in the total pressure over this flow sector. The microphones sense the considerable reductions in total pressure loss at the top-center portion of the AIP, and the modest improvements in the locations approaching 69^{o}. The average and the coefficient of variation of the 12-microphone array are shown in Table 3.1 for each control scenario.

Table 3.1: Statistical Results of Microphone Array for each Flow Control Effort at Mach 0.55

Control effort (%)	Array Pressure Coefficient of Variation	Array Pressure Average (Pa)
0	0.6492	232637
0.8	0.5461	63368
0.9	0.4289	37422
1	0.4180	34628
1.2	0.3797	30372

The reduction in the microphone array coefficient of variation indicates increasing uniformity in the total pressure distribution, and the reduction of the array average indicates an overall increase in total pressure recovery (Table 3.1). Unfortunately neither of these statistical metrics correlated well with the corresponding *DPCP* and *PR* values. As this was the case, a signal involving a combination of a small subset of sensor from the entire array was still needed to estimate *DPCP* values at each control effort.

3.4 Microphone-Based Observer of *DPCP*

3.4.1 Observer Concept

In the spirit of finding an adequate reduced set of measurements capable of estimating *DPCP*, an observed trend in the measurements was exploited and compared to the corresponding *DPCP* parameters. As the flow control effort increased, it was noticed that the RMS pressure levels from the microphones near 0^o approached the RMS pressure levels from the microphones near 69^o. This trend captures the effectiveness of the flow control in removing the large region of spoiled airflow near 0^o and providing a flow in this region with similar quality compared to the flow near 69^o. The difference between the pressure levels from the location near 0^o and those in the proximity of 69^o was chosen to quantify the convergence of the flow quality in the regions. In particular the addition of mean-square pressure amplitudes for the 63^o and 69^o locations were subtracted from the sum of the mean-square pressure amplitudes for the 3^o and 9^o locations and represented by $\tilde{H}$ in the following manner:

$$\tilde{H} = \left[\left(p'_{3^o,RMS} \right)^2 + \left(p'_{9^o,RMS} \right)^2 \right] - \left[\left(p'_{63^o,RMS} \right)^2 + \left(p'_{69^o,RMS} \right)^2 \right] \tag{3.7}$$

A slight modification was made to the calculation of $\tilde{H}$ from that shown in Equation 3.7 to simplify the range of values for $\tilde{H}$. Instead of trying to use the large valued RMS pressure readings in engineering units of Pascals, a smaller range in the pressure readings was achieved by using scaled-down microphone sensitivities. The sensitivities of the microphones used for

these experiments were on the order of 4e-5 Volts/Pa, and the voltage signals from the microphones was on the order of a few Volts. In order to work with feedback values on the same order as the microphone voltage signals, the microphone were scaled with the actual sensitivity of each microphone normalized by the average microphone sensitivity of the entire array. The actual feedback signal to be used in the automatic control system was denoted as H and is represented in terms of the microphone voltages V and the normalized sensitivities $|s|$ as

$$H = \left[|s_{3^o}|^2 V_{3^o}^2 + |s_{9^o}|^2 V_{9^o}^2 \right] - \left[|s_{63^o}|^2 V_{63^o}^2 + |s_{69^o}|^2 V_{69^o}^2 \right] \tag{3.8}$$

The feedback signal H for Mach numbers 0.4, 0.5, and 0.55 was calculated for various control efforts and plotted in Figure 3.11.

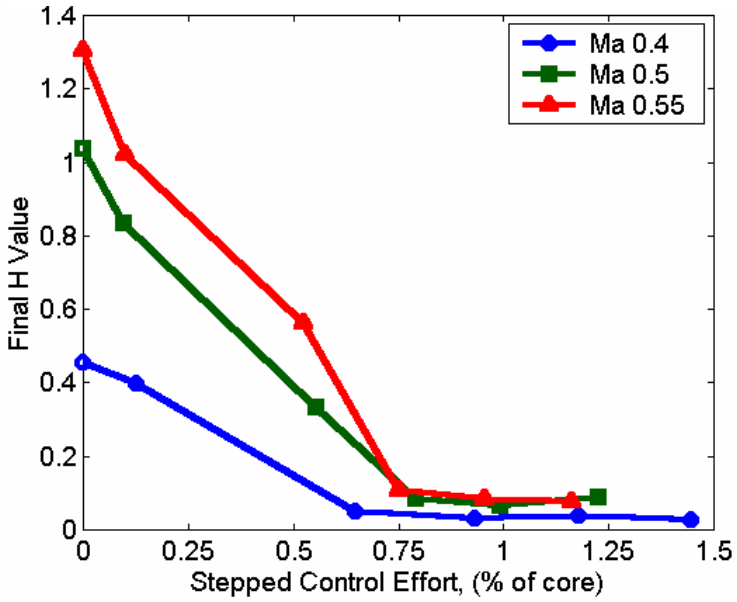

Figure 3.11: Feedback Signal H Steady-State Responses to Flow Control

Since no detailed aerodynamic data was logged for control efforts between 0% and 0.8%, microphone responses to step input control efforts were recorded to provide system responses in

this band of missing data. The results shown in Figure 3.11 were obtained from the steady-state response of *H* to the stepped control inputs. Validation of *H* as a suitable feedback observer of *DPCP* served as the next process in the development of the feedback component of the control system.

3.4.2 Feedback Signal Validation

Correlation analysis was conducted to validate *H* as a suitable feedback observer of *DPCP*. The steady-state responses of *H* shown in Figure 3.11 revealed a dependency on Mach number. As a consequence the relationship between *H* and *DPCP* was performed separately for each Mach number. For each of the three Mach conditions, the control efforts applied to the system from Figure 3.11 did match the control efforts used to obtain the *DPCP* from the fine grid of total pressure measurements; therefore, curve-fitting provided the interpolated *DPCP* values that corresponded to the stepped control efforts from Figure 3.11. The *H* and *DPCP* parameters for the Mach 0.55 flow speed are plotted versus a variety of control efforts in Figure 3.12. Both *H* and *DPCP* parameters demonstrated extremely similar trends with respect to control effort (Figure 3.12). The correlation between *H* and *DPCP* was determined by assessing the quality of linear fit between these two parameters. The quality of linear fit was determined by calculating the Pearson product moment correlation coefficient, more familiarly known as the R^2-value [22]. The least-squares linear curve-fits between *H* and *DPCP* are shown in Figures 3.13, 3.14, and 3.15 for the Mach numbers 0.55, 0.5, and 0.4, respectively. The statistical analysis concluded that *H* and *DPCP* were 97% correlated (Figure 3.13) for a Mach 0.55 flow, which indicated that *H* would serve as an excellent observer of *DPCP*. The correlation between *H* and *DPCP* for

Mach 0.5 is 99% (Figure 3.14) and 98% for Mach 0.4 (Figure 3.15). With the knowledge of Mach number, the observation of H would directly indicate the distortion level for the symmetric, level flight condition simulated in these experiments. The error bars in Figures 3.13, 3.14, and 3.15 are the standard deviations of the steady-state responses of H to the appropriate step control inputs. At both the high and low extremes of the signal H, the standard deviations overlap (Figures 3.13, 3.14, and 3.15). This overlap in the standard deviations indicates that H is not guaranteed to distinguish between the two flow scenarios in question, which may be problematic for the future control system. Finally, it should be noted that these curve-fits in Figures 3.13, 3.14, and 3.15 were conducted with a minimal ensemble of data due the high cost in obtaining the necessary total pressure measurements to determine the *DPCP* values. It would be advantageous for future experiments to obtain more *DPCP* values at different control efforts in order to provide a curve-fit with a higher confidence level. The design and demonstration of a closed-loop automatic distortion control system with the microphone-based *DPCP* observer H will be presented in Chapter 4.

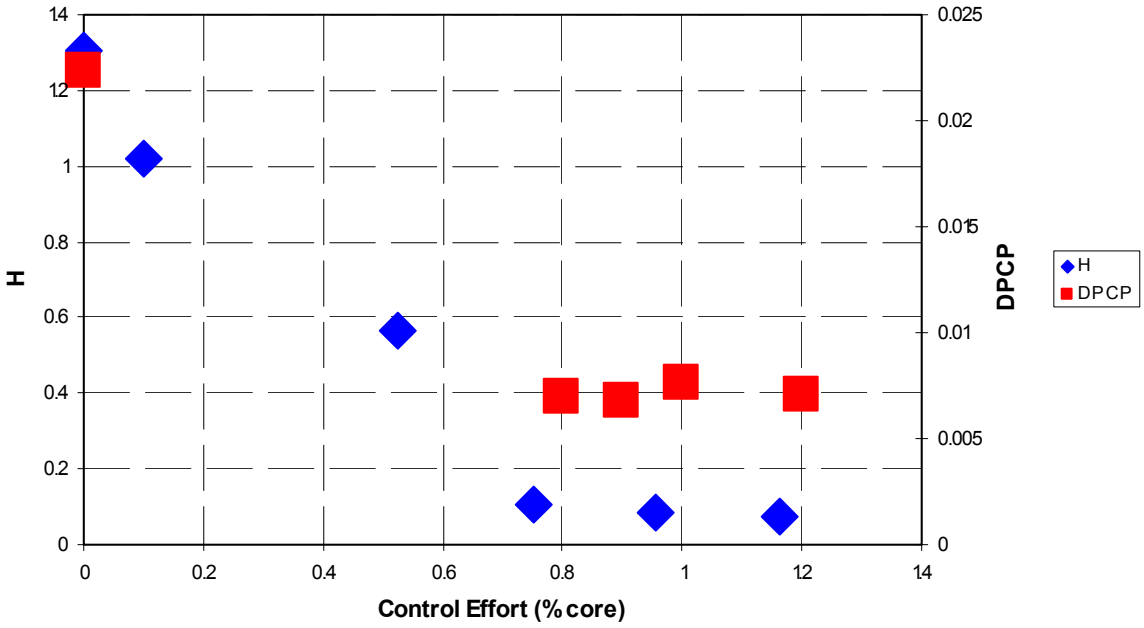

Figure 3.12: *H* and *DPCP* as a Function of Control Effort at Mach 0.55

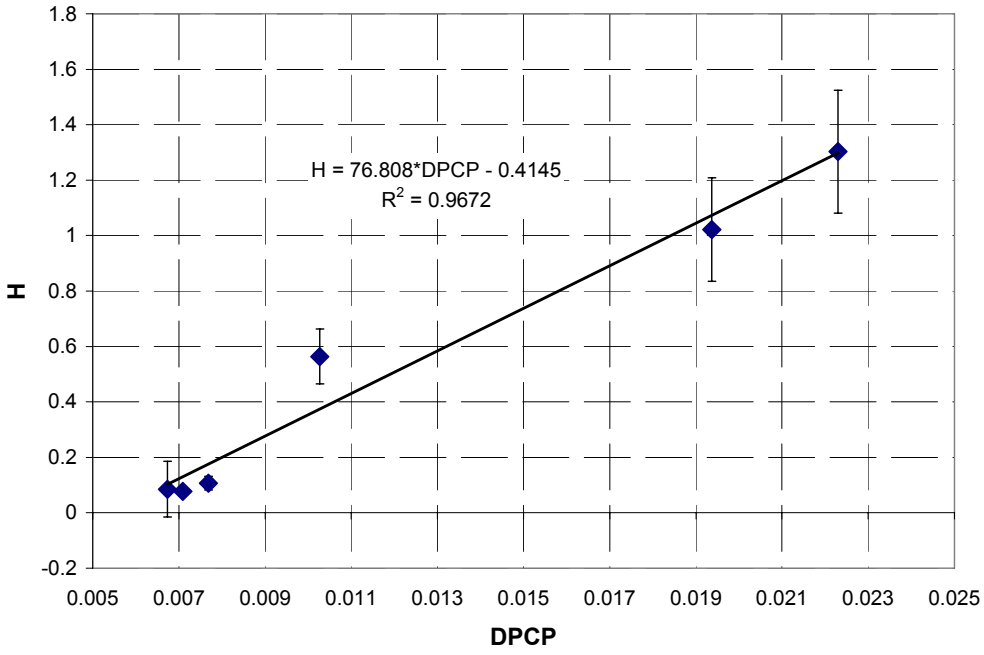

Figure 3.13: Correlation of *H* and *DPCP* at Mach 0.55

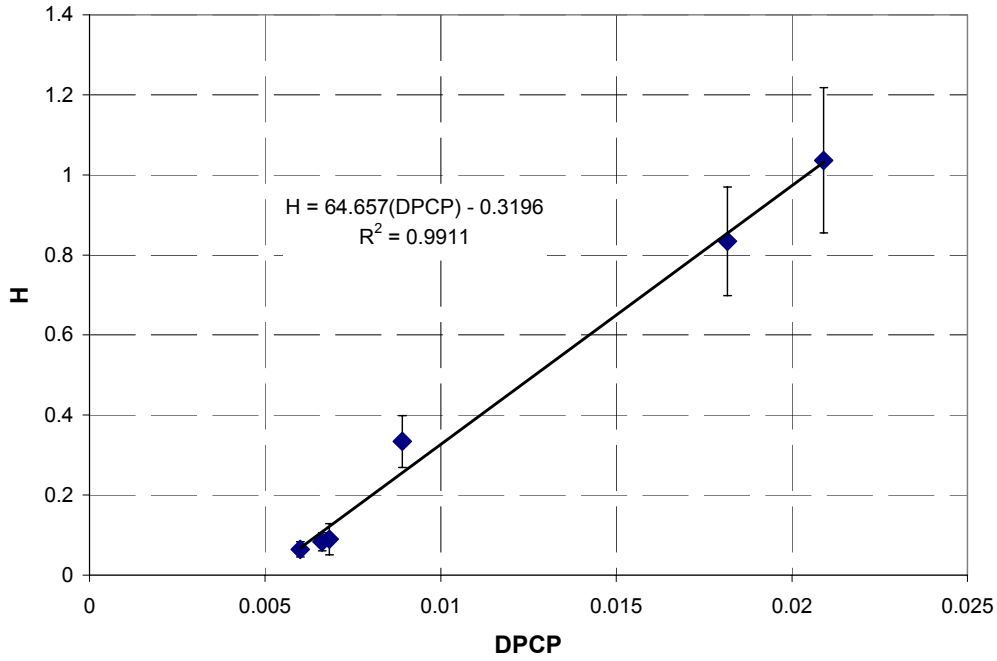

Figure 3.14: Correlation of *H* and *DPCP* at Mach 0.5

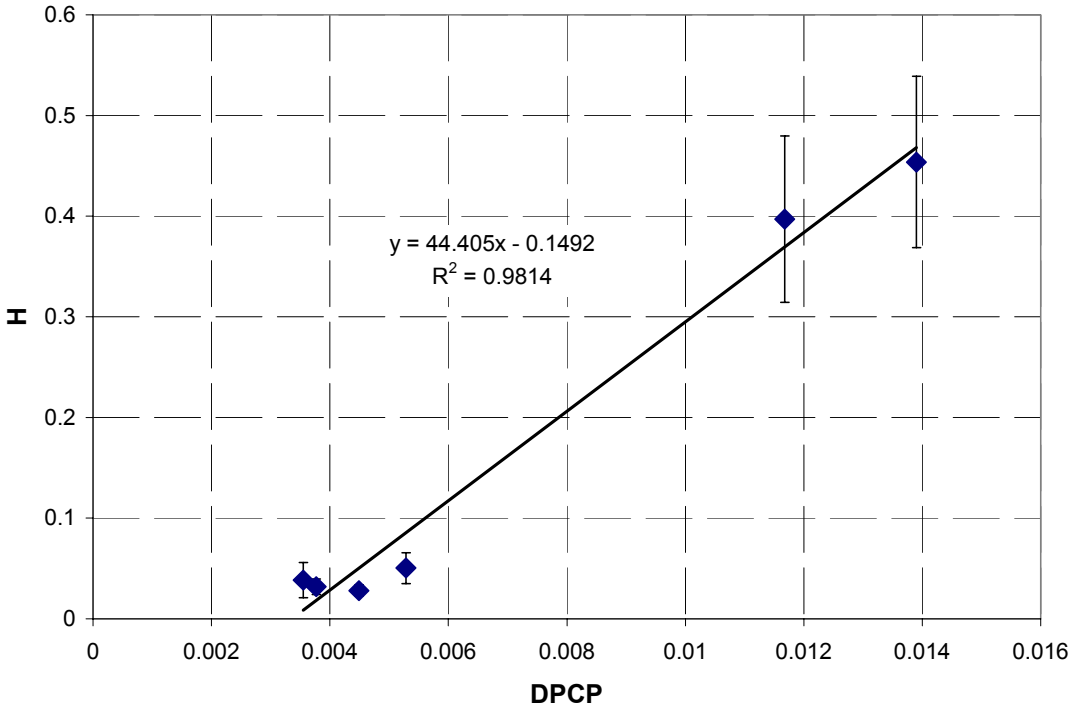

Figure 3.15: Correlation of *H* and *DPCP* at Mach 0.4

3.5 Extraction of Turbulent Pressure Fluctuations from Wall-Pressure Fluctuation Measurements

The microphone wall-pressure signals are composed of turbulent pressure fluctuations described by Poisson's equation (Eq. 3.6) and facility-related acoustic background noise. These background acoustic disturbances bias the assessment of the turbulent pressure fluctuations from the wall-pressure fluctuation measurements. The effect these disturbances have on the turbulence measurements needed to be evaluated in order to determine if the distortion observer technique needed to be updated with a technique to filter-out the disturbances. Obviously, an additional filtering process is undesired from a control systems perspective as it would place increased computational demands on the controller. This section presents a technique [23, 24] that removes facility-related acoustic noise from wall-pressure measurements.

3.5.1 Background Noise Removal Concept

Early attempts to remove background disturbance signal content involved array averaging techniques that provided only a statistical estimate of the background noise. Another drawback of the array averaging technique was the demand for a large number of sensors. Later refinements on resolving turbulent fluctuation components from acoustic components were introduced [25, 26] that required only two sensors. This technique involved the difference of two span-wise microphone signals that were spaced apart by a distance greater than half of the

boundary layer thickness. This span-wise spacing was speculated to be larger than the length-scales of any turbulent vortex in a boundary layer, which has since been proven to be an insufficient spacing with regards to achieving uncorrelated turbulent content at each sensor. A major shortcoming of this difference technique was that it also only provided statistical estimates for the turbulent fluctuation pressures.

The facility noise removal concept used in this research relies on an understanding of the turbulence length-scales in the airflows to be measured. This noise removal concept utilizes a span-wise microphone configuration shown in Figure 3.16. A span-wise sensor spacing (Figure 3.16) is used to capture pressure fluctuations from uncorrelated sources. The spacing in the span-wise direction must be large enough to ensure that both sensors will not sense the radiated pressure from any one turbulent pressure source. As a minimum requirement the spacing must be larger than the largest turbulent length-scale ($\Delta s > \ell$). In satisfying this spacing requirement, the wall-pressure measurement content for these two sensors attributed to turbulent pressure fluctuations will be uncorrelated; however, any background noise affecting both sensors will be highly correlated. Naguib et al. [23] proposed an optimal filtering technique to extract the actual background signal time histories. If the background noise is proven to severely hinder the accuracy of the distortion observer *H*, the optimal filtering technique would be necessary for real-time implementation into the control system. The initial off-line analysis of the effects of background noise on the signal *H* were conducted with coherence functions. The coherence function provided the coherent content, or acoustic content in this case, to be removed from the wall-pressure measurement. The optimal filter would merely attempt to emulate the coherence function with an optimized finite impulse response (FIR) filter.

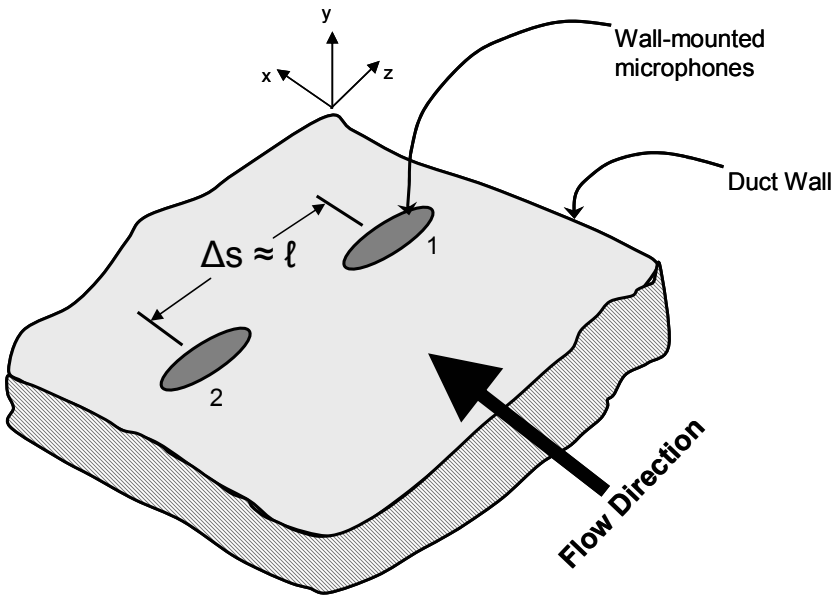

Figure 3.16: Span-wise Microphone Spacing for Detecting Background Facility Noise

3.5.2 Expected Acoustic Disturbances

Before the wall-pressure signals were analyzed for their acoustic content, the facility was examined for its possible acoustic sources. This facility acoustic analysis would help to explain the results obtained from the background acoustic noise filtering process. This inlet test facility contained several waveguides that could be excited at their respective resonant frequencies by the broadband jet noise from the inlet exit plane and the jet engine. The air jet exhausted from the inlet into the downstream plenum carries with it a tremendous amount of turbulence from the distorted airflow in the inlet. According to Lighthill [27, 28] the turbulent vortices that shed

through the shear layer into the stagnant air of the plenum radiate high levels of acoustic energy. Lighthill also determined that the acoustic radiation associated with this phenomenon was primarily directed in the jet stream direction generally remaining within 18^o of the jet. The directional nature of this radiation prevented this radiation from affecting the upstream microphones in the inlet; however, the standing waves that were excited within the plenum were expected to affect the microphone measurements.

Since the downstream plenum had a cross-sectional area that was 23 times larger than the inlet cross-section, the plenum adequately stagnated the air stream. Since the airflow is assumed stagnant, the simple acoustic wave equation for a non-moving media provided the estimate of the plenum natural frequencies. The cylindrical plenum was 10-feet long with a 4-foot diameter constructed of 1/2"-thick steel walls. The closed-closed end boundary conditions of this plenum forced zero-acoustic-pressure-gradients at both ends of the plenum. After application of these boundary conditions, the resulting eigenvalues correspond to half-wave axial resonances as:

$$f_n^{aft} = \frac{nc}{2L} \quad ; \quad where \;\; n = 1, 2, 3, ..., \infty \tag{3.9}$$

where c represents the speed of sound and L represents the length of the plenum. Finally, Table 3.2 summarizes the downstream plenum acoustic axial resonant frequencies in the frequency range of interest (50-350 Hz) according to Equation 3.9.

Table 3.2: Acoustic Plane Wave Natural Frequencies (50-350 Hz) in the Downstream Plenum

n	f_n *(Hz)*
1	55.8
2	111.5
3	167.3
4	223.1
5	278.9
6	334.6

In addition to the plane wave modes described in Table 3.2, out-of-plane acoustic modes will also exist in the downstream plenum at these low frequencies between 50 and 350 Hz. These higher-ordered acoustics cut-on at a low frequency of 82 Hz because of the large cross-sectional area of the plenum. The resonant frequencies of the higher-ordered acoustic modes that could potentially be excited in the downstream plenum are presented in Table 3.3.

Table 3.3: Resonant Frequencies (50-350 Hz) of Higher-Ordered Acoustic Modes in the Downstream Plenum

Mode (circumferential, radial)	*f(Hz)*
(1,0)	81.7
(2,0)	135.5
(0,1)	170
(1,1)	236.5
(2,1)	297
(0,2)	311

Since the turbulent jet exhausts into the center of the downstream plenum, it was anticipated that (0,1) and the (1,1) acoustic modes would be excited to higher energy levels.

The inlet itself can also be excited at its acoustic natural frequencies by the broadband turbulent sources. Since the air in the inlet is not stagnant, the homogeneous wave equation for sound pressure in a moving media was necessary to determine the inlet resonant frequencies. The homogeneous wave equation for sound pressure in a moving media is given as [29]:

$$\nabla^2 p - \frac{1}{c^2}\left(\frac{\partial}{\partial t} + \vec{V}\cdot\nabla\right)^2 p = 0 \tag{3.10}$$

where $\vec{V}$ represents the velocity of the media. In applying this governing equation (Eq. 3.10), the inlet was assumed to be a straight, hollow cylinder as shown in Figure 3.17. The wall of the cylinder was assumed rigid, and both ends were modeled as open.

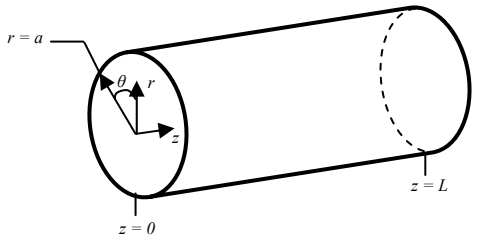

Figure 3.17: Serpentine Inlet Acoustic Model

The relationship for the axial resonant frequencies in the serpentine inlet is given as:

$$f_n = \left(1 - M^2\right)\frac{nc}{2L} \tag{3.11}$$

This relationship (Eq. 3.11) revealed a dependence of the axial resonant frequencies on the Mach number. This wave equation, however, was derived with several assumptions: homogeneous medium, constant flow speed, and no internal energy losses. It is expected that the constant flow speed assumption along the length of the duct will present discrepancies, because diffusers are designed to convert dynamic pressure into static pressure (ie., the airflow decelerates along the length of the duct). With a constant Mach number assumption the expected plane wave resonances will occur every 97 Hz. Finally, it should be noted that the cut-on frequency for the higher-ordered acoustic modes in the serpentine inlet is 785 Hz, which is well above the frequency range of interest for this sensing scheme (50-350 Hz). Thus, higher-ordered acoustic modes within the inlet would not affect the sensing scheme. These inlet resonances and the aforementioned plenum resonances were expected to be the dominant sources of acoustic disturbance to the turbulence sensors at the exit-plane of the inlet.

3.5.3 Application of Filtering Technique

This filtering technique was intended to remove the background acoustic noise affecting the four microphone signals used in the distortion observer *H*. Each of these four microphone signals was to be compared with an auxiliary microphone signal that measured turbulent pressure fluctuations from different turbulent sources. A sufficient span-wise spacing was necessary to ensure that the turbulent content of the signals being compared was in-fact uncorrelated. In light of this, it was decided to use the largest span-wise spacing allowed by the original 12-microphone array, which equated to a spacing of 60^{o}. Table 3.4 indicates the locations of the

primary signals from *H* and the auxiliary sensors used for filtering-out the acoustic disturbances from the primary signals according to a 60^o-spacing. Notice that use of this span-wise spacing conveniently required only the four signals from *H* to be measured.

Table 3.4: Microphones Used in Filtering Technique to Remove Acoustic Disturbances *H*

Location of Primary Signal (deg)	Location of Auxiliary Signal for Comparison (deg)
3^o	63^o
9^o	69^o
63^o	3^o
69^o	9^o

The ordinary coherence functions given as:

$$\gamma^2 = \frac{G_{XY}G_{YX}}{G_{XX}G_{YY}} \tag{3.12}$$

which derived from the Chebychev inequality, were examined between the microphones to be compared according to Table 3.4. With these microphone pairings, the correlated content between any microphone-pairing was explained by either $\gamma^2_{3^o,63^o}$ or $\gamma^2_{9^o,69^o}$. Since plane-wave acoustic disturbances were expected in this low frequency band between 50 and 350 Hz, both coherence functions $\gamma^2_{3^o,63^o}$ and $\gamma^2_{9^o,69^o}$ were expected to yield similar values. The coherence functions $\gamma^2_{3^o,63^o}$ and $\gamma^2_{9^o,69^o}$ in the 50 to 350 Hz frequency band are plotted for the control effort of 1.20% in Figure 3.18. It should be noted that 60 spectrums were averaged in obtaining all of the coherence spectra in this chapter. The coherence functions were first examined for the

scenario of maximum control effort (1.20%), which yields the poorest turbulence-to-acoustic-disturbance ratio (Figure 3.18). Both coherence functions were remarkably similar, as the high coherence spectral lines were in excellent agreement. Many of these spectral lines of high coherence are speculated to result from acoustic standing waves located in the plenum downstream of the serpentine inlet, and the coherence spectral lines associated with these acoustic modes are labeled in Figure 3.18. The plane-wave acoustic modes from the downstream plenum are labeled at their respective natural frequencies ($f_1 \rightarrow f_6$) in Figure 3.18. Similarly, the energetic (0,1) and (1,1) modes are labeled at their respective natural frequencies in Figure 3.18. Another component that showed high coherence was electrical noise, which was noticed at 60 Hz intervals. It should be noted that the expected acoustic disturbance associated with standing waves inside the inlet were not identified in the measured data. The coherence functions $\gamma^2_{3^o,63^o}$ and $\gamma^2_{9^o,69^o}$ are also plotted for control efforts of 0.9%, 0.8%, and no flow control in Figures 3.19, 3.20, and 3.21, and these coherence functions are all similar to each other as well. They all also detect relatively high levels of correlated content at each the spectral lines associated with the standing waves in the downstream plenum. The only exception to this trend occurred for $\gamma^2_{9^o,69^o}$ in the no flow control case between 135 and 260 Hz (Figure 3.21), where the speculated acoustic sources were not as salient.

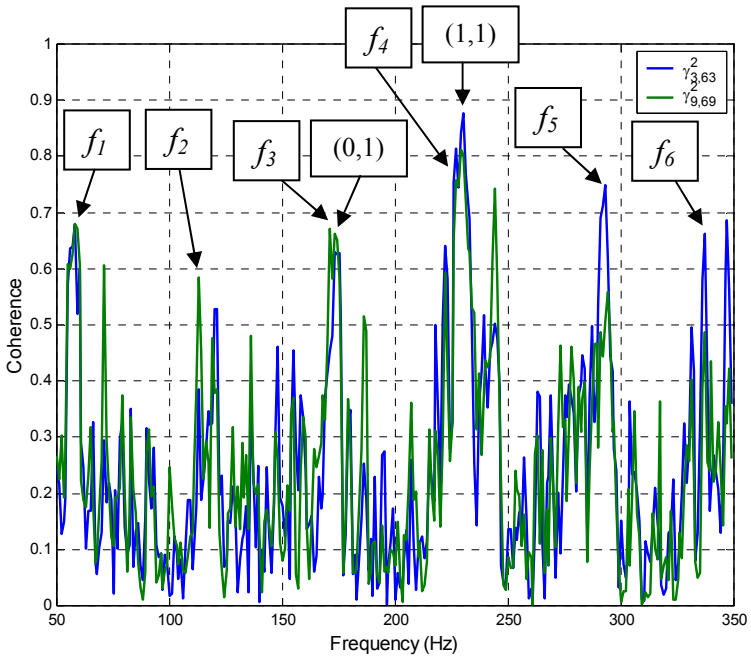

Figure 3.18: $\gamma^2_{3^o,63^o}$ and $\gamma^2_{9^o,69^o}$ with 1.20% Flow Control at Mach 0.55

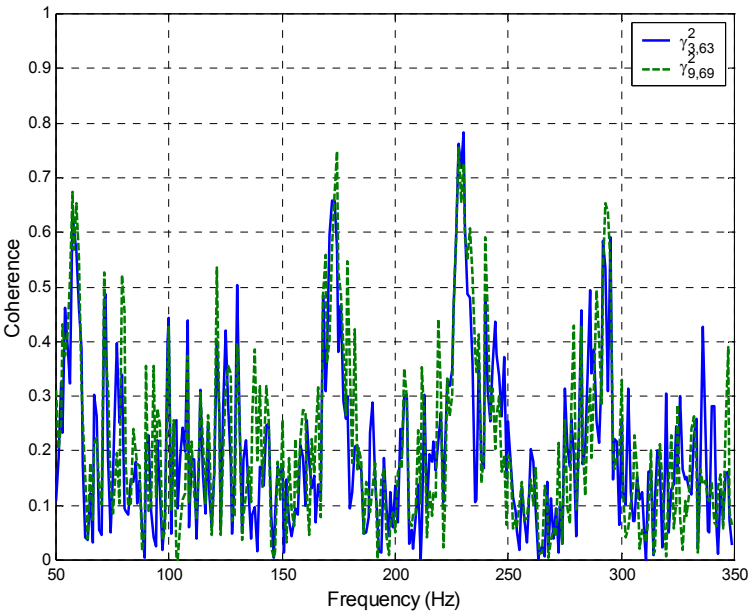

Figure 3.19: $\gamma^2_{3^o,63^o}$ and $\gamma^2_{9^o,69^o}$ with 0.9% Flow Control at Mach 0.55

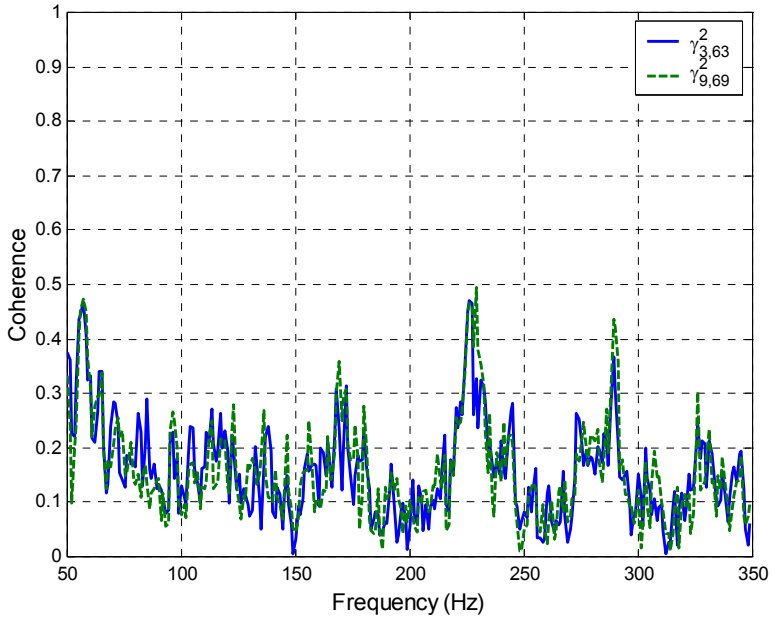

Figure 3.20: $\gamma^2_{3^o,63^o}$ and $\gamma^2_{9^o,69^o}$ with 0.8% Flow Control at Mach 0.55

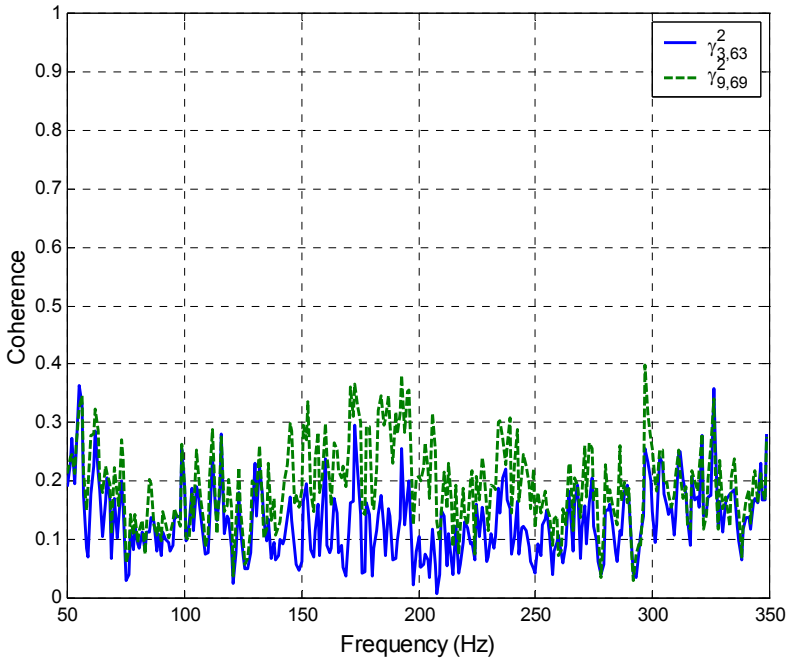

Figure 3.21: $\gamma^2_{3^o,63^o}$ and $\gamma^2_{9^o,69^o}$ with No Flow Control at Mach 0.55

A probable cause for the relatively higher coherence levels in this region is acoustic wave scattering in the thick TBL, which is a nonlinear effect where the incoming wave is scattered over frequencies other than the incident frequency [29]. It should be noted that the axial, acoustic resonance within the serpentine inlet was never clearly identified as a major disturbance in the preceding coherence analysis. The average coherence levels for each flow control scenario are shown in Table 3.4, and they ranged between 0.13 and 0.24. As the increased flow control attenuated the turbulence levels, the coherence levels also increased as the turbulence-to-acoustic-disturbance ratios degraded.

On a final note, the coherence levels between the microphone at 3^o and the other 11 microphones in the original array are shown in Figure 3.22. Consistently high coherence levels at the frequencies associated with the standing waves in the downstream plenum were noticed for the entire array (Figure 3.22), which helps to substantiate that the microphones are detecting these plane-wave disturbances from the downstream plenum. The final evidence that the primary acoustic disturbances are planar lies in the fact that the phase of the cross-spectrums between the microphone at 3^o and the other microphones in the array are zero at the same spectral lines of consistently high coherence for the entire array. Figure 3.23 shows the phase between the microphone at 3^o and the microphones at 39^o, 45^o, 54^o, and 57^o with the zero-phase regions associated with the six acoustic standing waves highlighted by their respective natural frequencies ($f_1 \rightarrow f_6$).

Table 3.5: Average Coherence Between 50 and 350 Hz

Control Effort (%)	**Average** $\gamma^2_{3^o,63^o}$	**Average** $\gamma^2_{9^o,69^o}$
None	0.131	0.193
0.8%	0.158	0.158
0.9%	0.202	0.241
1.2%	0.243	0.242

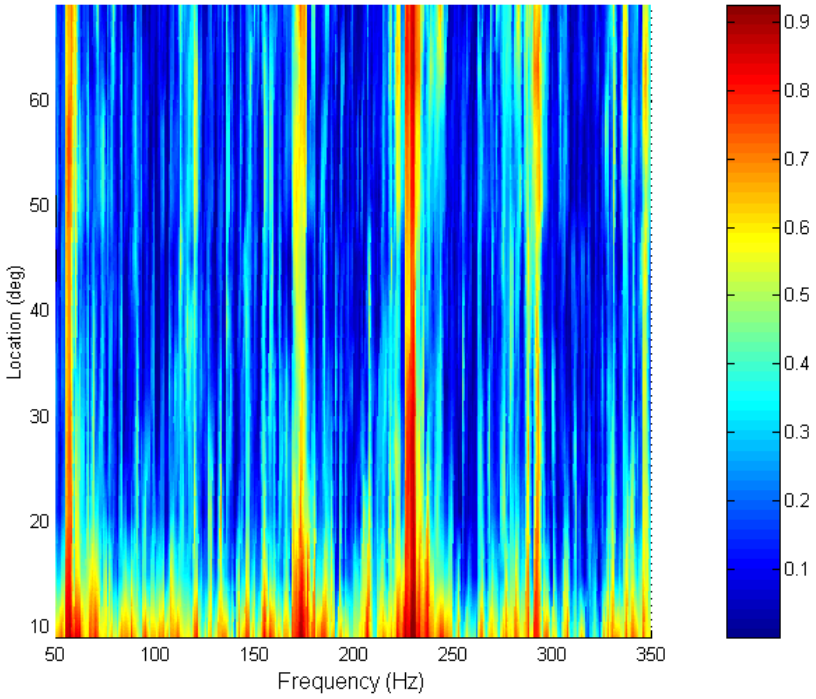

Figure 3.22: Coherence Between Microphone at 3° and other 11 Microphones from the Array at 1.20% Flow Control at Mach 0.55

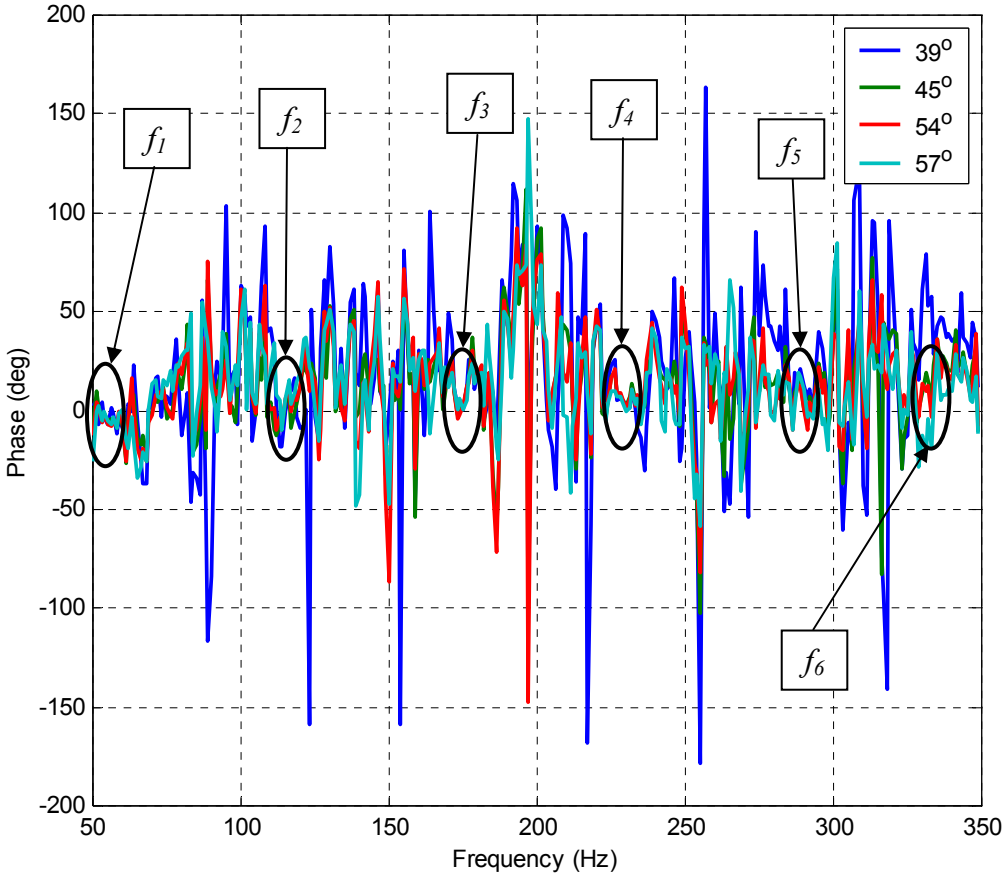

(a)

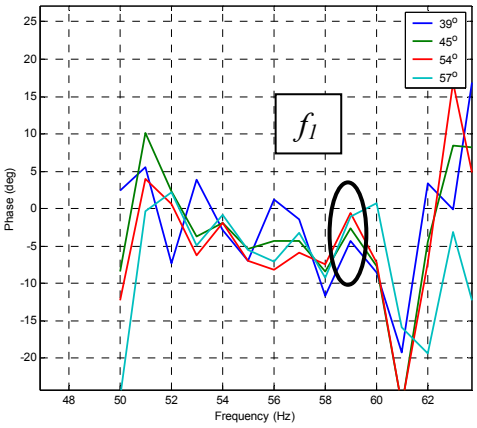

(b)

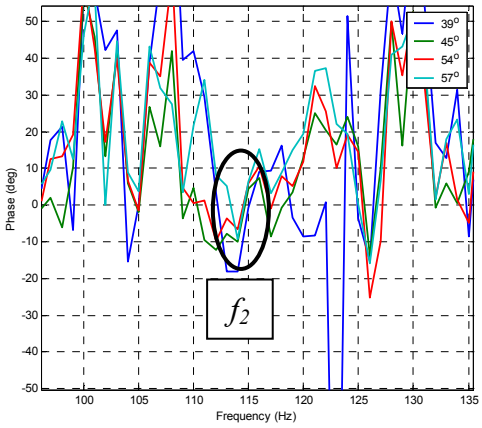

(c)

Figure 3.23: Phase Between Microphone at 3° and the Microphones at 39°, 45°, 54°, and 57° at Mach 0.55 1.2% Flow Control **(a)** Phase between 50-350 Hz **(b)** Phase at f_1 **(c)** Phase at f_2 **(d)** Phase at f_3 **(e)** Phase at f_4 **(f)** Phase at f_5 **(g)** Phase at f_6

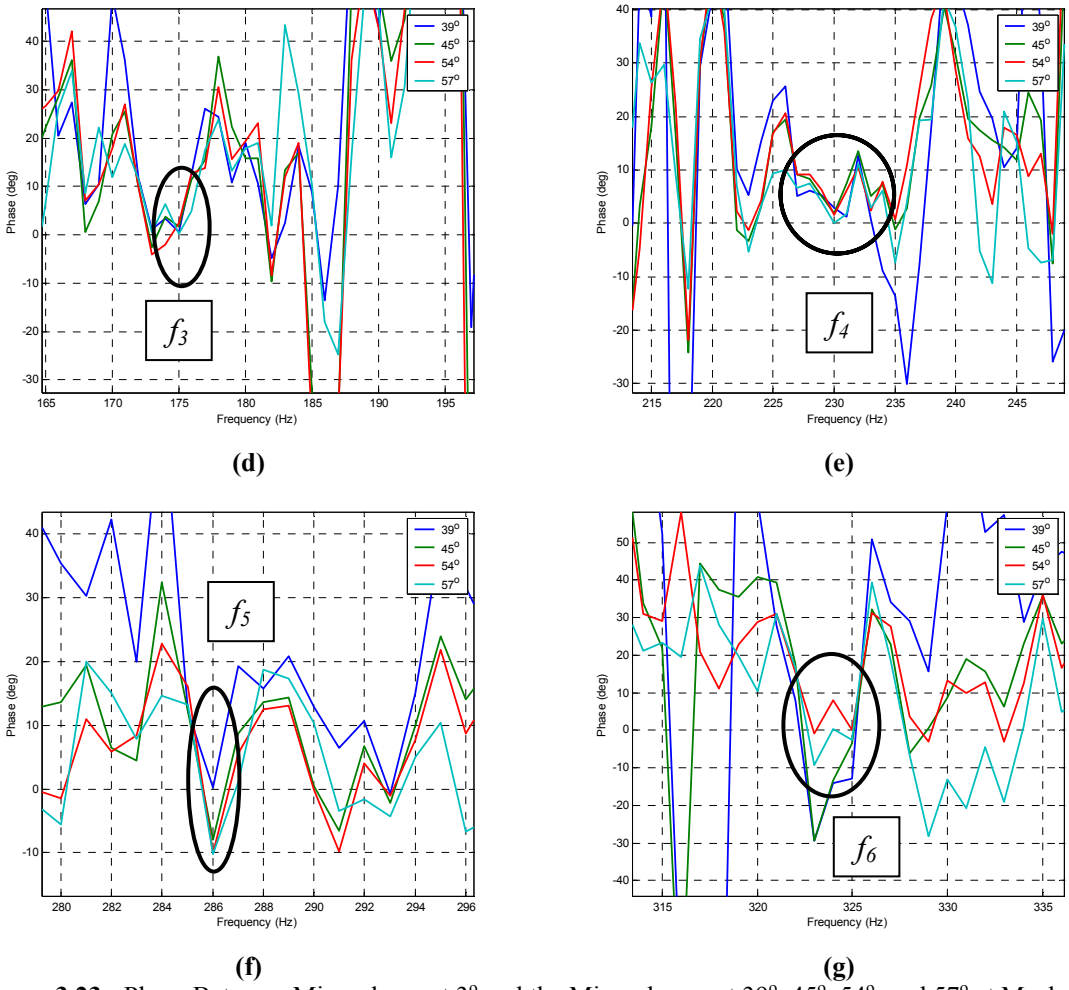

Figure 3.23: Phase Between Microphone at 3° and the Microphones at 39°, 45°, 54°, and 57° at Mach 0.55 1.2% Flow Control **(a)** Phase between 50-350 Hz **(b)** Phase at f_1 **(c)** Phase at f_2 **(d)** Phase at f_3 **(e)** Phase at f_4 **(f)** Phase at f_5 **(g)** Phase at f_6

3.5.4 Background Noise Effects on Distortion Observer

With an adequate estimate of the background noise affecting the microphone measurements, the biasing effects on the distortion observer were then assessed. Since the coherent content between the compared sensors was to be removed, the average coherences in Table 3.4 were the percent reduction in each of the four signals comprising *H*. These coherence values were used to calculate the acoustic-filtered *H*-values. A comparison of the original

acoustic-contaminated *H*-values with the filtered *H*-values at each control effort for the Mach 0.55 flow is shown in Figure 3.24. The comparison of the original (contaminated) distortion observer *H* with the filtered distortion observer (Figure 3.24) revealed that the acoustic disturbance was greater at lower control efforts. At the lower control efforts the jet exhaust from the inlet into the downstream plenum contained high levels of turbulence. Since the exhausted turbulent flow into the plenum provided acoustic excitation of the acoustic modes in the plenum, higher turbulence levels generated higher acoustic modal amplitudes in the downstream plenum. The effect of background acoustic noise removal on *H* was then assessed. The linear correlation between *H* and *DPCP* was assessed by the agreement to a linear fit between these two parameters. The contaminated and filtered *H*-values are plotted versus the corresponding *DPCP* values in Figure 3.25, and the agreements to linear curve-fits are presented for both data sets. As shown previously the unconditioned (contaminated) *H* demonstrated a 97% agreement to a linear fit. With the implementation of acoustic noise filtering, the linearity between *H* and *DPCP* modestly improved to 98%. Although the acoustic filtering does improve accuracy in predicting *DPCP*, the improvements were not enough to justify the additional signal processing of this technique for the real-time demonstration of the control system. More importantly, the filtered results in Figure 3.25 fall within the standard deviation of the contaminated *H*-values, which makes these signals statistically indistinguishable. Therefore, the control system to be demonstrated in Chapter 4 did not incorporate the acoustic background noise filtering technique. In an actual inlet/engine configuration the acoustic contamination will not pose a problem for the sensing scheme proposed in this chapter, mainly because there are no plenum chambers in an actual configuration.

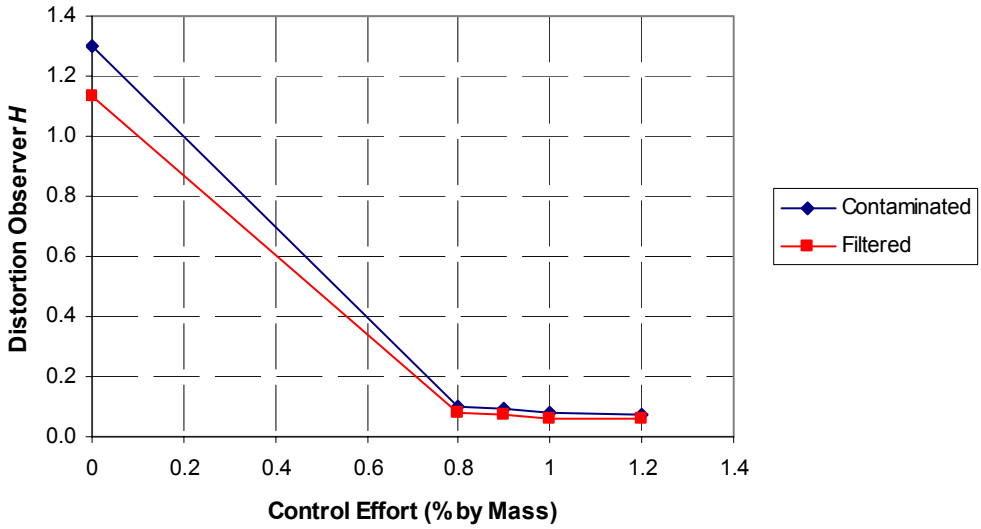

(a)

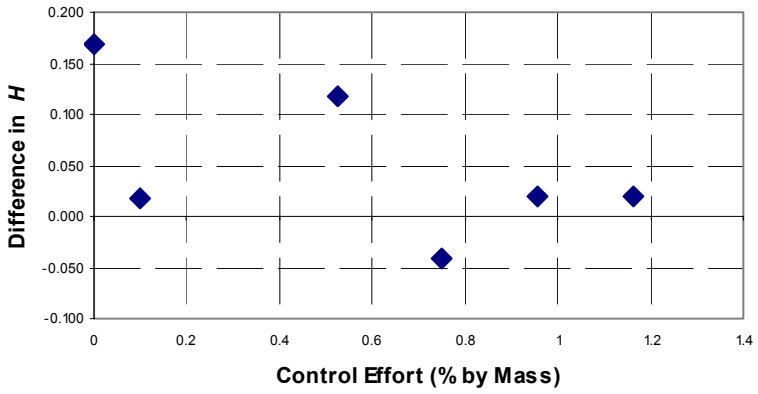

(b)

Figure 3.24: (a) Comparison of Acoustic-Contaminated and Filtered Distortion Observers *H* at Various Control Efforts, and **(b)** Difference Between Contaminated and Filtered *H*-values at Mach 0.55

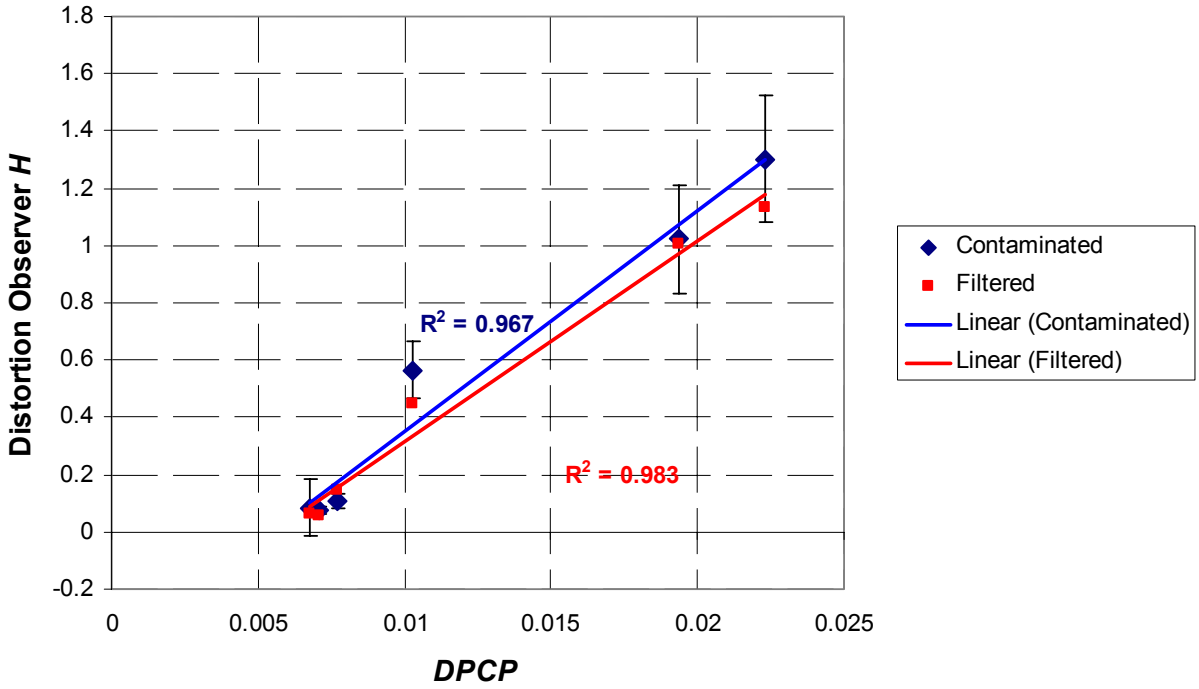

Figure 3.25: Acoustic-Contaminated and Filtered Distortion Observers *H* vs. *DPCP* at Mach 0.55

3.6 Summary

A non-intrusive method of sensing the circumferential distortion intensity using wall-pressure fluctuation measurements was proposed in this chapter. A basic understanding of internal flows explains that secondary flows are responsible for the accumulated turbulent, low-momentum flow regions at the serpentine inlet exit plane. In addition, the large-scale coherent turbulent structures have been identified by the research community to be responsible for the mean flow energy dissipation. As this was the case, monitoring the amplitudes of the large-scale turbulence responsible for total pressure loss served as the basis for this sensing strategy. Wall-

mounted microphone signals and inflow total pressures were recorded in response to a secondary flow control technique developed by Lockheed Martin. Experimental results revealed that a minimal set of four microphones could be used to observe the flow control's ability to thwart the secondary flow development that creates flow distortion. This microphone-based signal correlated well with *DPCP* values measured, and was expected to serve well as a distortion observer in the feedback loop of an automated distortion control system. As a final measure this microphone-based distortion observer was analyzed for its sensitivity to background acoustic disturbances unrelated to the turbulent mechanisms of total pressure dissipation. It was discovered that acoustic noise removal only improved the correlation between *H* and *DPCP* by a modest 1%. As a result the added signal processing required to remove the acoustic disturbances was not warranted for the real-time control system demonstration.

Chapter 4

SISO Microphone-Based Flow Distortion Control System

This chapter describes the development of a SISO microphone-based distortion control system. In the first section of this chapter, the structure of distortion feedback control system is described. The feedback loop of this control system was based on the circumferential distortion parameter (*DPCP*) linear observer presented in Chapter 3. Then the plant dynamics are presented as a basis for the PID compensator design. The third section discusses the PID compensator that was designed to achieve quick and accurate response time, as well as robustness with respect to plant changes such as sudden inlet flow speeds. Finally, this chapter concludes with the successful results from the experimental demonstration of the control system.

4.1 Closed-Loop System Structure

4.1.1 Control System Architecture

Since the distortion observer creates a single value *H* that estimates *DPCP*, the controller was reduced to a simple SISO system. A classical feedback system was chosen as the method to control the vortex generator flow affecters in order to achieve desired *DPCP* levels. The block diagram of the feedback distortion control system is shown below in Figure 4.1. A PID-type compensator was favored because it could be easily tuned for effective control performance.

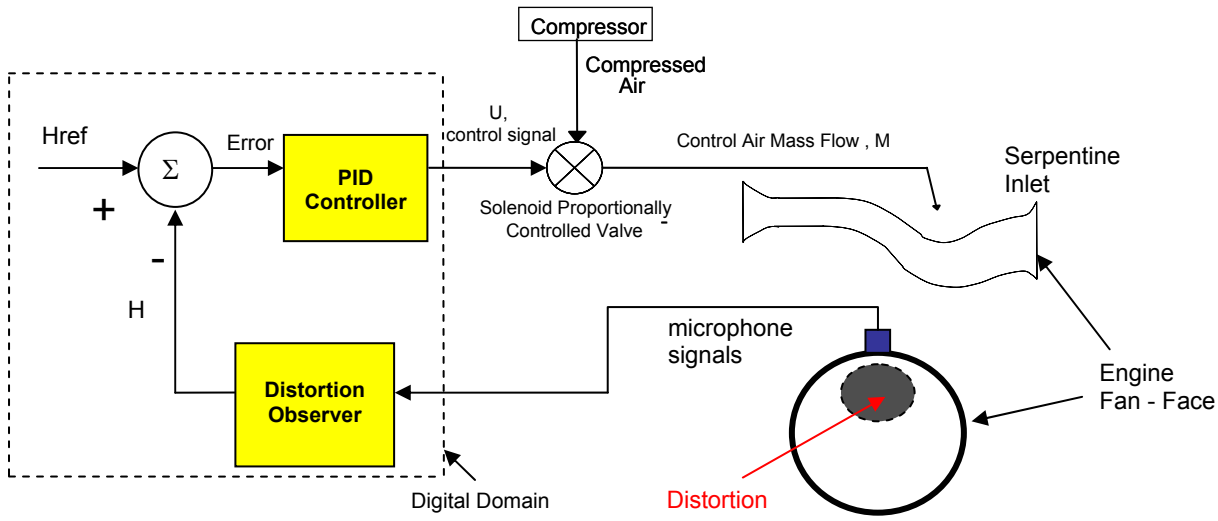

Figure 4.1: Block Diagram SISO Distortion Feedback Control System

The correlation analysis in Section 3.4 already provided the steady-state relationship between *H* and *DPCP*. Successful implementation of this feedback approach required an understanding of the actuator and plant dynamics, as well as the sensor dynamics in response to

the plant changes. With regard to this system, the actuator was the combination of the proportionally-controlled solenoid valve, the control air-supply compressor, and all of the capacitance associated with the plumbing that delivered the control-air to the inlet. The plant dynamics were composed of the fluid dynamics that created the spatial total pressure distortion at the AIP, which was characterized by the *DPCP* parameter. The final unknown dynamic component was that of the speed of the microphone responses to the changing plant dynamics. Since the dynamics of all three unknown components would be ultimately cascaded in the forward loop of the control system, these dynamics were lumped together and treated as a single "black box". The cascaded dynamics of the plant model are illustrated in Figure 4.2. Thus, a single transfer function *G(s)* (Figure 4.2) between the control voltage to the valve *U* and the observer estimate *H* was to be determined for the design of the appropriate PID compensator.

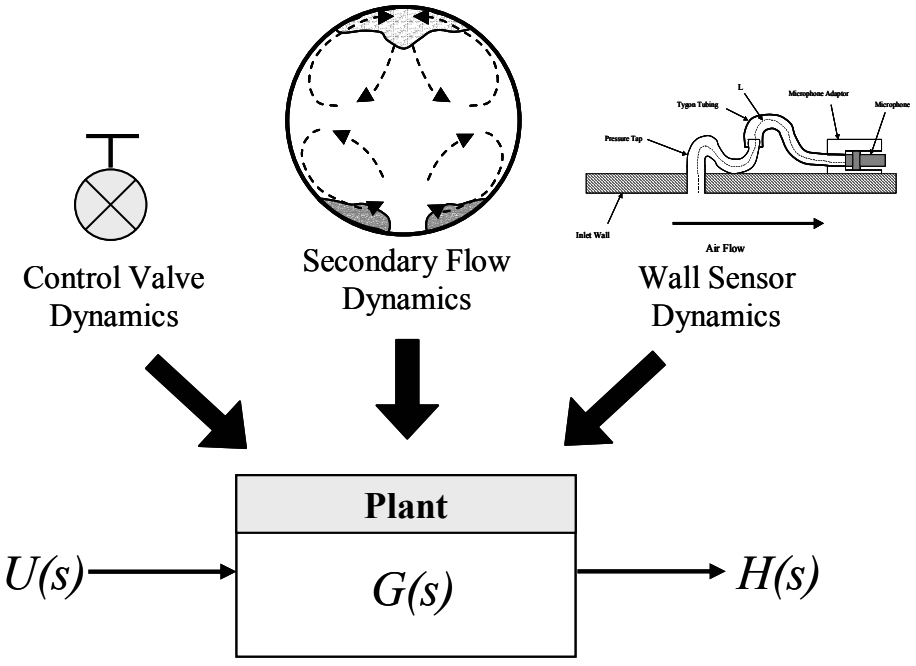

Figure 4.2: Plant Transfer Function *G*

The dominance of each dynamic component could be prioritized. Considering that the distance between the flow affecters and the AIP is approximately 0.33 meters and the flow speed of Mach 0.55, the time delay for the sensors located at the AIP to sense the effects of the flow control was on the order of thousandths of a second. These fast dynamics would obviously not dominate the overall dynamics of this system. Each microphone has a response bandwidth of 20-kHz, but the slowest frequency used for feedback was 50-Hz. Finally, the valve was known to have a bandwidth response on the order of 10-Hz, which made its dynamics dominate the overall system response.

4.1.2 Control System Hardware

4.1.2.1 Feedback Signal Processing

The feedback microphone signal processing is shown in Figure 4.3.

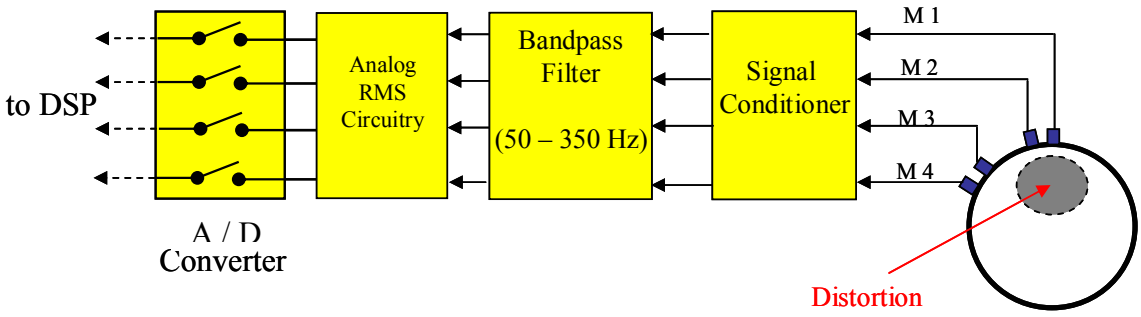

Figure 4.3: Feedback Signal Processing

A PCB® model 584A signal conditioner provided the PCB® model 106B high intensity microphones with a 22 VDC, 20 mA excitation. The signal conditioner also provided a gain of 20 to the microphone output signals to better fill the voltage dynamic input range of the A-to-D converter. These microphone voltage signals were then passed through a band-pass filter with corner frequencies at 50 and 350 Hz. The RMS of the filtered fluctuating microphone signals was then obtained with an analog RMS-calculating circuit. The circuit diagram of the RMS-calculating circuit is shown in Figure 4.4. This circuit is based on an Analog Devices® AD736 true RMS-to-DC converter monolithic integrated circuit, and requires the insertion of an averaging capacitor as a feedback loop for the circuit (C_{av} in Figure 4.4). The capacitance C_{av} dictates the dynamic speed of response for this circuit. The RMS microphone signals are finally passed into the A/D board of the DSP.

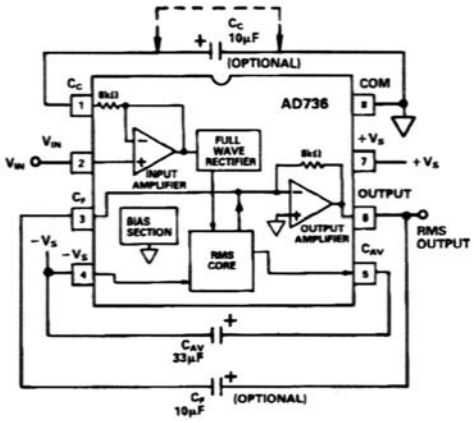

Figure 4.4: Analog RMS-Calculating Circuit

4.1.2.2 Forward Loop Signal Processing

The control air delivered to the jet-type vortex generator flow affecters was regulated by a Mark 70 Series pneumatic control valve manufactured by Jordan Valve®. This normally-closed valve is operated by a pneumatic positioner requiring an input pressure signal between 12 to 24 psi for full range of operation. In order to control the pneumatic valve electronically, the system required a current-to-pressure transducer. This was basically a small, calibrated valve that required an electrical input signal between 4-20 mA to regulate output pressures between the 12-24 psi necessary to open the control valve. Unfortunately, the control voltage signal from the DSP was output between +/- 8.2 VDC at only a few milliamps. In order to meet the current demands of the current-to-pressure transducer, the control signal from DSP was passed through a non-inverting operational amplifier circuit. The non-inverting amplifier circuit diagram is shown in Figure 4.5 [30]. With proper selection of R_1 and R_2, a signal gain A_v of 10 was achieved according to:

$$A_v = \frac{U}{V_{DSP}} = 1 + \frac{R_2}{R_1} = 1 + \frac{900\,\Omega}{100\,\Omega} = 10 \tag{4.1}$$

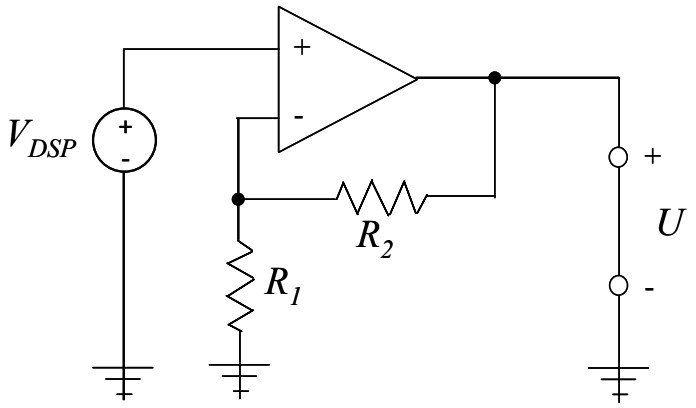

Figure 4.5: Non-Inverting Operational Amplifier Circuit

4.2 Determination of System Dynamics

It was important to gain an understanding of the system dynamics, so that a proper PID compensator could be tailored to reshape the system dynamics. The system dynamics between the control voltage input to the valve and the feedback signal *H* were determined experimentally. Step voltage signals *U* were input to the control valve exciting the dynamics of the system. Comparison of the response in *H* to the known step input enabled the construction of the transfer function between *U* and *H* (which is defined as *G*). Table 4.1 summarizes the amplitudes of the voltage step inputs to determine the system dynamics.

Table 4.1: Control Voltage Step Inputs for System Identification

U (Volts)	Mach 0.4 control (mass %)	Mach 0.5 control (mass %)	Mach 0.55 control (mass %)
5.9	0	0	0
6.3	0.126	0.096	0.099
6.8	0.648	0.555	0.524
7.2	0.931	0.791	0.751
7.6	1.180	0.991	0.954
7.9	1.446	1.228	1.163

This range of control voltage step inputs of *U* (Table 4.1) was sent to the valve to reveal any nonlinearities of the response in *H*, and to also provide the dependencies of *H* to the inlet throat Mach number.

4.2.1 Steady-State System Dynamics

The average of all the steady-state time responses of H to the step inputs described in Table 4.1 were shown in Figure 3.16. It was clear from the responses at each Mach number that the system was not linear over the entire range of control efforts. H becomes despondent at control efforts greater than 0.8% for all three Mach numbers tested, which also happens to be true for the *DPCP* values as well. Since H shows minimal response to flow control above 0.8%, the control system was not commanded to achieve reference levels H_{ref} below this lower response threshold. The control system was designed to perform at less than 0.8% control effort, as this was the linear response region as seen from Figure 3.16.

After inspection of the system frequency response functions obtained from the step input experiments, it was decided that a 2nd-order model of the system dynamics of the form

$$H(s) = \frac{-g_{ss}\ \omega_n^2}{s^2 + 2\ \zeta\ \omega_n\ s + \omega_n^2} U(s) + F \tag{4.2}$$

would be adequate for the PID compensator design [31]. Overall there were four unknown terms to identify in creating the 2nd-order plant model of Equation 4.2. The terms $-g_{ss}$ and F described the steady-state system response. Application of the final value theorem to Equation 4.2 for a step input with amplitude of A produced the following linear expression for the steady-state response H_{ss}:

$$U(s) = \frac{A}{s}$$
$$\lim_{t\to\infty} h(t) = \lim_{s\to 0} \; s\; H(s) = H_{ss} \tag{4.3}$$
$$H_{ss} = -g_{ss} A + F$$

Interpretation of this expression (Eq. 4.3) showed that the steady-state gain $-g_{ss}$ is simply the slope of the steady-state system response, and the drift term F is the y-intercept of the steady-state system response. Both terms were identified by performing a least-squares curve-fit analysis on the steady-state results, which is shown in Figure 4.6. The response at each Mach number suggested that the system could be considered linear with a high level of confidence because of the high R^2-values. The plant steady-state response terms (g_{ss} and F) that resulted from the linear curve-fit in Figure 4.6 are presented in Table 4.2 . Given the linear nature of this system, the PID control design simulations were expected to accurately predict the closed-loop responses.

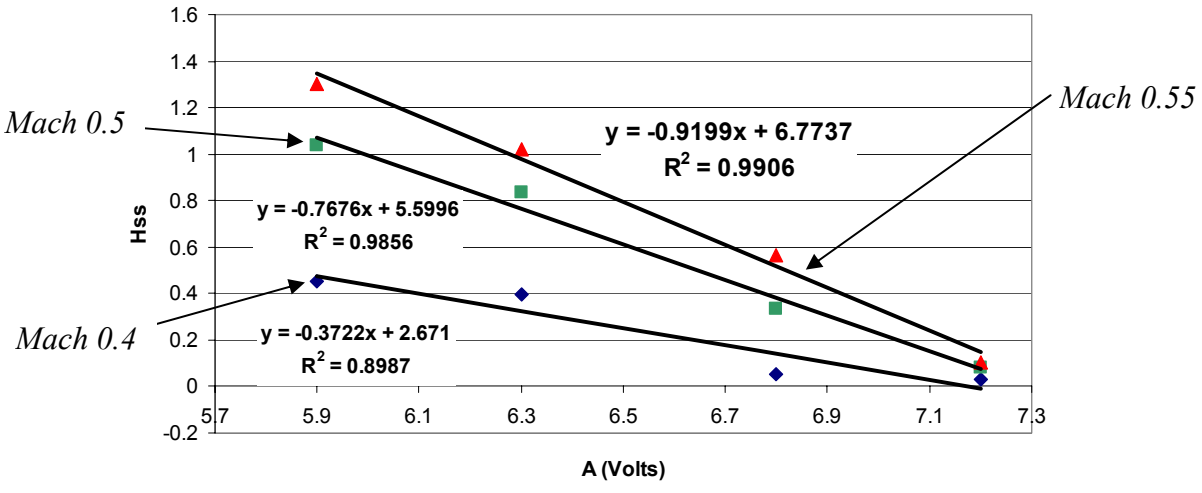

Figure 4.6: Steady-State Curve-Fit Analysis

Table 4.2: Plant Steady-State Response Terms at each Mach Number

Mach	g_{ss}	***F***	R^2
0.4	-0.372	2.671	0.899
0.5	-0.768	5.600	0.986
0.55	-0.920	6.774	0.991

4.2.2 Plant Dynamic Response

The frequency response functions (FRF) from the step input experiments were analyzed to determine the natural frequency and the damping ratio of the 2nd-order plant model. The averaged frequency response shown in Figure 4.7 indicates a natural frequency located approximately at 3 rad/s. This is evidenced by the -90° phase relationship at 3 rad/s. Due to a poor frequency resolution, the damping ratio became difficult to determine from the FRF; therefore, the damping ratio was determined to be 0.7 from visual inspection from the time domain step responses.

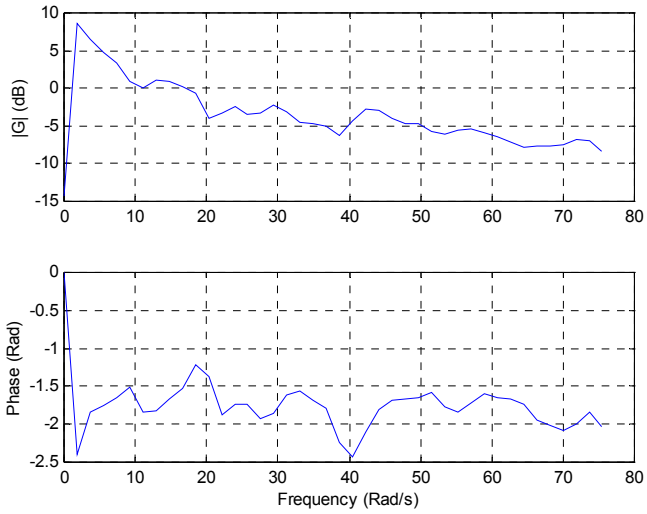

Figure 4.7: Average FRF of Plant *G*

4.3 PID Compensator Design

The basic PID control law in the continuous domain can be expressed as

$$u(t) = K_P e(t) + K_I \int e(t)dt + K_D \frac{de(t)}{dt} \tag{4.4}$$

where K_P, K_I, and K_D are the proportional, integral, and derivative control gains respectively. Application of Euler's discrete derivative approximation twice to the continuous PID control law (Eq.4.4) yields a finite difference representation that introduces the control sampling frequency

as a fourth design parameter in addition to the three control gains. With the z-transform this finite difference equation was transformed into the discrete frequency domain, and algebraic manipulation led to the discrete PID transfer function [32]:

$$D(z) = \frac{\left(K_P + K_I T + K_D/T\right)\ z^2 + \left(-K_P - 2K_D/T\right)\ z + K_D/T}{z\ (z-1)} \tag{4.5}$$

The primary PID design objective for this system was to place both zeros of *D(z)* below the plant natural frequency of 3 rad/s. The PID transfer function introduces phase and amplifies the feedforward dynamics at frequencies above the faster zero. Thus, placement of both zeros below ω_n introduced phase margin to the feedforward dynamics, which provides system stability through damping. Another benefit from the design objective was caused by the gain increase above the faster zero, which flattens the magnitude of the feedforward frequency response near the crossover frequency. A flat frequency response near the crossover desensitizes the system response speed to possible changes in the plant dynamics [33]. The zeros of the PID transfer function (Eq. 4.5) are given by:

$$D(z) = \frac{K(z - z_1)\ (z - z_2)}{z\ (z-1)}$$

where,

$$K = \left(K_P + K_I T + K_D/T\right) \tag{4.6}$$

$$z_{1,2} = \frac{\left(K_P + 2\ K_D/T\right) \pm \sqrt{K_P^2 - 4K_D K_I}}{2K}$$

An attempt to solve for the control gains that would place both zeros below 3 rad/s, but the zeros were determined by all three control gains simultaneously (Eq. 4.6). As a result of this coupling, the control gains that satisfied the design constraint were iteratively solved. The optimal set of control gains in terms of the settling time metric were determined at a few selected proportional gains and presented in Table 4.3. The control system responses for a step change in the desired feedback level from 1.6 down to 0.08 were simulated in order to identify which PID control gains provided the quickest and most stable response. These closed-loop step responses are shown in Figure 4.8. This change in command level equated to a change in *DPCP* from 0.023 to 0.007, effectively reducing circumferential distortion by 66%.

Table 4.3: Selected PID Compensators for Control System Simulation

K_P	K_I	K_D	T_S (sec)
2.0	3.0	0.30	0.70
4.0	4.0	0.55	0.51
6.0	4.0	0.75	0.44
8.0	4.0	0.90	0.39
10.0	4.0	1.0	0.36

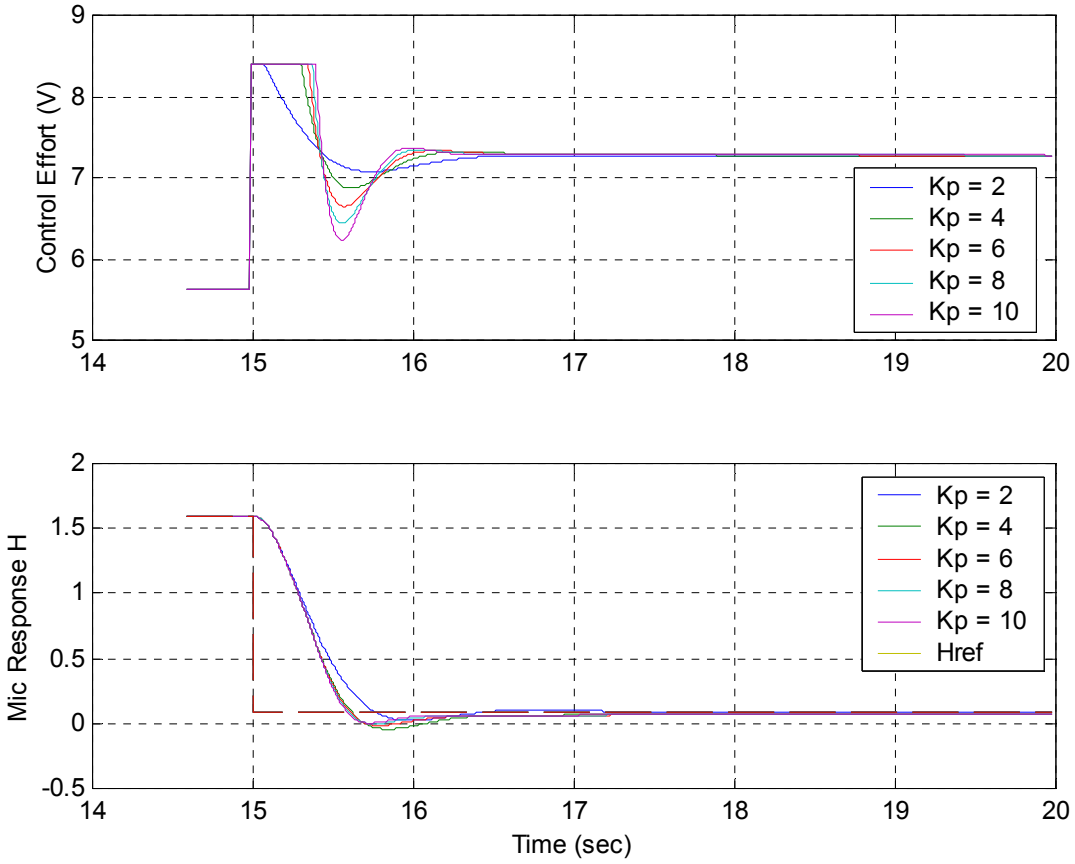

Figure 4.8: Simulated Control System Step Responses

The nonlinearity of the control signal saturation caused by the current limits on the current-to-pressure transducer was incorporated into these simulations (Figure 4.8). As expected the higher proportional gains created tremendous overshoot in the control efforts, which were clipped by the current limiter. Instabilities were speculated to result from the severe clipping. The compensator design associated with a K_P of 2 was expected to yield the most favorable responses, since it demonstrated the least amount of clipping.

4.4 Control System Results

4.4.1 Closed-Loop Step Response

Requesting a quick response to sudden changes in control effort simulated the control system's ability to be immediately activated during the event of a flight maneuver that jeopardizes engine operability. The control system was requested to bring the observation *H* from 1.6 down to 0.08, which corresponded to a change in *DPCP* level from 0.023 down to 0.007 (a 66% reduction in circumferential distortion), as quickly as possible. System responses were expected to match the simulated responses from Figure 4.8. The closed-loop step responses for the systems compensated with the following PID controllers $K_P = 2.0$, $K_I = 3.0$, $K_D = 0.0$ and $K_P = 2.0$, $K_I = 3.0$, $K_D = 0.3$ are shown in Figures 4.9 and 4.10. As anticipated, only the compensators with proportional gains less than or equal to 2 produced unstable step responses. The system shown in Figure 4.9 demonstrated a ringing response associated with overshoot, resulting in a settling time based on 2% of the final value of slightly less than 2 seconds. As an attempt to create a more "deadbeat" response, the damping was in creased for the second experiment by increasing K_D to 0.3. This "deadbeat" system settled in approximately 1 second to the stepped control command (Figure 4.10). When this system is eventually integrated into an aircraft, the plumbing of the control air delivery to the jet-type VG's will be much shorter than the plumbing network used for this research (see Section 2.5). The shorter plumbing in the actual aircraft will reduce actuation delay, and consequently improve the system speed of response.

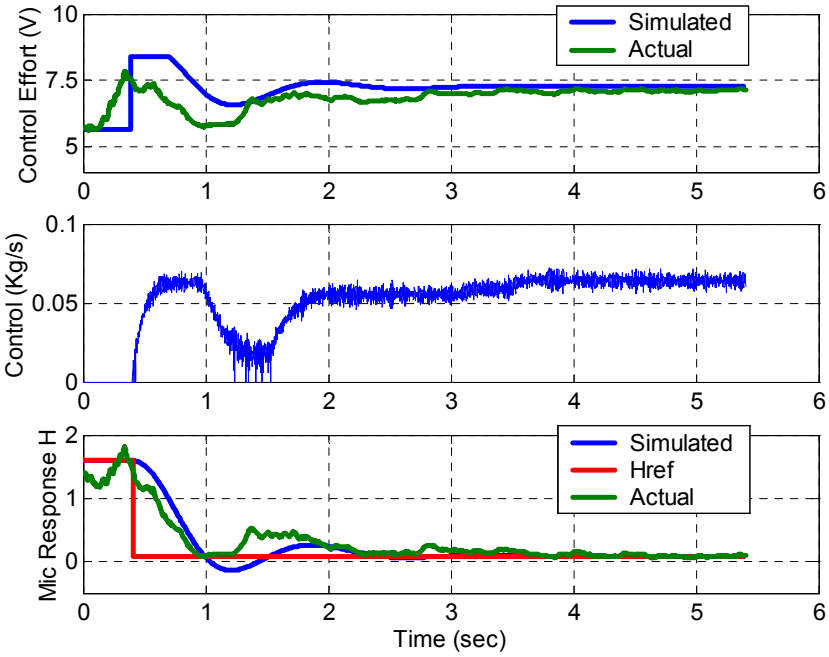

Figure 4.9: Step Response with $K_P = 2.0$, $K_I = 3.0$, $K_D = 0.0$

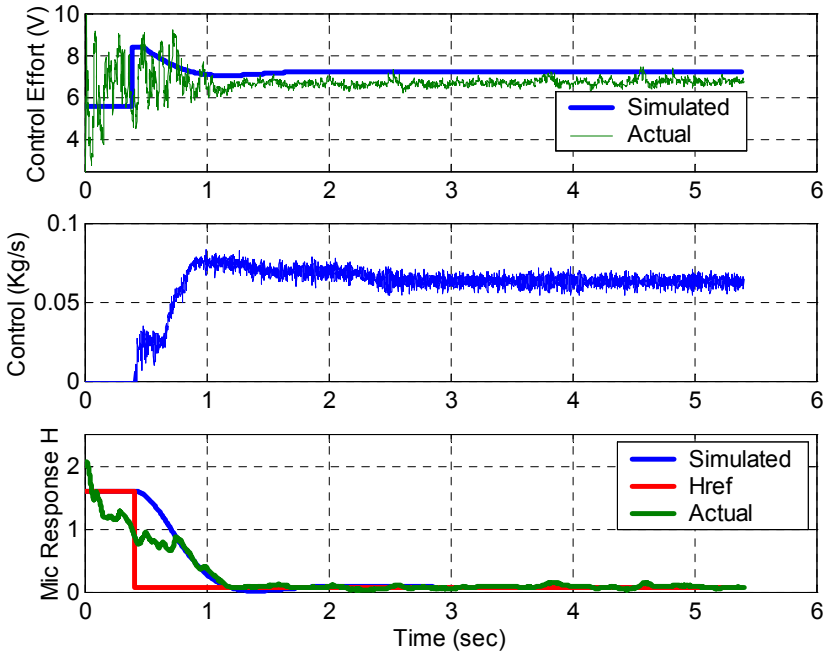

Figure 4.10: Step Response with $K_P = 2.0$, $K_I = 3.0$, $K_D = 0.3$

4.4.2 Distortion Control During Sudden Flow Speed Changes

In addition to providing a quick response to sudden changes in control level commands, the system also needed to demonstrate the ability to maintain a set distortion level during sudden flow speed changes. The jet engine, which pulled the airflow through the test inlet, was quickly ramped down and then up to test the control system's ability to hold the desired *DPCP* level of 0.007 (H = 0.1). The compensator ($K_P = 2.0, K_I = 3.0, K_D = 0.3$) that yielded the step response with the best settling time was first tested for its insensitivity to sudden flow speed changes (Figure 4.11). During the ramp-up in flow speed, the PID controller suppressed the *DPCP* to a maximum overshoot level of 0.009, compared to the desired *DPCP* of 0.007. The flow control system prevented the *DPCP* from even remotely approaching the dangerously high uncontrolled *DPCP* level of 0.023. With this excellent control system response, this distortion sensing and control system was established as a viable technology to improve the operability of a jet engine coupled to a serpentine inlet while performing aircraft accelerations.

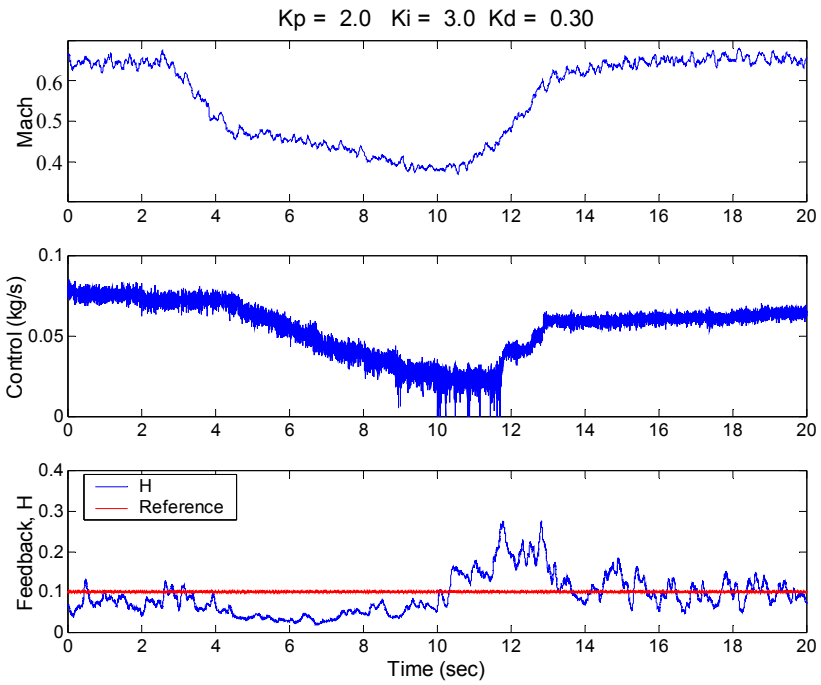

Figure 4.11: Flow Speed Change Response $H_{ref} = 0.1$ and $K_P = 2.0$, $K_I = 3.0$, $K_D = 0.3$

4.5 Summary

This chapter described the development of an automated system capable of non-intrusively sensing and controlling circumferential total pressure distortion in serpentine inlets. The feedback loop of this control system incorporated an observer of the circumferential

distortion parameter *DPCP* using wall-pressure fluctuation measurements from strategic locations pertinent to the symmetric, level flight condition, which was developed and validated in Chapter 3. After experimental determination of the system dynamics, a PID compensator was designed that achieved a requested 66% reduction in *DPCP* (from *DPCP* of 0.023 down to 0.007) in less than 1 second. This control system was also tested for its ability to maintain a *DPCP* level of 0.007 during a quick ramp-down and ramp-up engine throttling sequence, which served as a measure of system robustness. The control system allowed only a maximum peak *DPCP* of 0.009 during the engine ramp-up. The automated distortion control demonstrations described in this chapter have shown the great potential of applying this distortion sensing and control to military aircraft with serpentine jet engine inlets.

Chapter 5

A Wall-Pressure Sensing Technique to Infer Optimal Active Flow Control with Two Flow Affecters

The ability to employ non-intrusive, wall-pressure sensors to infer total pressure distortion control by a single array of jet-type vortex generators has been successfully demonstrated in Chapters 3 & 4. The vortex generator array used thus far affected the flow region in the top-half of the AIP. Lockheed Martin expanded the system capabilities by adding a second array of jet-type vortex generators further upstream in the inlet to control the secondary

flow plaguing the total pressure distribution in the bottom-half of the AIP, which is explained in Section 5.1. The efforts to expand the wall-pressure sensing technique to accommodate an inlet with two flow affecters are presented in Section 5.2. This inlet with two flow affecters also has a lower length-to-diameter ratio, and it was tested in a Lockheed Martin Test facility which differed from the Virginia Tech / Techsburg inlet test facility. The Lockheed Martin inlet test facility was capable of achieving an inlet throat Mach number of 0.7, as compared to the maximum 0.55 Mach number in the Virginia Tech / Techsburg inlet test facility. The combination of control efforts from the forward and aft affecters that provided an optimal compromise between the achieved inlet performance indices, circumferential distortion intensity and average pressure recovery, and the required control efforts were determined to serve as a baseline for the non-intrusive sensing technique. A wall-pressure-based sensing technique was sought after that could identify these optimal control efforts. This new wall-pressure sensing technique was not merely a distortion observer; rather, it was intended to be an overall inlet performance observer, which considers both of the inlet performance indices at the expense of the control efforts. Finally, this chapter concludes by proposing the layout of an automatic MIMO control system that incorporates this new sensing technique.

5.1 Regions of Controllability with Two Flow Affecters

The secondary flow as described in Chapter 1 is responsible for accumulating the low-momentum fluid in several regions of the AIP (Figure 1.5). The added vortex generator array

attempts to counter the secondary flow responsible for collecting the low-momentum fluid at the two lower lobes of the AIP. This flow affecter was positioned upstream to nullify the secondary flows from the first and third serpentine inlet bends. Because these control jets are introduced earlier into the inlet airflow, this injected air mass experiences greater diffusion as compared to the air mass from the downstream flow affecter. Thus, the upstream flow affecter actually controls the entire flow region at the AIP, and the downstream affecter still controls the flow in the upper portion of the AIP as before. The regions of control for each flow affecter are presented in Figure 5.1. Because both affecters control the airflow in the upper portion of the AIP, it was expected that wall-pressure sensors mounted in this sector would measure responses coupled to both affecters.

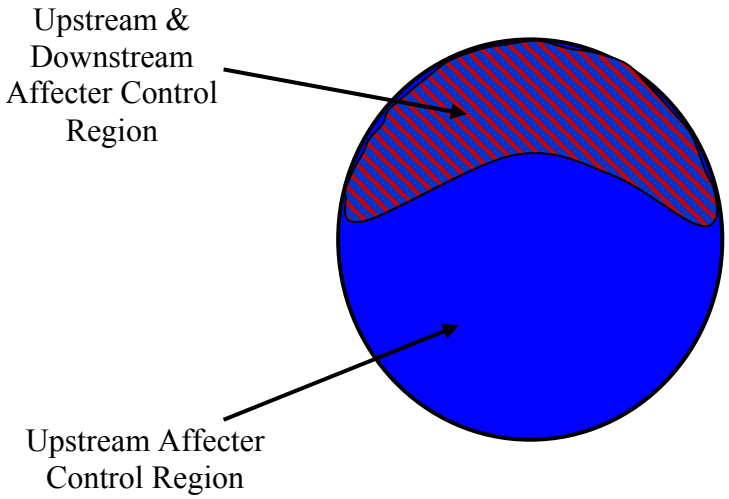

Figure 5.1: Flow Affecter Regions of Controllability

5.2 Optimal Control Efforts with Two Flow Affecters

The compatibility between this inlet, equipped with two flow affecters, and a jet engine compressor was assessed using total pressure measurements recorded at 80 radial and circumferential locations at the AIP. Inlet efficiency was assessed by the average pressure recovery *PR*, which was simply the average of the 80 AIP total pressure measurements normalized by the stagnation pressure upstream of the inlet entrance. In order to remain consistent with the aim of this sensing scheme, which was to predict total pressure losses, the average pressure deficit defined as

$$PD = 1 - PR \tag{5.1}$$

was used as the inlet efficiency metric. *PD* served as a measure of the average loss of total pressure in the inlet. The total pressure distortion was again characterized by the circumferential distortion intensity *DPCP*.

A series of experiments intended to map the inlet performance indices (*PD* and *DPCP*) as a function of variations in flow control efforts (Table 5.1) at Mach 0.5, 0.6, and 0.7 were conducted to determine the optimal control efforts. These optimal control settings that were to be determined directly from the AIP total pressure measurements would serve as the basis of evaluation for the proposed microphone-based inlet performance observer. The desired control settings at a given Mach number would need to achieve an optimal balance between the inlet performance indices and the required control efforts.

Table 5.1: Inlet Performance Assessment Experimental Matrix

Mach 0.7 Aft Jet (%) \ Fwd jet(%)	0.25	0.50	0.75	1.00
0.25				-
0.5				-
0.75				-
1				-
1.25				-

Mach 0.6 Aft Jet (%) \ Fwd jet(%)	0.25	0.50	0.75	1.00
0.25	-	-	-	-
0.5	-	-	-	-
0.75	-	-	-	-
1	-	-	-	-
1.25	-	-	-	-

Mach 0.5 Aft Jet (%) \ Fwd jet(%)	0.25	0.50	0.75	1.00
0.25	-	-	-	-
0.5	-	-	-	-
0.75	-	-	-	-
1	-	-	-	-
1.25	-	-	-	-

The AIP total pressure measurements were analyzed by Lockheed Martin [34], and the optimal control efforts were determined based on the *PR* and *DPCP* metrics. A formulaic approach was desired that could identify these optimal control efforts and serve as a model for a similar approach using microphone data as opposed to the aerodynamic data. A cost function of the form

$$J = Q_x\left(q_1 DPCP + q_2 PD\right) + Q_u\left(q_3 u_{fwd} + q_4 u_{aft}\right) \tag{5.2}$$

was developed with the intention of identifying the optimal control efforts according to Lockheed Martin [34]. This cost function was not required to have a quadratic form because none of the terms could be negative. Thus, a linear cost function was sufficient in guaranteeing a cost function with a positive global minimum. The optimal control setting was considered to be associated with the control efforts that minimized *J* (Eq. 5.2). The terms u_{fwd} and u_{aft} in Equation 5.2 represent the forward and aft control efforts in terms of the control air mass flow

rates as a percentage of the total inlet mass flow rate. The q and Q terms are weighting factors that prioritize the various terms compared in the calculation of J, and the q and Q terms were desired that yielded optimal control settings similar to Lockheed Martin's recommendations. The terms q_1 and q_2 allowed for the inlet performance indices to be prioritized, and these terms must satisfy the condition

$$q_1 + q_2 = 1 \tag{5.3}$$

For example if q_1 was equal to 1, *DPCP* would be given full priority in representing the inlet performance in the calculation of J. Likewise, the terms q_3 and q_4 allowed for prioritization of the control inputs u_{fwd} and u_{aft}, and were required to satisfy a similar condition where

$$q_3 + q_4 = 1 \tag{5.4}$$

Finally, the weighting coefficients Q_x and Q_u allowed for prioritization of either the inlet performance, or the required control effort respectively. Yet again, these weighting coefficients were to satisfy a similar condition where

$$Q_x + Q_u = 1 \tag{5.5}$$

For this cost function analysis the achieved inlet performance and the required control effort were considered to have equal importance, as a result both Q_x and Q_u were set to a value of 0.5. Similarly, both inlet performance indices were considered equally important, thus q_1 and q_2 were set to 0.5. As for the prioritization of the flow affecters, the forward affecter proved to

have a greater affect on the inlet performance. In the formulation of J (Eq. 5.2), a higher q-value inflates the level of J with respect to that parameter, thereby penalizing that particular parameter. With this in mind, the aft affecter control effort was penalized by setting q_{aft} to 0.7 and q_{fwd} to 0.3 accordingly. Using the aforementioned weighting coefficients, the following results in J were tabulated for Mach 0.5, 0.6, and 0.7 in Tables 5.2, 5.3, and 5.4 respectively. The optimum control settings, which are the minimum J-values, are highlighted with bold and italicized typefaces. These desired control settings then served as the basis for evaluation of the wall-pressure sensing technique.

Table 5.2: Cost Function *J* Results for Mach 0.5

Fwd jet(%) / Aft Jet (%)	**0.25**	**0.50**	**0.75**	**1.00**
0.25	0.711	0.767	1.196	1.254
0.5	0.732	0.782	0.829	0.962
0.75	0.736	***0.689***	0.699	0.844
1	0.810	0.732	0.772	0.818
1.25	0.778	0.717	0.882	0.914

Table 5.3: Cost Function *J* Results for Mach 0.6

Fwd jet(%) / Aft Jet (%)	**0.25**	**0.50**	**0.75**	**1.00**
0.25	0.778	0.698	1.326	0.870
0.50	0.796	0.753	0.829	0.934
0.75	0.826	***0.677***	0.697	0.798
1.00	0.810	0.783	0.788	0.840
1.25	0.862	0.779	0.852	0.928

Table 5.4: Cost Function *J* Results for Mach 0.7

Fwd jet(%) / Aft Jet (%)	**0.25**	**0.50**	**0.75**	**1.00**
0.25	0.609	0.802	1.053	1.042
0.50	0.716	0.908	0.847	0.836
0.75	0.821	0.770	0.727	***0.702***
1.00	0.937	0.839	0.823	0.815
1.25	1.036	0.982	0.899	0.960

5.3 Wall-Pressure Sensor Responses to Flow Control with Two Affecters

This section describes the setup and implementation of the wall-pressure sensing study that was directed toward the development of a signal capable of directing a flow control system to the optimal control settings according to the cost function *J*. The placement of the sensor array is first described. Then spectral results from the array are presented to indicate the frequency band of interest. Finally, a smaller subset of the sensor array is proposed as the sensor set to be used for the non-intrusive inlet performance observer.

5.3.1 Sensor Array Placement

With the addition of the upstream flow affecter, the entire AIP flow field could now be controlled. In light of this, the preliminary sensing study was conducted with a 16-microphone array that spanned half of the AIP cross-section as shown in Figure 5.2. The symmetric flow field afforded the ability to place the microphones only on one half of the AIP cross section. The general locations of the spoiled airflow for an uncontrolled flow are shown as the dark grey

regions in Figure 5.2. Unfortunately, no AIP total pressure contours that could show the actual distortion patterns measured were released by Lockheed Martin for presentation. This entire array was recorded at varying control efforts and different Mach numbers to determine which sensors best captured the flow improvements in response to flow control. It was anticipated that monitoring the sensor responses closest to the uncontrolled spoiled airflow regions, namely the sensors at 0^o, 12^o, 24^o, 120^o, 132^o, and 144^o, would combine to serve as the best non-intrusive flow descriptor.

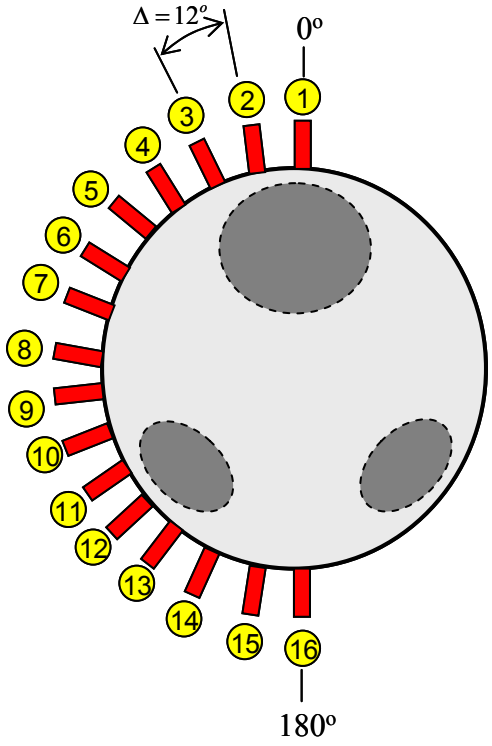

Figure 5.2: Sensor Placement (Spoiled, Low-Momentum Flow in Grey)

5.3.2 Motivations for Background Acoustic Noise Filtering

Since this experiment involving a serpentine inlet with two flow affecters was conducted in a different test facility from the one used for the material in Chapters 3 and 4, the wall-pressure signals were analyzed for potential acoustic disturbances. This new test facility contained a plethora of complicated geometries, which made analytical prediction of acoustic natural frequencies practically impossible. As this was the case, the coherence analysis of the microphone array served as the indicator for acoustic disturbances. The presence of acoustic disturbances becomes quite noticeable when high flow control efforts attenuate the turbulence levels. In light of this, the degree to which the acoustic disturbances affect the wall turbulence measurements was first analyzed for the optimal control case (u_{fwd} of 1.0% and u_{aft} of 0.75%) at Mach 0.7. The frequency range that demonstrated the highest wall-pressure fluctuations was 200-400 Hz, which will be shown in detail later. The coherence between the microphone at 0^o and the other 15 microphones of the array are shown in Figure 5.3 for the optimal control scenario at Mach 0.7 for the 200 to 400 Hz frequency band.

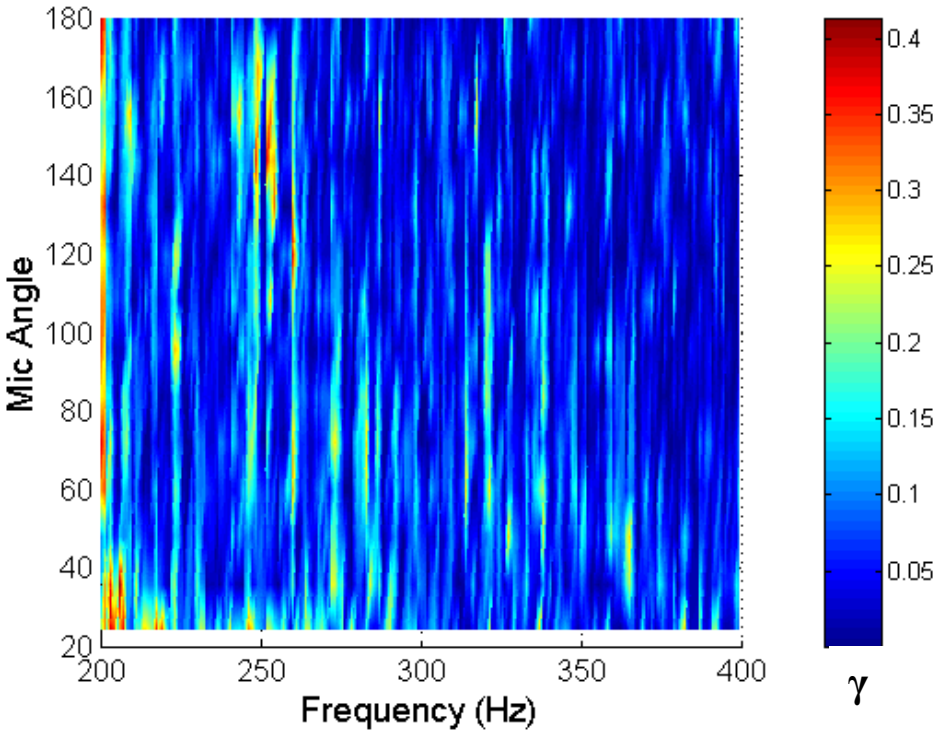

Figure 5.3: Coherence Between Microphone at 0° and all other Microphones in Array for Optimal Control Scenario at Mach 0.7

From this coherence analysis it was realized that the signals from the entire array were relatively correlated at specific frequencies primarily below 300 Hz. Since all the microphones demonstrated similar coherence levels at the same frequencies, it was impossible for the signal content at these frequencies to be purely turbulent. The consistent correlation across the entire array suggested that the array was detecting acoustic pressures from facility-related sources. The original and the acoustic-filtered RMS pressure spectra for the microphone at 0° are shown in Figure 5.4. Sharp tonals can be seen from the original microphone spectrum (Figure 5.4), which raises concern if these tones are turbulence-related. It is known that the random nature of the turbulence would not exhibit such a distinct tonal nature. The acoustic-filtered spectrum in Figure 5.4 does not contain these sharp tonals below 300 Hz. The correlated content between

locations at 0° and 48° was removed from the signal at 0°, which is ample span-wise spacing for these reduced turbulent length-scales, to produce this acoustic-free, turbulent spectrum.

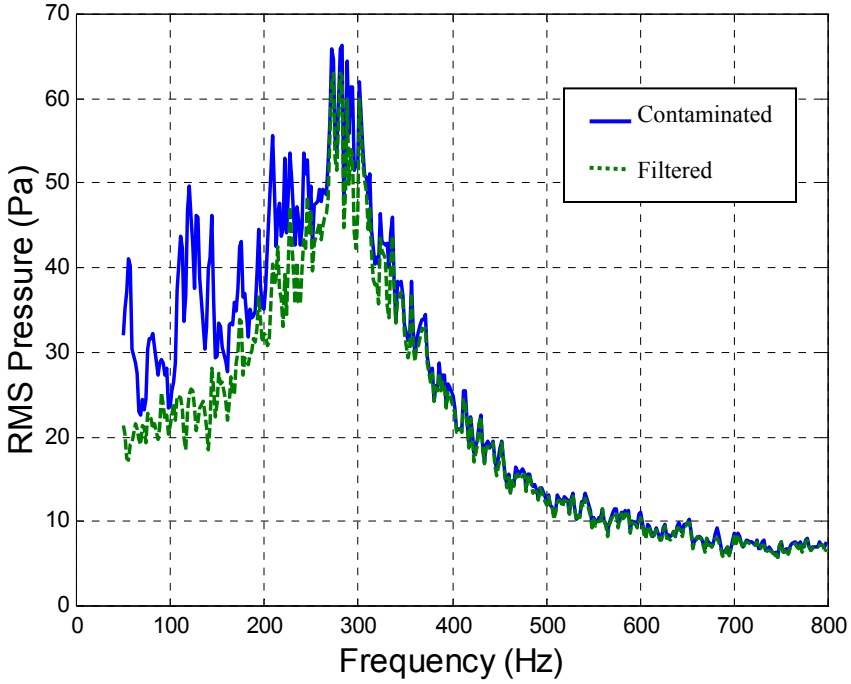

Figure 5.4: Comparison of Original RMS Pressure Spectrum with the Acoustic-Filtered Spectrum at Location 0° for the Optimal Control Scenario at Mach 0.7

As just shown, the wall-pressure fluctuation measurements were heavily biased by low-frequency, background acoustic disturbances at high levels of flow control. This was to be expected since the turbulence levels were greatly reduced by the flow control. As an unexpected turn of events, the wall-pressure measurements at low control efforts (high turbulence levels) were also vulnerable to the background acoustic disturbances. A similar coherence analysis for the low control efforts of 0.25% forward control and 0.75% aft control is shown in Figure 5.5. This coherence analysis demonstrated the same pattern of consistently high coherence across the entire array at specific frequencies. The contaminated and filtered RMS wall-pressure spectrums

recorded by the microphone at 0^o for the 0.25% forward control and 0.75% aft control scenario is shown in Figure 5.6. An appreciable difference between the acoustic-contaminated and the acoustic-filtered RMS wall-pressure spectrums can be seen in Figure 5.6.

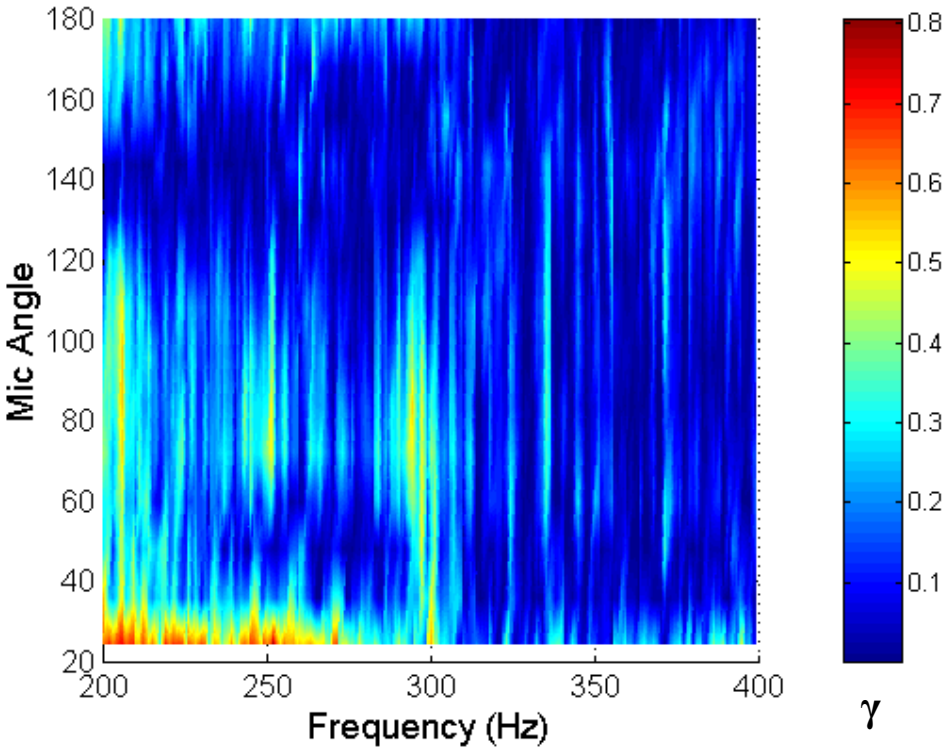

Figure 5.5: Coherence Between Microphone at 0^o and all other Microphones in Array Under Minimal Control Efforts at Mach 0.7

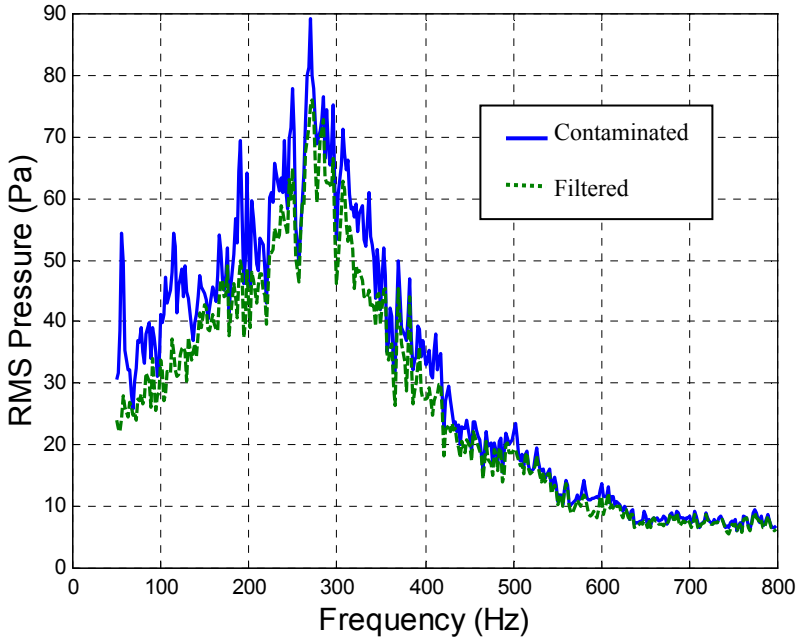

Figure 5.6: Comparison of Original RMS Pressure Spectrum with the Acoustic-Filtered Spectrum at Location 0^{o} Under Minimal Control Efforts at Mach 0.7

The appreciable biasing of the wall-pressure fluctuation measurements due to background sources in this new facility motivated the incorporation of a real-time, optimal filter into the proposed feedback signal that can remove the acoustic content. In addition, this sensing technique will need to reject the acoustic disturbances from a turbofan jet engine when this system is eventually implemented into an actual aircraft inlet. Since jet engines are capable of radiating higher-ordered modes when subjected to a distorted airflow, the addition of a real-time filtering scheme will be necessary to account for these constantly changing acoustic disturbances. The acoustic filtering technique implemented in this sensing technique derives from Naguib's et al. [23] optimal filtering method presented in Section 3.5. The caveat here will be that an adaptive LMS filter will serve as the optimal filtering technique as shown in Figure 5.7. This filter network will determine the content of a contaminated wall-pressure fluctuation

measurement p'_1 that is uncorrelated with a sufficiently-spaced span-wise wall-pressure fluctuation measurement p'_2. The sufficient span-wise spacing ensures that both sensors do not measure turbulent pressure fluctuations from the same turbulent sources, thus any correlated content will result from an external acoustic source. The adaptive filter determines the correlated content attributed to acoustic sources p'_a, and the correlated content is subtracted from the contaminated signal p'_1 to yield the true turbulent content at location 1 denoted as $p'_{t,1}$.

The span-wise spacing to be used for this analysis was determined to be 48^o. Since this spacing was to ensure that a single turbulent structure could not be detected by both wall sensors, the coherence analysis performed for the flow scenario with the largest turbulent structures would indicate the minimum sensor spacing. The largest turbulent structures existed for the highest flow speed and the least control effort, which was the minimal control effort scenario at Mach 0.7. The coherence results (Figure 5.5) for this case indicated that high coherence levels were confined to distinct frequencies at a spacing of 36^o. Based on this observation a conservative spacing of 48^o was chosen for the filtering technique.

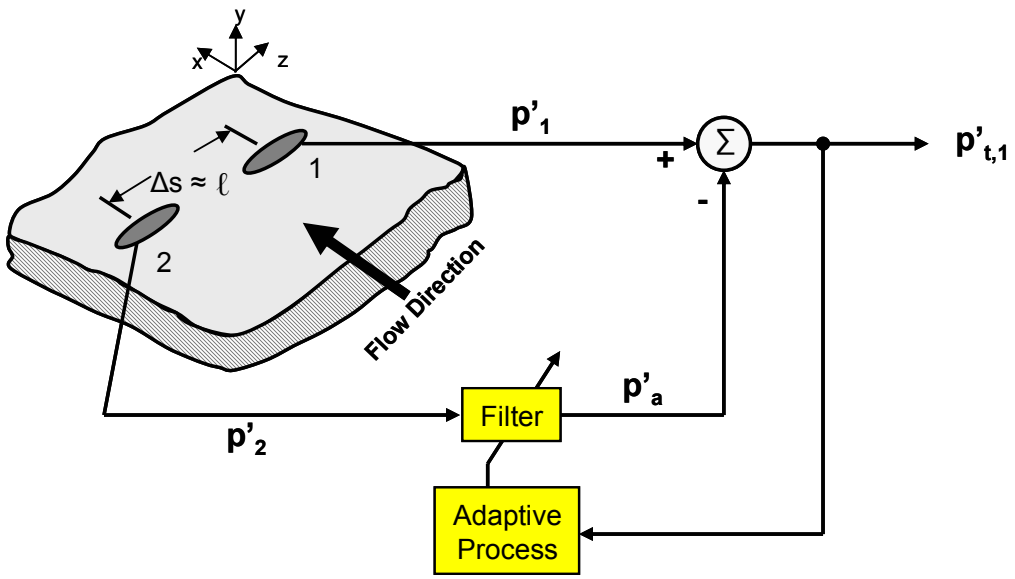

Figure 5.7: Adaptive Filter Network to Extract Facility Background Noise from Wall-Pressure measurements

5.3.3 Adaptive Filtering Basics

The basic adaptive filtering concepts are presented here to provide insight as to how the turbulent content was extracted. The basic adaptive network used for this background noise extraction technique is shown again in Figure 5.8 with the traditional generic variables. The FIR filter tap weights $\underline{w}_k$ are adapted by an LMS adaptation algorithm, in an attempt to create a filter output signal s_k that is correlated to the primary signal y_k.

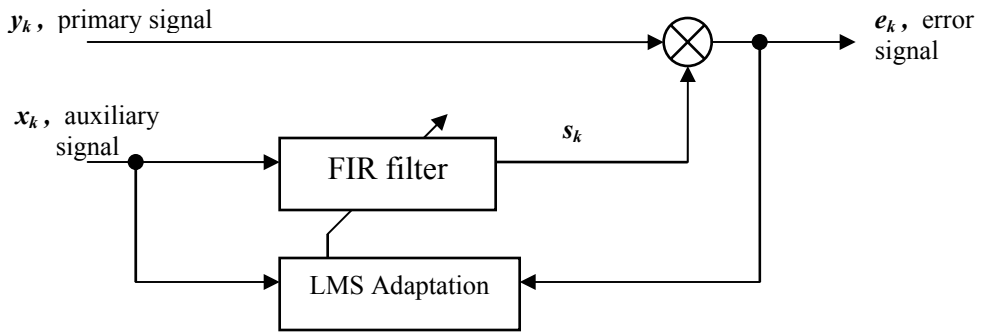

Figure 5.8: Noise Extraction Adaptive Filter Network

The adaptive FIR filter output s_k is given by

$$\hat{s}_k\left(\underline{w}\right) = \sum_{r=1}^{p} w_r\, x_{k-r} = \underline{x}_k^T\, \underline{w}$$

where,

$$\underline{w} = (w_1 \cdots w_p)^T$$

$$\underline{x}_k = (x_{k-1} \cdots x_{k-p})^T \tag{5.6}$$

The block diagram form of the FIR filter along with the adaptive block is shown in Figure 5.9.

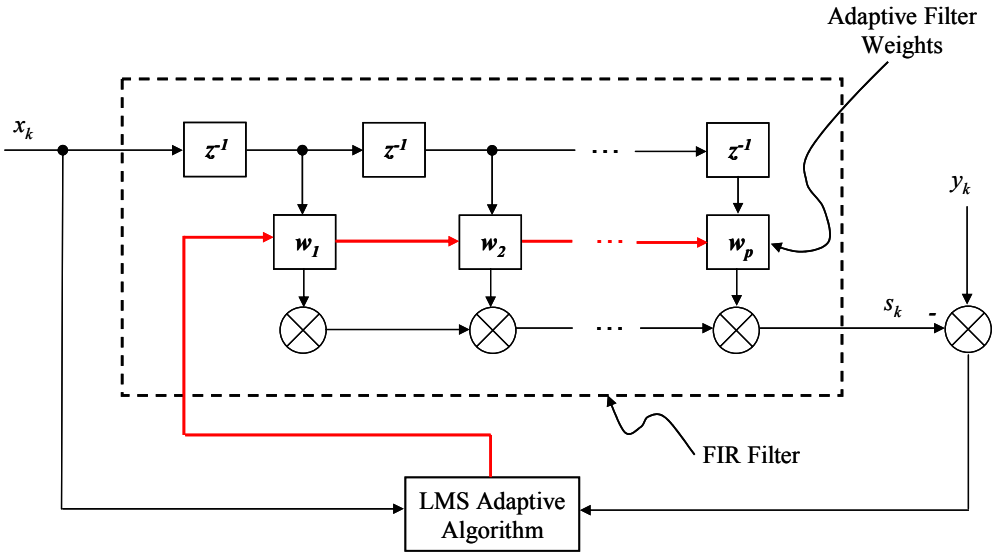

Figure 5.9: Adaptation and FIR Filter Block Diagram

The error signal is then developed in terms of the primary signal, auxiliary signal, and the adaptive filter weights as

$$\begin{aligned} e_k &= y_k - \hat{s}_k \\ &= y_k - \underline{x}_k^T \underline{w} \end{aligned} \tag{5.7}$$

Squaring the error function (Eq. 5.7) and then finding the statistically expected value results in the mean squared error (MSE) function which is shown as

$$\begin{aligned} \varepsilon = E[e_k^2] &= \left(y_k - \underline{x}_k^T \underline{w}\right)\left(y_k - \underline{x}_k^T \underline{w}\right) \\ &= E[y_k^2] - 2\underline{w}^T E[\underline{x}_k y_k] + \underline{w}^T E[\underline{x}_k \underline{x}_k^T]\underline{w} \\ &= R_y - 2R_{xy}^T \underline{w} + \underline{w}^T R_x \underline{w} \end{aligned} \tag{5.8}$$

The MSE function (Eq. 5.8) is a quadratic equation, which implies that a global minimum exists. Then differentiating Equation 5.8 with respect to $\underline{w}$ and equating it to zero results in

$$\underline{w}_o = R_x^{-1} R_{xy} \tag{5.9}$$

where $\underline{w}_o$ is the optimal filter weight vector. Further insight into the relationship between $\underline{x}_k$ and e_k can be gained by analyzing the expected results of $\underline{x}_k e_k$. This is conducted as

$$\begin{aligned} &E[\underline{x}_k y_k] - E[\underline{x}_k \, \underline{x}_k^T \underline{w}_o] = 0 \\ &E[\underline{x}_k]\left\{E[y_k] - E[\underline{x}_k^T \underline{w}_o]\right\} = 0 \\ &E[\underline{x}_k]E[e_k] = 0 \end{aligned} \tag{5.10}$$

This result concludes that the error signal is orthogonal or uncorrelated with the auxiliary signal. With this said, the error signal is the portion of the primary signal that is uncorrelated with the

auxiliary signal, an by induction the signal s_k is the portion of the primary signal that is correlated with the auxiliary signal.

Since the cross-correlation matrix R_{xy} in the MSE function is practically impossible to determine real-time, a more practical iterative approach has been adopted in determining the optimal filter weights $\underline{w}_o$. The easiest approach to implement is the steepest-descent algorithm given by

$$\underline{w}_k = \underline{w}_{k-1} - \frac{1}{2}\mu\frac{d\varepsilon}{d\underline{w}} \tag{5.11}$$

where the MSE is iteratively minimized by searching for the optimal filter weights in the direction of the gradient. In Equation 5.11 μ represents the iterative step-size. In general, large values of μ allow faster convergence upon $\underline{w}_o$ while sacrificing the margin of stability. It has been determined in general that a stable solution cannot occur if μ is greater than 2 or less than 0. Allowing the expected squared error to be approximated by the instantaneous squared error yields

$$\underline{w}_k = \underline{w}_{k-1} + \mu\,\underline{x}_k e_k \tag{5.12}$$

which is the gradient-estimated version of the steepest-descent algorithm. In order to implement the steepest-descent, LMS adaptive filtering technique only two elements of the system must be chosen: the step-size μ and the number of adaptive filter taps (the size of $\underline{w}$).

5.3.4 Sensor Array Spectral Analysis

The overall purpose of this spectral analysis was to determine which sensors and which frequency band best captured the flow quality improvements due to flow control. The wall-pressure spectra presented in this subsection were conditioned by the acoustic filtering technique described earlier. The background acoustic filtering was conducted with microphone pairs separated by 48°, as suggested in Section 5.3.3. After several iterations, the step-size and the number of FIR taps for the adaptive filters were chosen to be 0.01 and 28, respectively.

The frequency band from the wall-pressure sensors that measured the highest RMS pressure fluctuations at low frequencies was sought after because these turbulent structures were shown to be responsible for the mean flow total pressure losses (Chapter 3). A contour plot of the RMS pressures from the entire sensor array under the influence of a minimal control effort, u_{fwd} of 0.25% and u_{aft} of 0.75%, for a Mach 0.7 flow speed is shown in Figure 5.10. A quick glance at the contour plot in Figure 5.10 indicated which sensors recorded the highest, low-frequency turbulence levels. These results showed that over the entire array the highest RMS pressures were sensed between 200 and 400 Hz. As anticipated in Section 5.3.1, the sensors closest to the spoiled flow regions (0°, 12°, 24°, 120°, 132°, and 144°) recorded the largest RMS pressures, thereby indicating regions of severe total pressure loss. It should be noted that the microphone located at 36° was inoperable for all of the experiments presented in Chapter 5.

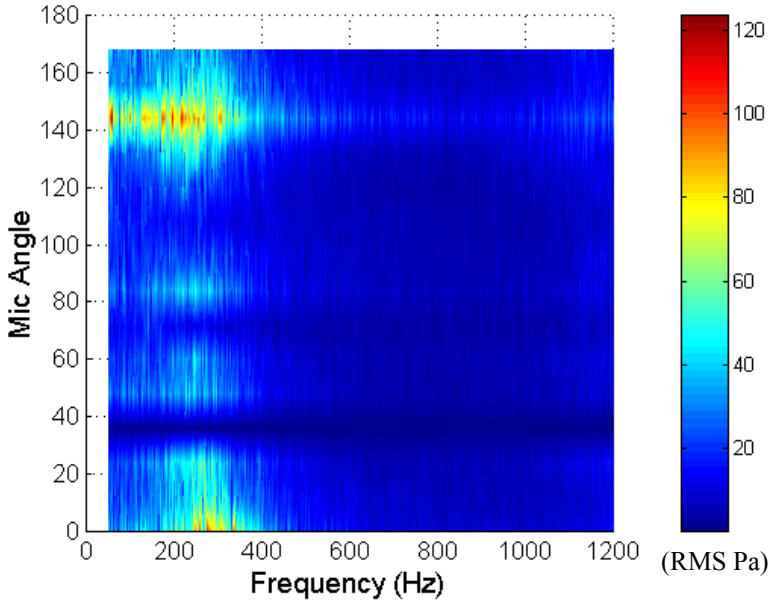

Figure 5.10: Array RMS Pressures for u_{fwd} of 0.25% and u_{aft} of 0.75% at Mach 0.7

The contour plot in Figure 5.11 presents the RMS pressures measured by the entire array between 50 and 1200 Hz under the optimal control efforts (u_{fwd} of 1.0% and u_{aft} of 0.75%) for a Mach 0.7 flow speed. A glance at the array RMS pressures for a Mach 0.7 flow under the optimal flow control settings (Figure 5.11) showed considerable reductions in the RMS pressure levels between 200 and 400 Hz, especially for those sensors located near the uncontrolled, spoiled flow regions.

Since it is difficult to deduce particular aspects of the spectral results from the contour plots of Figures 5.10 and 5.11, individual spectrums from the microphones located near the spoiled flow regions were analyzed in further detail. The RMS pressure spectra recorded at 0^o for the minimal and optimal control scenarios are shown in Figure 5.12. A more detailed view of the RMS pressure spectrums from the microphone at 0^o (Figure 5.12) shows that the optimal flow control input reduced the RMS pressure by a factor of approximately two in the 200-400 Hz

frequency band. This comparison (Figure 5.12) also further supported the fact that the 200-400 Hz frequency band was most sensitive to the flow control. Looking toward the higher frequencies in Figure 5.12, it was noticed that the flow control was ineffective in reducing the small-structured turbulence levels. This observation combined with the fact that the optimal control input greatly improved the total pressure recovery at 0^o provided further evidence that the low-frequency, large-scale turbulence is responsible for total pressure losses. A similar analysis was conducted for the other microphone located near spoiled airflow (located at 144^o). The RMS pressure spectrums from this microphone for the minimal and optimal control scenarios are plotted in Figure 5.13. Similar trends were noticed from the wall sensor located at the other region with spoiled airflow (144^o) in response to these same flow control efforts (Figure 5.13). However, a couple of subtle differences were noticed from this sensor in response to flow control. This sensor at 144^o, which responds solely to the upstream flow affecter, indicated better removal of small-scale turbulence at higher frequencies compared to the flow region near 0^o. At this time it could only be speculated that the flow control air mass remained very close to the wall at the 144^o location, which helped to reduce the small-scale turbulence level. Nonetheless, the fact remained that the 200-400 Hz frequency band still responded to the flow control with the greatest attenuation of turbulence levels. Now that the sensor locations and the frequency band that best distinguished the flow quality have been discovered, a detailed analysis of the RMS pressures integrated from 200 to 400 Hz was necessary in order to develop microphone signals capable of detecting the optimal control efforts.

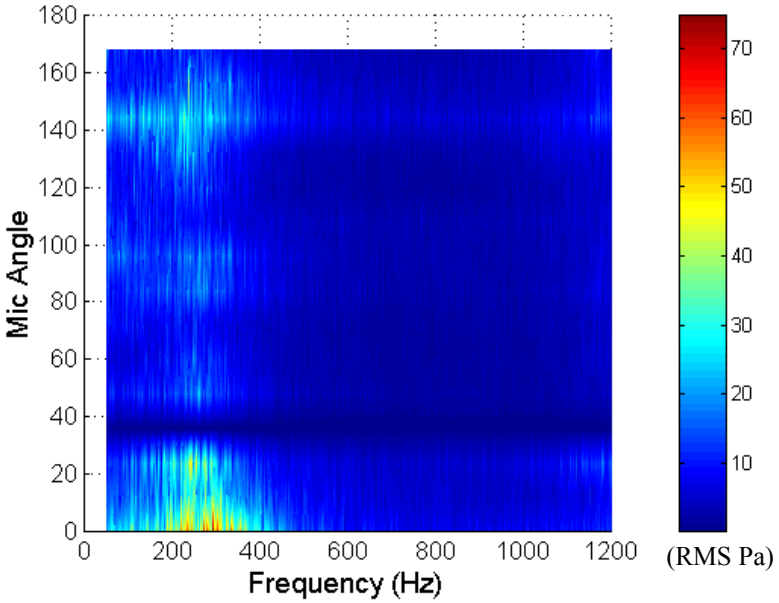

Figure 5.11: Array RMS Pressures for u_{fwd} of 1.0% and u_{aft} of 0.75% at Mach 0.7

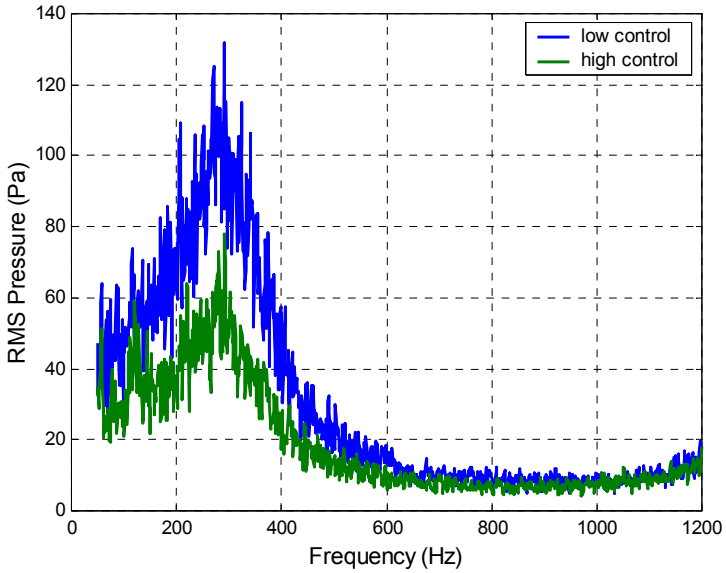

Figure 5.12: RMS Pressure Spectra at 0^{o} for high and low control efforts at Mach 0.7

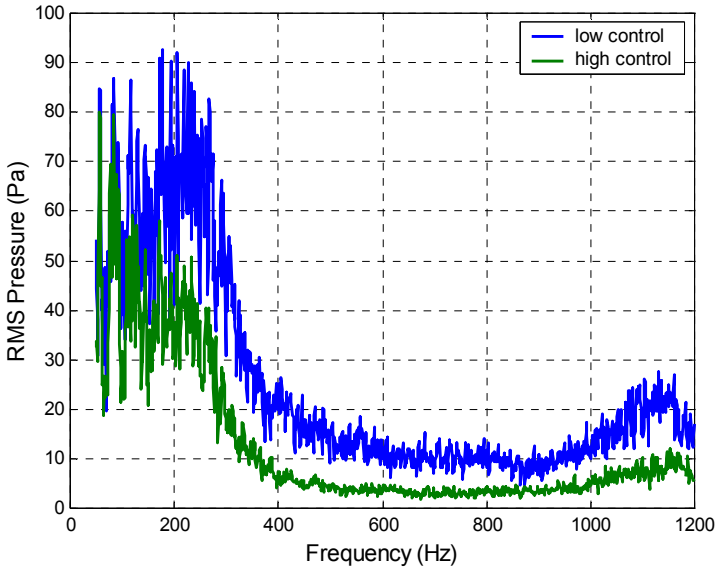

Figure 5.13: RMS Pressure Spectra at 144^{o} for high and low control efforts at Mach 0.7

5.4 RMS Wall-Pressure Responses to Flow Control

After inspection of the wall-pressure spectrums from the entire array in response to a variety of control efforts, the sensors near the spoiled flow regions were located. The original 16-microphone array was then condensed to a modest pair of 3-microphone arrays shown in Figure 5.14. Microphones 11, 12, and 13 of the original array, which were influenced by only the forward affecter, will now be referred to as Array 1. The remaining microphones 1, 2, and 3, which were influenced by both forward and aft affecters, will now be referred to as Array 2.

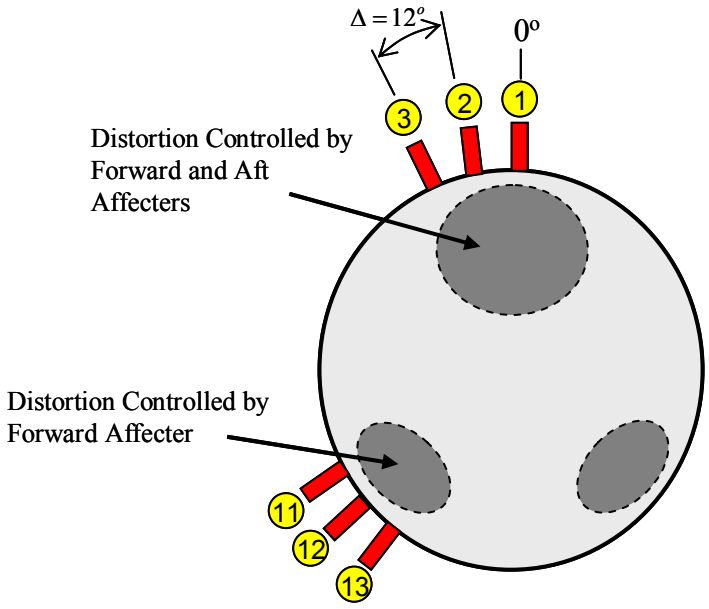

Figure 5.14: Reduced Set Microphone Arrays

Three microphones were used for each array in order to provide better coverage of the spoiled flow regions. The average of the three microphones from each array was used to provide a single signal flow quality descriptor for each spoiled flow region, and the averaged signal from Arrays 1 and 2 were denoted as H_1 and H_2 respectively.

These H-values are computed in a similar manner to the distortion observer H for the SISO distortion control system described in Chapters 3 and 4. Each of the six microphone signals was filtered by an 8^{th}-order digital band-pass Butterworth filter that passed only the signal content between 200 and 400 Hz. In order to provide the correct relative measurements of the microphones, each filtered microphone signal was then scaled by its particular sensitivity normalized by the average of the sensitivities from all six microphones used. The calibrated voltage signals from the microphones were then processed by adaptive filter networks pairing

each of the six microphone signals with another microphone signal located 48° away. These voltage signals now representing true turbulence levels were then processed through a running RMS algorithm that considered the 900 most recently sampled data points, which equated to a ½ second buffer with the 1800-Hz sampling rate used for this analysis.

The responses of H_1 and H_2 to the changes in forward and aft control efforts were examined to determine the coupling of the responses to both control inputs. As previously shown, the signal H_1 was expected to respond solely to the forward flow affecter, and the signal H_2 was expected to be coupled to both flow affecters. The plots of H_1 and H_2 versus each flow affecter control effort, which are shown in Figure 5.15 (a-b), provide an indication of the coupling between the H-values and the control inputs. These responses from H_1 and H_2 were measured under variations in the forward and aft affecter control efforts. Neither H_1, nor H_2 were measured in response to only one of the affecters due to facility operation cost. For example, several responses for H_1 would be recorded at a constant forward affecter control effort while the aft control effort was varied.

Focusing on the H_1 responses to the forward and aft affecters (Figures 5.15 (a) and (b)), it was quickly realized that H_1 responds almost exclusively to the forward affecter as expected. A curve-fit of the H_1 response to u_{fwd} with a 2nd-order polynomial (Figure 5.15 (a) in blue) showed a 96% agreement with this curve-fit, thus H_1 proved to be insensitive to variations in u_{aft}. The insensitivity of H_1 to u_{aft} is further supported by the 1% agreement in a 2nd-order polynomial curve-fit between H_1 and u_{aft} (Figure 5.15 (b) in blue). On the other hand, H_2 appeared to be primarily related to u_{aft} with its 87% agreement to a 2nd-order polynomial curve-fit between these

two parameters (Figure 5.15b in red). This correlation coefficient was considerably less than the 96% correlation between H_1 and u_{fwd}, because the forward affecter air mass diffused into the upper portion of the AIP near the sensors associated with H_2. This diffusion of the forward affecter air mass is seen by the 9% correlation of H_2 with u_{fwd}. This slight coupling of H_2 is not negligible, and it proposes that a true MIMO system exists. As the responses to flow control efforts are non-linear for both H_1 and H_2, the hopes of mathematically decoupling this system are dismal. This coupling will pose a problem for the feedback signal design based upon H_1 and H_2.

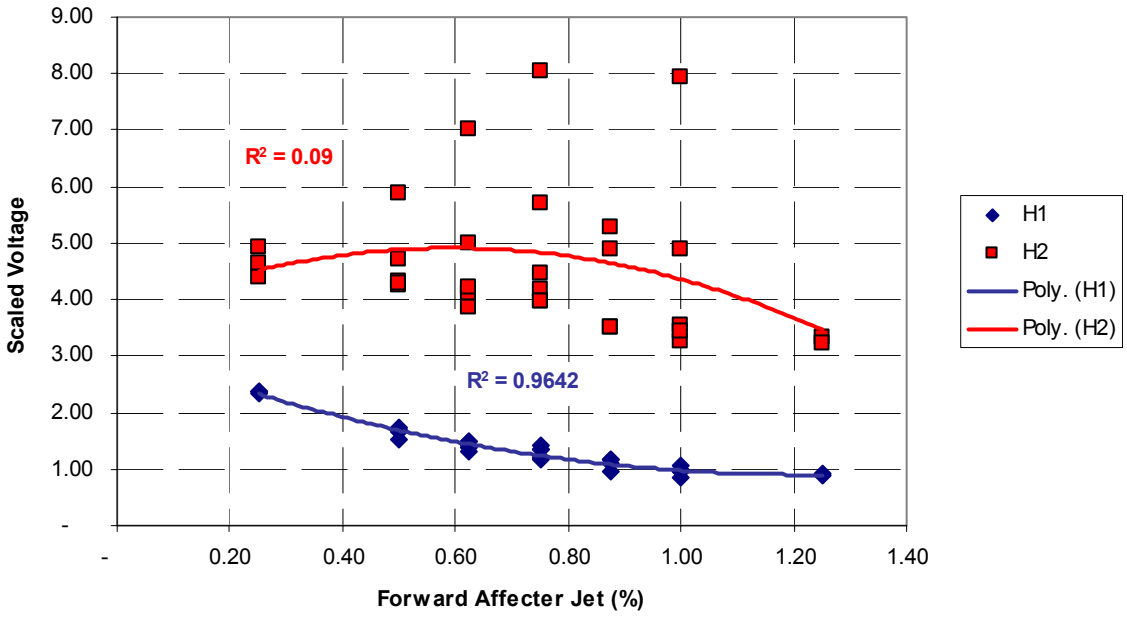

(a)

Figure 5.15 (a): H_1 and H_2 versus Forward Affecter Jet Mass Percentage

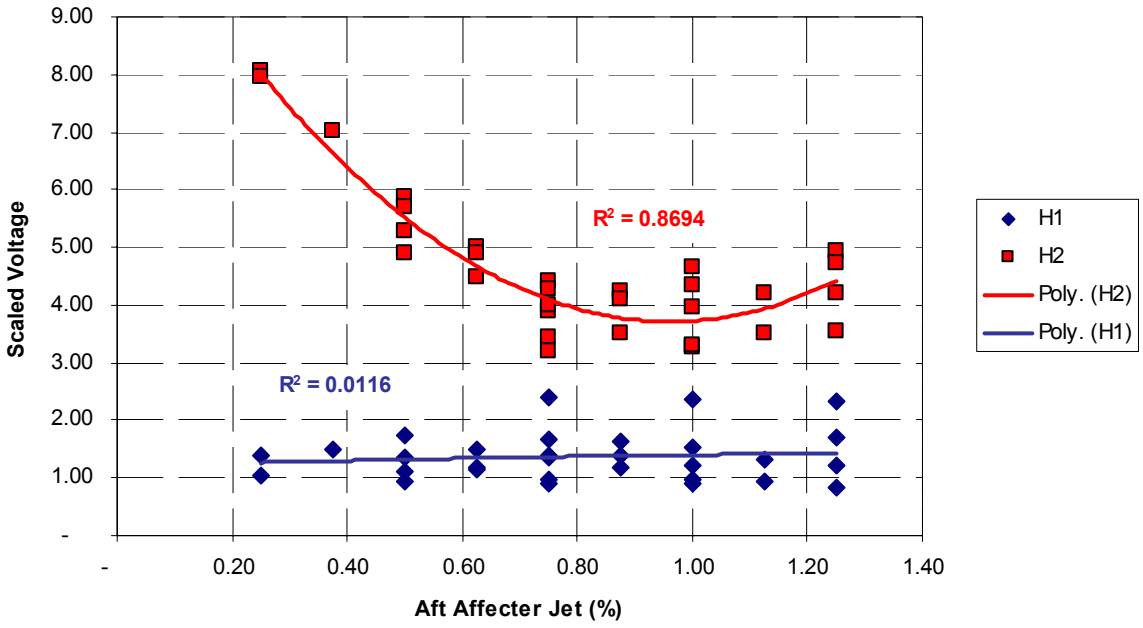

(b)

Figure 5.15 (b): H_1 and H_2 versus Aft Affecter Jet Mass Percentage

5.5 Wall-Pressure Based Optimal Control Indicator

The wall-pressure fluctuation signals H_1 and H_2 that monitor the flow control's removal of spoiled airflow needed to be manipulated in such a manner that they could be used to automatically direct the flow affecters to the desired control efforts. The required signal processing of H_1 and H_2 in order to achieve a suitable flow descriptor was desired to be simplistic, so that this technique could be easily implemented in a feedback control system in a

future experiment. As a result, the task focused on taking advantage of the decaying nature of the microphone responses to flow control, and then on properly handling the coupling of H_2 to both flow affecters.

In order to promote consistency, it was decided to create a microphone-based inlet performance indicator that incorporated the control effort, just as the cost function J (Eq. 5.2) provided the optimal tradeoff between the aerodynamic performance indices (*DPCP* and *PD*) and the control effort. By splitting the cost function J into two separate equations that are each associated with a flow affecter control input, and replacing the aerodynamic performance indices (*DPCP* and *PD*) with H_1 and H_2, the non-intrusive measure of the inlet performance was formulated as

$$\begin{aligned} y_1 &= q_H H_1 + q_u u_{fwd} \\ y_2 &= q_H H_2 + q_u u_{aft} \end{aligned} \tag{5.13}$$

The variables q_H and q_u are weighting coefficients that allow for prioritization of either the microphone signals or the control efforts. Since the performance and control weights Q_x and Q_u in the cost function J were both set to 0.5, q_H and q_u were also set to 0.5 for consistency. As was the case with the cost function J, the minimum values in y_1 and y_2 represented the optimal tradeoff between the inlet performance and the flow control effort.

In the application of this sensing technique (Eq. 5.13), the cross-coupling of the H_2 response to both the forward and aft affecters was first addressed. It was desired to avoid the complexities involved in mathematically decoupling the nonlinear responses of H_2 to the forward

and aft affecters. As a consequence it was decided to analyze y_1 first since H_1 was not cross-coupled to the aft affecter. Once the minimum value of y_1 was obtained, the forward control effort u_{fwd} would be held constant at that optimal setting. Without variation in u_{fwd}, the y_2 data set could then be analyzed solely for its response to the aft affecter control effort u_{aft}. Continuing with the emphasis on the Mach 0.7 flow speed scenario, the results of y_1 for Mach 0.7 are presented in Figure 5.16. The y_1 results highlighted in red correspond to the test conditions where u_{aft} was at its lowest level at each particular u_{fwd}. These responses in red represented the initial condition where the aft control had not yet been controlled according to y_2. Focusing on the initial condition responses of y_1, the minimum value corresponded to a forward control effort of 0.875%, which was extremely close to the 1.0% desired control effort according to *J*. As for the entire set of responses, the minimum value was also at 0.875% showing the minimal effect of the aft affecter control effort on y_1. The responses of y_2 to u_{aft} were then analyzed with u_{fwd} held constant at 0.875% and presented in Figure 5.17. The minimum y_2-value occurred at an aft control effort of 0.75%, which was identical to the optimal aft control setting according to *J*. The responses of y_1 and y_2 to their associated control inputs at Mach 0.5 and 0.6 are shown in Appendix D. The optimal control efforts predicted by y_1 and y_2 for Mach number flows 0.5, 0.6, and 0.7 are summarized in Table 5.5, and the percent difference between the optimal control efforts predicted by *J* and y_1 & y_2 are presented in Table 5.6.

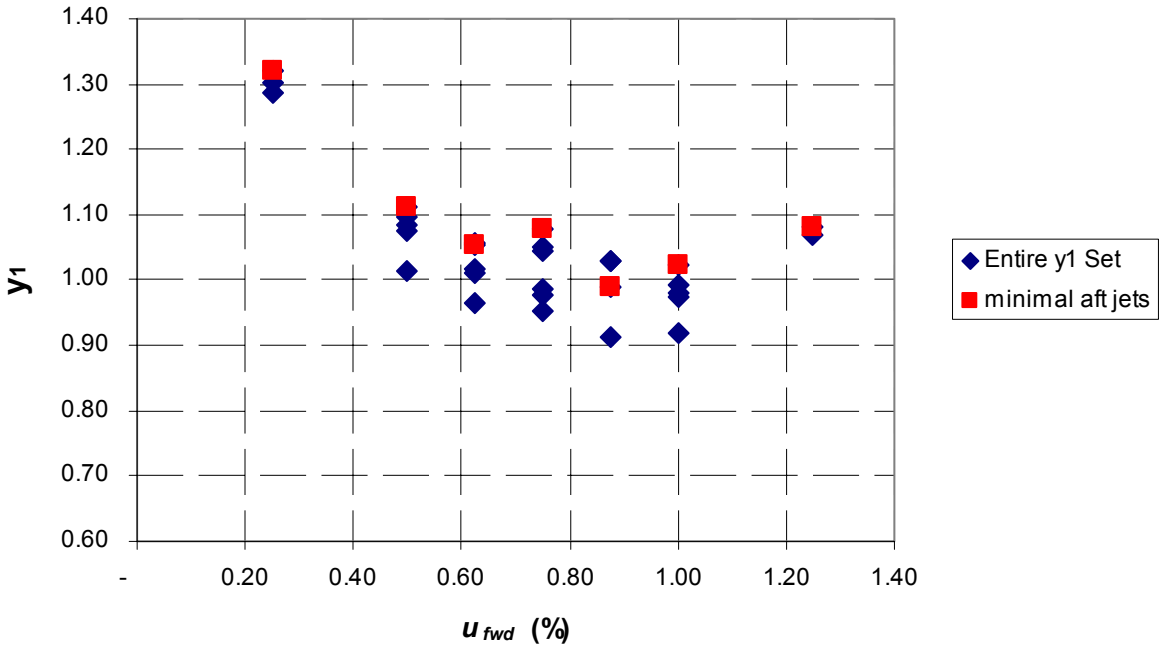

Figure 5.16: y_1 versus u_{fwd} for Mach 0.7

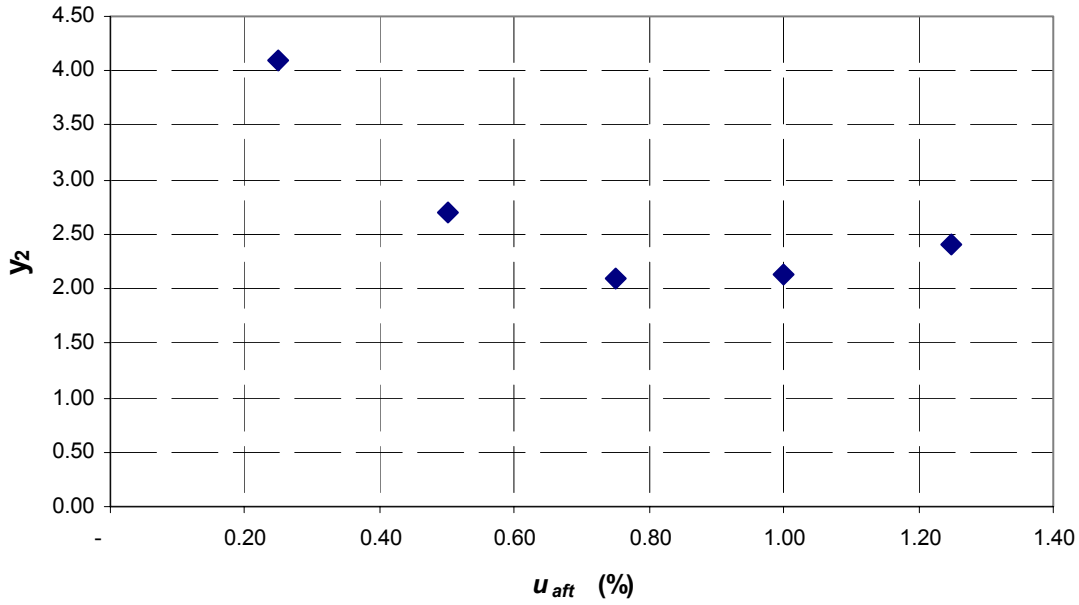

Figure 5.17: y_2 versus u_{aft} with $u_{fwd} = 0.875\%$, for Mach 0.7

Table 5.5: Comparison of Optimal Control Settings from J and y_1 & y_2

Mach	Predicted by J		Predicted by $y1$ and $y2$	
	u_{fwd}	u_{aft}	u_{fwd}	u_{aft}
0.5	0.5	0.75	0.5	0.75
0.6	0.5	0.75	0.625	0.75
0.7	1.0	0.75	0.875	0.75

Table 5.6: Percent Difference Between Optimal Control Settings from J and y_1 & y_2

Mach	u_{fwd}	u_{aft}
0.5	0	0
0.6	20	0
0.7	12.5	0

In conclusion this non-intrusive inlet performance estimation technique, based on wall-pressure fluctuation measurements, indicated optimal flow control efforts that agreed well with optimal control efforts determined from a cost function based on the circumferential total pressure distortion intensity *DPCP* and the average pressure recovery *PR* (Tables 5.5 and 5.6). This inlet performance estimator was able to determine the optimal control efforts for a serpentine inlet equipped with two flow affecters, as opposed to the single affecter system described in Chapters 3 and 4. Finally, this inlet performance sensing technique was not a function of Mach number, which was the primary drawback of the distortion observer H described in Chapters 3 and 4.

5.6 Architecture of a Potential Distortion Control System with Two Flow Affecters

The scope of this research was directed at providing a non-intrusive sensing technique to infer the optimal control efforts from two flow affecters intended to minimize the average total pressure losses *PD* and the circumferential total pressure distortion intensity *DPCP* delivered to a jet engine compressor coupled to a serpentine inlet. A non-intrusive observation technique that identified the appropriate control efforts from forward and aft flow affecter locations was presented in the previous subsection. An experimental demonstration of a closed-loop system incorporating this observation technique was beyond the resources of this research, but this subsection proposes the architecture of a potential inlet performance control system.

Using the signals y_1 and y_2 (Eq. 5.13) directly for feedback in a control system would create a multiple-input, multiple-output (MIMO) control scenario. This system would be half-coupled due to the dependence of y_2 on both flow affecter inputs. In order to avoid the coupling effects in a true MIMO control system, a scheduled control algorithm could be used to decouple the feedback signals. As a result, the MIMO system would be converted into two independent single-input, single-output (SISO) control systems. The controller associated with the feedback of y_1, which is the independent signal, would be scheduled first to achieve the optimal level of y_1 using the forward affecter. Since this control loop takes precedence over the y_2 feedback loop, it will be referred to as the master. Once the master loop has been appropriately controlled, the

controller associated with y_2, denoted as the slave, could then be activated. A schematic of this proposed control system is shown in Figure 5.18.

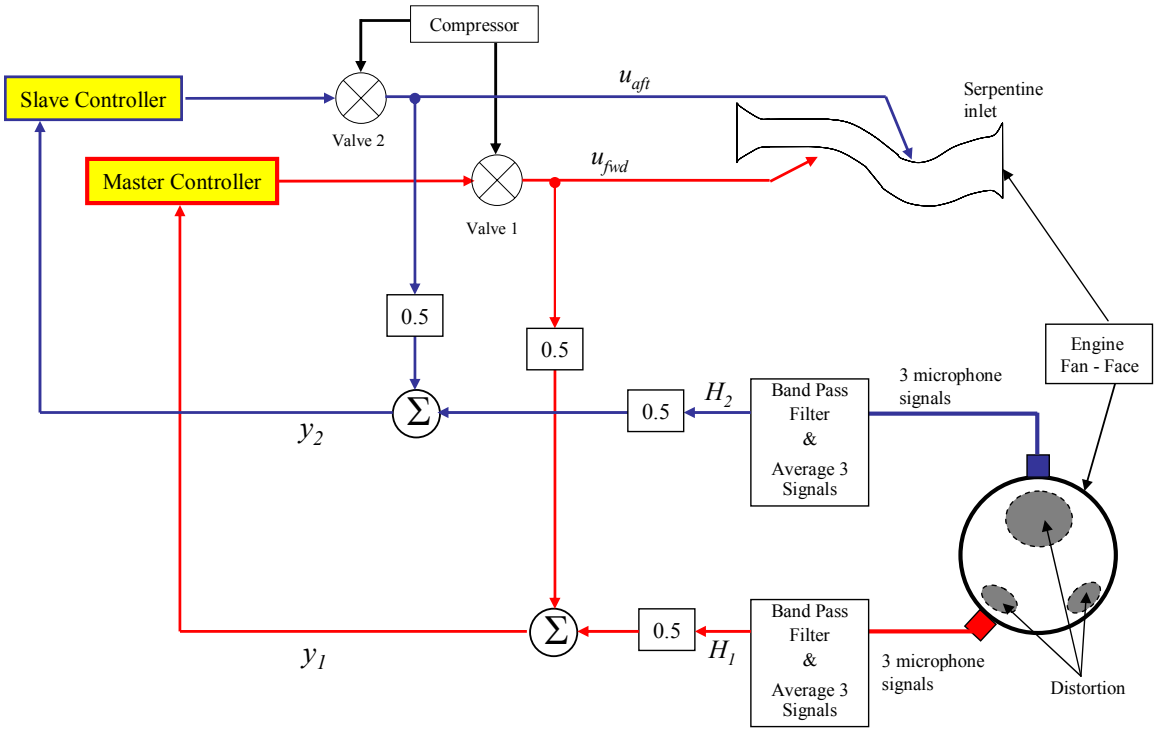

Figure 5.18: Schematic of Proposed Closed-Loop Inlet Performance Control System

The control logic for both the master and slave controllers would be gradient searching algorithms that locate the minimum values of y_1 and y_2. It is proposed that a simple constant step searching algorithm such as

$$U_{i+1} = U_i + D_i S$$

where;
$U_i \equiv$ control effort (Volts to control valve)
$D_i \equiv$ control decision
$S \equiv$ constant step size (Volts)

(5.14)

be used to locate the minima of y_1 and y_2. The control decision D would be based on the gradient of the feedback signal y with respect to the control effort u denoted as b in

$$D_i = \begin{cases} 1, \; if \; b \le b_{cr} \\ -1, \; if \; b > b_{cr} \end{cases} \qquad \text{where} \quad b_{cr} \equiv \text{ critical slope value} = 0 \; . \tag{5.15}$$

In order to correctly schedule the activation of the slave controller, a flag to activate the slave controller would need to be turned on in the master control algorithm once the minimum y_1 value was obtained. For example this flag could be turned on when the master control decision D_1 was set to -1. Combining this control system architecture with the non-intrusive sensing technique described in Section 5.5 should produce a control system capable of achieving control efforts proven to be optimal by the inlet performance cost function J (Eq. 5.2).

5.7 Summary

This chapter was concerned with furthering wall-pressure sensing techniques to infer optimal inlet performance. A serpentine inlet at a Lockheed Martin facility was used for this sensory development, which had a lower length-to-diameter ratio than the test inlet used for the

experiments presented in Chapters 3 and 4. This test facility provided the advantage of reaching Mach 0.7 at the inlet's throat, compared to the maximum Mach of 0.55 at the Virginia Tech facility. Also, this new inlet was equipped with a second array of jet-type flow affecters positioned upstream of the original flow affecter to reduce the secondary flow causing total pressure losses in the lower half of the AIP cross-section. Optimal control efforts for the forward and aft affecter were determined based on AIP total pressure measurements for flow speeds of Mach 0.5, 0.6, and 0.7. A pair of microphone-based signals were developed that could properly indicate which control efforts were optimal. This sensing technique was independent of Mach number, which was a dependency that hindered the distortion observer H developed in Chapter 3. Finally, the architecture of a proposed control system was described for the future implementation of this newly developed non-intrusive, optimal inlet performance sensing technique.

Chapter 6

Conclusions and Future Work

This chapter provides a summary of the key results and contributions from the research presented in this dissertation. Section 6.1 discusses the conclusions from the non-intrusive distortion sensing techniques and the first successful demonstration of an automated distortion control system. Then in Section 6.2, future directions for this research topic are suggested.

6.1 Conclusions

This research has produced three significant contributions to the aero propulsion community: a non-intrusive means of sensing distortion in serpentine inlets, an automated distortion control system demonstration, and a non-intrusive means of sensing optimal control efforts with regards to overall inlet aerodynamic performance. To the author's knowledge, a distortion control system using non-intrusive feedback sensors has never before been demonstrated. As a result of the non-intrusive sensing and control developments in this research, implementation of the jet-type VG flow affecters into aircraft equipped with serpentine inlets appears to be extremely feasible.

The non-intrusive sensing technique that infers *DPCP* was based on the basic knowledge of secondary flow development and TBL separation phenomenon that occur in serpentine inlets. The nature of the turbulence associated with these parasitic flow qualities was focused on to provide indications of the flow distortion. Large-scale, low-frequency, energetic turbulent fluctuations were observed by wall-pressure sensors to be highly indicative of the total pressure losses in the vicinity of the measurement. This finding was in accordance with the fact that large-scale turbulence dictates the rate of turbulent kinetic energy dissipation, which is typically in equilibrium with the extraction of mean flow total pressure by the turbulent flow. Strategic wall-pressure sensor placement was afforded by the knowledge of these aforementioned flow characteristics, which yielded a simplistic distortion sensing technique that could be easily implemented real-time in a distortion control system. This wall-pressure-based distortion observer was validated by its high level of correlation with the *DPCP* metric at Mach numbers of

0.4, 0.5, and 0.55. However, the linear relationships between the distortion observer and *DPCP* were a function of the Mach number, which would require Mach number feedback to implement this observer technique in a distortion control system. As a final measure, the wall-pressure-based distortion observer was shown to be insensitive to the background facility-related acoustic disturbances. Despite this finding it is recommended that the background acoustic disturbance filtering technique proposed by Naguib et al. [23] be incorporated into the distortion observer computation for future implementation in order to reject possible higher-order acoustic modes that will unevenly bias the wall-sensor measurements.

The most significant outcome of this research was the successful demonstration of the automatic distortion control system. The distortion observer provided the distortion feedback information to a PID controller that adjusted the VG flow affecter blowing rates in order to obtain the desired *DPCP* levels in the serpentine inlet. This control system demonstrated a high speed of response to immediate requests for reduction in *DPCP* levels. A 66% reduction in *DPCP* was achieved in less than 1 second and maintained indefinitely. This control system also demonstrated a high level of distortion control during the event of a simulated aircraft deceleration and acceleration, which provided indication of this system's capability to properly function under the influence of realistic flight dynamics.

The final aspects of this research provided a technique for detecting the optimal flow control efforts from two flow affecters in serpentine inlets. The *PR* and *DPCP* metrics and the air bleed rates from the compressor required to provide the flow control were considered for the optimal performance analysis. Lockheed Martin provided the optimal control efforts for each

Mach number tested. A cost function was constructed to have the capability of identifying the same optimal control efforts as Lockheed Martin. The cost function was developed to provide a model for a similar cost function that replaced the *PR* and *DPCP* metrics with wall-pressure fluctuation measurements. This cost function, which considered the wall-pressure measurements, predicted optimal control efforts that were in excellent agreement with the baseline cost function. This new non-intrusive sensing approach provided several key advantages over the previously developed distortion observer: indication of optimal overall compression system performance independent of Mach number. Finally, the control system architecture and control logic necessary to implement this optimal sensing technique were presented.

6.2 Future Work

In the immediate future the optimal sensing technique described in Chapter 5 should be incorporated into the proposed automatic control system and experimentally demonstrated. There are several control system design challenges that exist before demonstrating such a system. Of paramount concern is the coupling of the signal H_2 to both flow affecter control efforts. A concerted effort should be made to investigate non-linear decoupling techniques since operating two independent SISO controllers would greatly reduce the system complexity. Attention to designing the adaptive filters such that their settling time is an order of magnitude faster than the remaining system dynamics should be made. Slow adaptive response will produce erroneous feedback values during system dynamic events.

Recall that the sensing and control research presented in this dissertation pertained to the level, symmetric flight condition. In order for this sensing approach to be truly feasible, it must be capable of detecting an asymmetric distortion pattern, which is shown in Figure 6.1. This would require measuring the wall-pressure fluctuations on both sides of the inlet exit plane. In addition, the sensing algorithms would need to be adjusted to handle measurements from both sides of the inlet exit plane. The concept of using two independent jet-type VG's to independently control the vertical halves of the AIP is shown in Figure 6.2. Additional flow control experiments will need to be conducted to test the effectiveness of independent VG arrays to control one half of the flow field (Figure 6.2). The regions of controllability for each VG array would need to be investigated for any coupling

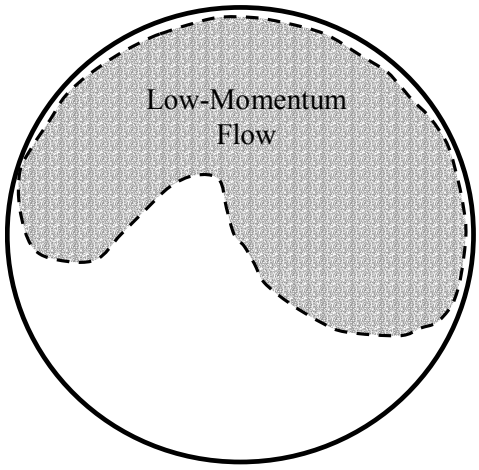

Figure 6.1: Asymmetric Distortion Pattern Created by Sideslip

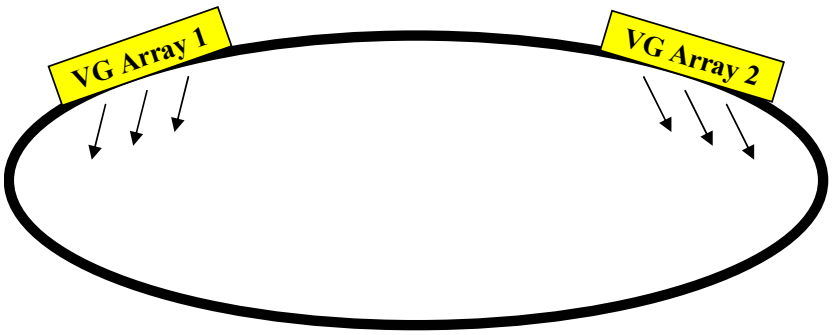

Figure 6.2: Independent VG Arrays each Controlling Half of Flow Field Located at an Upstream Station in the Inlet

effects. If each VG array produced independent affects on the flow, it would be logical to speculate that the VG array on the side with higher extents of distortion would output a higher control effort. For the distorted flow pattern presented in Figure 6.1, the VG array 2 of Figure 6.2 would need to output a higher control effort. The recommended sensing approach would stem from the optimal sensing technique presented in Chapter 5.

The long range future work necessary for implementing this technique into an actual aircraft lies in the area of more realistic test conditions. This sensing and control technique should be tested in a wind tunnel facility capable of simulating sideslip and angle of attack for the aircraft. In addition, the distortion effects created by an aircraft forebody should also be investigated.

References

[1] Hamed, A. and Numbers, Keith. "Inlet Distortion Considerations for High Cycle Fatigue in Gas Turbine Engine." AIAA 1997.

[2] Fulghum, D.A.. "Stealth Engine Advances Revealed in JSF Designs." Aviation Week & Space Technology. March 19, 2001, pp. 90-99.

[3] Gridley, M.C., and Walker, S.H.. "Inlet and Nozzle Technology for 21st Century Fighter Aircraft", ASME 96-GT-244, International Gas Turbine and Aeroengine Congress, Birmingham, UK, June 1996.

[4] Wendt, B. Serpentine Inlet Total Pressure Measurements. NASA Glenn Research Center, Cleveland, OH, 2000.

[5] Air Force Office of Scientific Research. Basic Research Issues in Aerodynamics and Control of HCF. Workshop Held at Gas Turbine Laboratory, MIT, 1995.

[6] Dixon, S.L. "Fluid Mechanics and Thermodynamics of Turbomachinery". 4th-edition, Butterworth Heinemann, 1998.

[7] Smith, W. "Pressure Losses in Ducted Flows". The Butterworth Group, London, UK. 1971.

[8] Anderson, B.H., and Gibb, J. "Study on Vortex Generator Flow Control for the Management of Inlet Distortion". *Journal of Propulsion and Power, Vol 9, No. 3,* pp. 420-430, 1993.

[9] Hamstra, J.W., Miller, D.N., Truax, P.P., Anderson, B.A., and Wendt, B.J. "Active Inlet Flow Control Technology Demonstration". ICA-6112. 22nd International Council of the Aeronautical Sciences, August 27 – September 1, 2000, Harrogate, UK.

[10] Rabe, A. Serpentine Inlet Total Pressure Measurements. Virginia Tech and Technology in Blacksburg, Blacksburg, VA, 2001.

[11] Harper, D.K. "Boundary Layer Control and Wall Pressure Fluctuations in a Serpentine Inlet". Masters of Science Thesis, Mechanical Engineering Dept. Virginia Tech, May 2000.

[12] Simpson, R.L. "Aspects of Turbulent Boundary-Layer Separation". 0376-0421(95)00012-7. Prog. Aerospace Sci., Vol 32, pp. 457-521, 1996.

[13] Vanyo, J.P. "Rotating Fluids in Engineering and Science". Butterworth Heinemann, 1993.

[14] SAE Aerospace Recommended Practice 1420 Revision A. "Gas Turbine Engine Inlet Flow Distortion Guidelines", 1998.

[15] Installation Manual for the TFE109-1 Turbofan Jet Engine. Allied-Signal Aerospace Co., Garrett Engine Division. December 18, 1992.

[16] Kinsler, L.E., Frey, A.R., Coppens, A.B., and Saunders, J.B. "Fundamentals of Acoustic" 4th Edition, John Wiley & Son, 2000.

[17] TMS320C30 Manual. Texas Instruments, 1990.

[18] Holmes, P., Lumley, J. L., and Berkooz, G. "Turbulence, Coherent Structures, Dynamical Systems, and Symmetry". Cambridge Monographs on Mechanics, 1996.

[19] Bull, M. K. "Wall-Pressure Fluctuations Beneath Turbulent Boundary Layers: Some Reflections on Forty Years of Research". Journal of Sound and Vibrations, 190, 1996, pp. 299-315.

[20] Wark, C. E., Naguib, A. M., "On the Relationship Between Wall Pressure and Velocity Field in a Turbulent Boundary Layer". AIAA 98-2642.

[21] Moss and Oldfield. "Effect of Free-Stream Turbulence on Flat-Plate Heat Flux Signals: Spectra and Eddy Transport Velocities". *Journal of Turbomachinery.* Vol. 118, July 1996, pp. 461-467.

[22] Walpole, Myers, and Myers. "Statistics for Engineers and Scientist" 6th Edition, Prentice Hall, 1998.

[23] Naguib, A.M., Gravante, S.P., and Wark, C.E. "Extraction of Turbulent Wall-Pressure Time Series Using an Optimal Filtering Scheme". *Experiments in Fluids*, 22, pp. 14-22.

[24] Farabee, T.M. "Flow-Induced Noise Due to Laminar-Turbulence Transition Process". Presented at the ASME Winter Annual Meeting, San Francisco, CA, December 10-15, 1989.

[25] Wambsganss, M.W. and Zaleski, P.L. "Measurements, Interpretation, and Characterization of Near-Field Flow Noise. ANL-7685, 1970, 112-140.

[26] Simpson, R.L., Ghodbane, M., and McGrath, B.E. "Surface Pressure Fluctuations in a Separating Turbulent Boundary Layer". Journal of Fluid Mechanics, 1987, Vol. 177, pp. 167-186.

[27] Lighthill, M.J. "On Sound Generated Aerodynamically: I. General Theory". Reprinted from the Proceedings of the Royal Society, Series A, Vol. 211, 1952, pp. 564-587.

[28] Lighthill, M.J. "On Sound Generated Aerodynamically: II. Turbulence as a Source of Sound". Reprinted from the Proceedings of the Royal Society, Series A, Vol. 211, 1952.

[29] Morse, P.M., and Ingard, K.U. "Theoretical Acoustics". McGraw-Hill, Inc. New York, NY, 1968.

[30] Hambley, A. R. "Electrical Engineering Principles and Applications". Prentice Hall, 1997.

[31] Allan, B.G., Juang, J.N., Raney, D.L., Seifert, A., Pack, L.G., and Brown, D.E. "Closed-loop Separation Control Using Oscillatory Flow Excitation". NASA/CR-2000-210324.

[32] Franklin, G.F., Powell, J.D., and Workman, M. "Digital Control of Dynamic Systems". 3rd-Edition, Addison Wesley, 1998.

[33] Dorf, R.C. and Bishop, R.H. "Modern Control Systems". 8th Edition, Addison Wesley, 1998.

[34] Phil Truax. Aerospace Engineer at Lockheed Martin Aeronautics, Co. November 2002.

[35] Conversations regarding secondary flows with Dr. Semih Olcmen. November 2001.

[37] Solo, V. and Kong, X. "Adaptive Signal Processing Algorithms: Stability and Performance". Prentice Hall, 1995.

[38] Chassaing, R. "Digital Signal Processing with C and the TMS320C30". John Wiley & Sons, 1992.

[39] Harris, F.J. "On the Use of Windows for Harmonic Analysis with the Discrete Fourier Transform". Proceedings of the IEEE, Vol. 66, No. 1, January 1978.

[40] Goodwin, G.C., Graebe, S.F., and Salgado, M.E. "Control System Design". Prentice Hall, 2001.

Appendix A Secondary Flow Analysis

Simple analysis of the airflow within serpentine inlets describes the basic mechanisms that create the secondary flow patterns that contribute to flow distortion entering the jet engine compressor. Qualitative analysis of the turning flows in the serpentine inlet using the inviscid Euler's equation can be used to construct a map of the secondary flow field throughout the inlet. There are three bends in the inlet (Fig. A.1) that create secondary flow patterns, and the contribution from each bend can be superimposed to form the secondary flow map at the exit plane of the inlet.

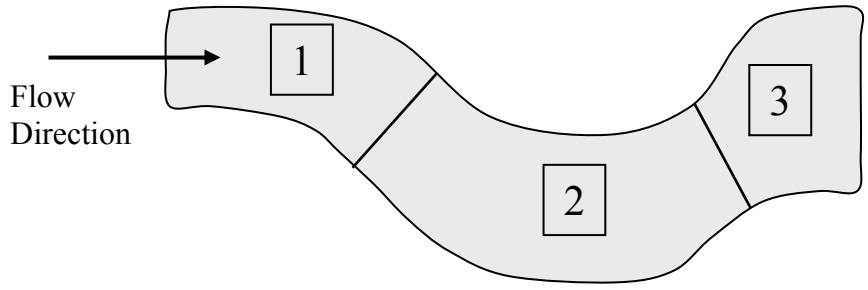

Figure A.1: Bends in Serpentine Inlet Creating Secondary Flow

This analysis takes advantage of the symmetric flow field that results from a level, symmetric flight condition by analyzing the flow on only one side of the inlet. Looking first at the half-section of the inlet at bend 1 (Fig A.2), the Euler's analysis can reveal the fundamental dynamics that cause secondary flow development. As the shape of the duct cross-section does not affect the outcome of this analysis, a simple rectangular cross-section was chosen to illustrate

this secondary flow development. Of course viscosity will create boundary layers along all of the inner surfaces of the duct, but it can be shown that only the boundary layer along the back wall contributes to the creation of a secondary flow. Due to the viscosity at the back wall, a boundary layer velocity profile will be present where the velocity at the wall must obey a no-slip

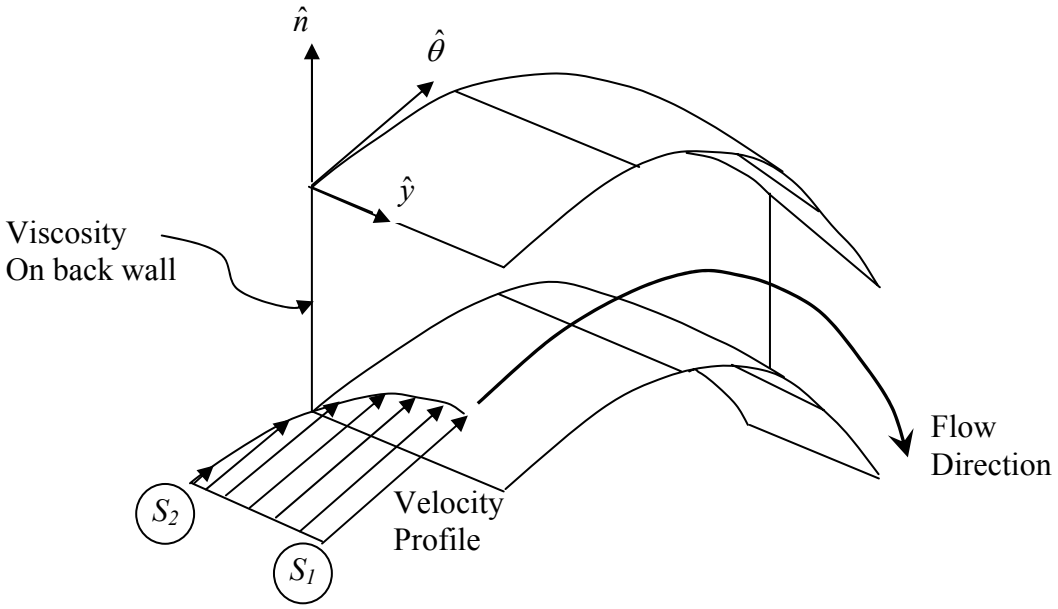

Figure A.2: Half-Section View of Bend 1

condition. The downstream progression of this low momentum flow near the wall will be tracked along streamline S_2. Moving outward from the wall in the y-direction, the stream-wise velocities will approach the free-stream velocity. The progression of the free-stream will be simultaneously tracked along streamline S_1.

Due to the curved flow path (Fig. A.3), the fluid particles undergo tangential accelerations. The normal component of Euler's inviscid equation of motion

$$\frac{\partial p}{\partial n} = \rho\left(\frac{v^2}{R}\right) \tag{1.1}$$

can be applied along both streamlines. A fair assumption can then be made that the pressure gradient in the normal direction will be the same for both streamlines S_1 and S_2. In addition, the flow will be assumed incompressible which states that the density will be the same for both streamlines.

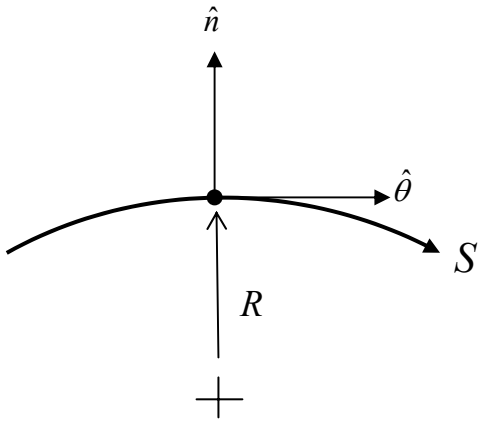

Figure A.3: Curved Flow Path Showing Radius of Curvature

Application of these two assumptions and some algebraic manipulation allows an expression to be written relating the radius of curvature to the particle velocity for each streamline (Eq. 1.2), which can then be used to qualitatively compare the paths of each streamline.

$$R = \frac{\rho V^2}{\partial p / \partial n} \qquad \text{(1.2)}$$

$$\text{then,} \quad R \propto V^2$$

Use of Equation 1.2 allows for the following qualitative analysis (Eq. 1.3) to reveal that the higher momentum flow along S_1 will flow through a larger radius of curvature.

$$V_1^2 > V_2^2 \quad \therefore \quad R_1 > R_2 \qquad \text{(1.3)}$$

As the high momentum fluid moves outward through the bend, the low momentum fluid is simultaneously moving toward the inside of the bend (Fig. A.4). These streamlines re-circulate upon reaching the bottom and top inner surfaces of the duct which creates a large counter clockwise circulating or secondary flow pattern as seen looking downstream toward the exit plane of the duct (Fig. A.5).

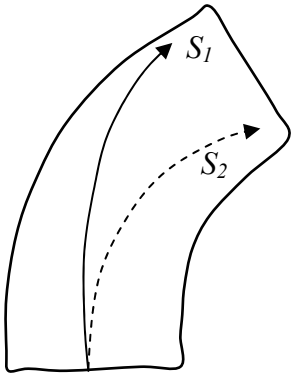

Figure A.4: Paths of Streamlines S_1 and S_2 (View from +y-direction)

Similar analysis at bends 2 and 3 will determine the contribution of each bend to the overall secondary flow field at the inlet exit plane. The superposition of the secondary flow created in each of the three bends creates the overall secondary flow field pictured in Figure A.6. Recalling that the low-momentum, turbulent boundary layer flow moves toward the inside of each bend, this low-momentum, spoiled airflow accumulates at the top-center and the two bottom right and left sectors which is also shown in Figure A.6.

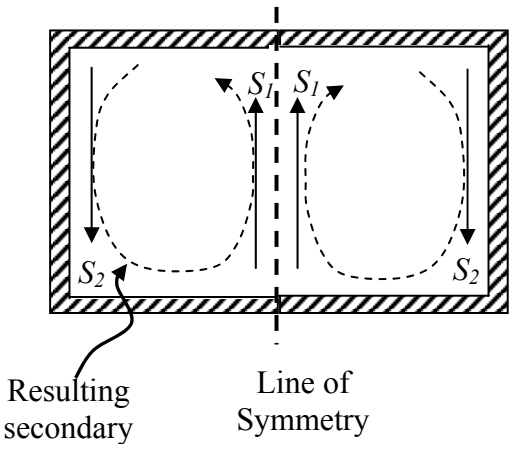

Figure A.5: Secondary Flow Patterns

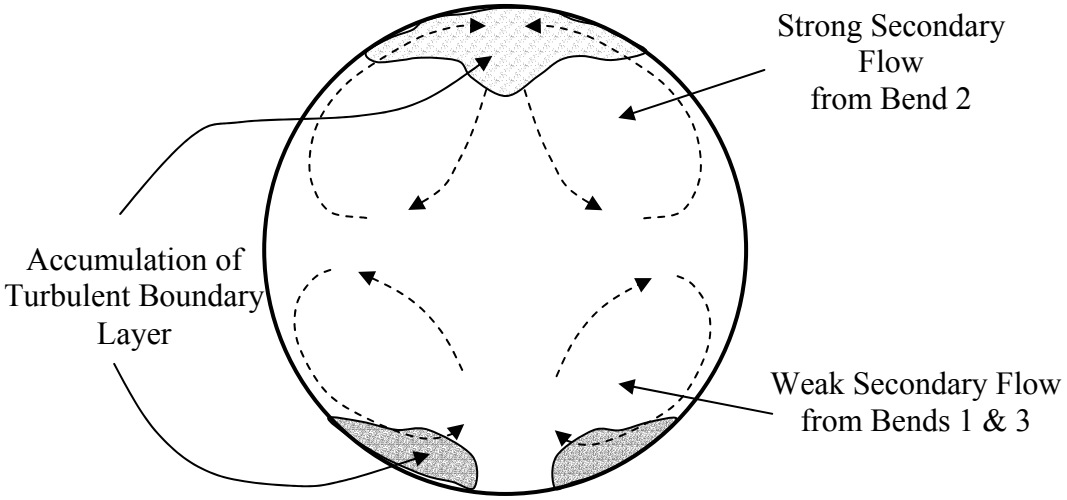

Figure A.6: Secondary Flow Field at the Inlet Exit Plane

Appendix B: Microphone Array Spectral Results in Response to Flow Control

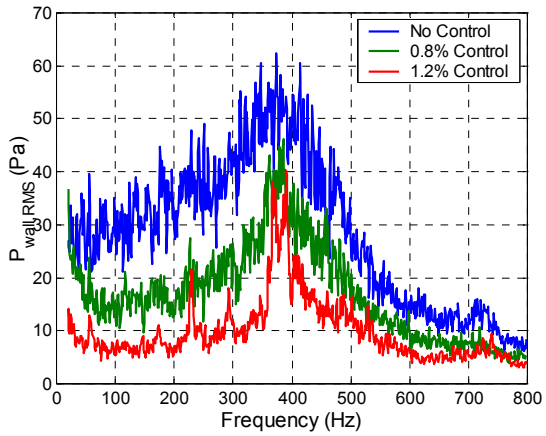

(a) 0°

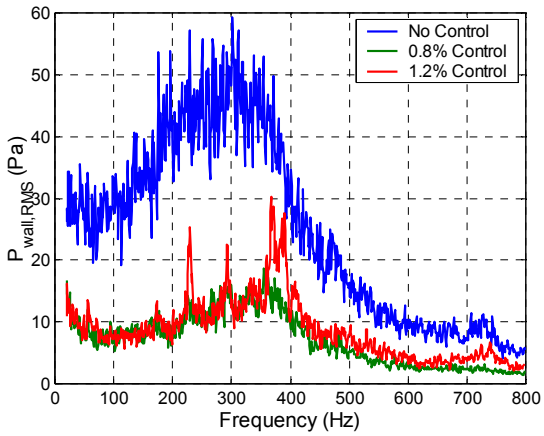

(b) 9°

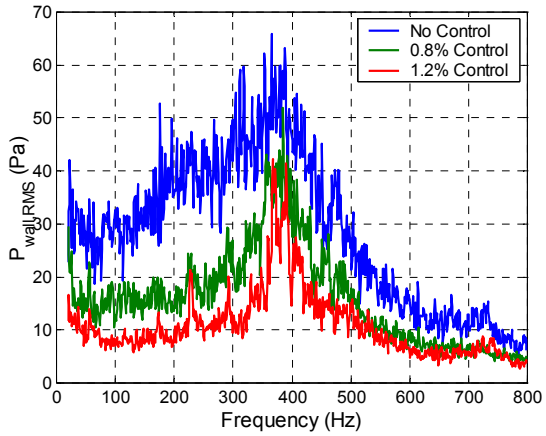

(c) 15°

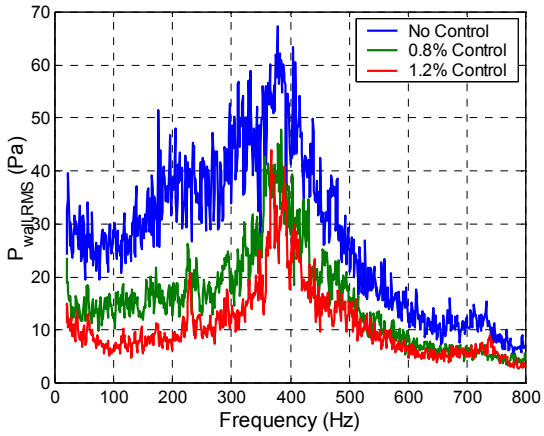

(d) 21°

Figure B.1: RMS Pressure Spectra for 12-microphone Array Varied Control Efforts at Mach 0.55

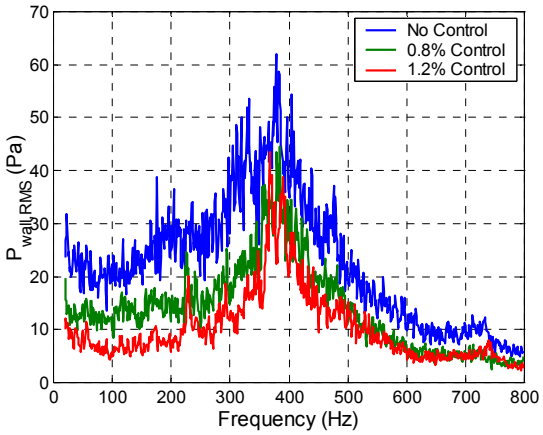

(e) 27°

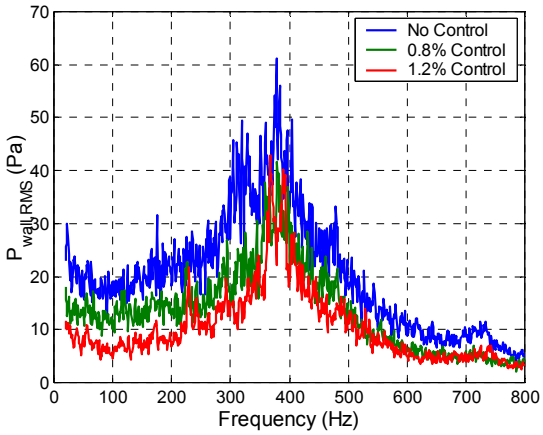

(f) 33°

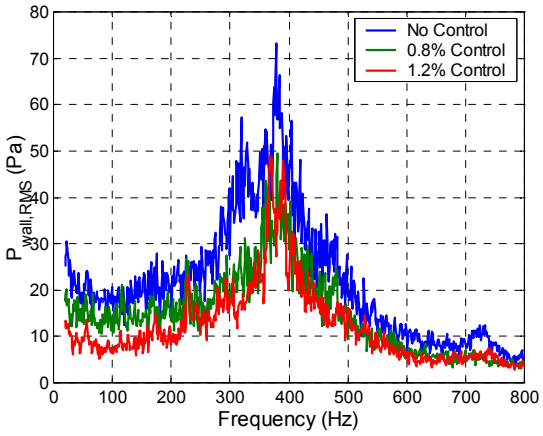

(g) 39°

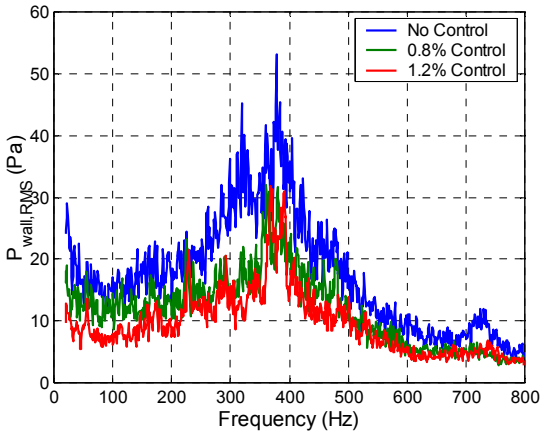

(h) 45°

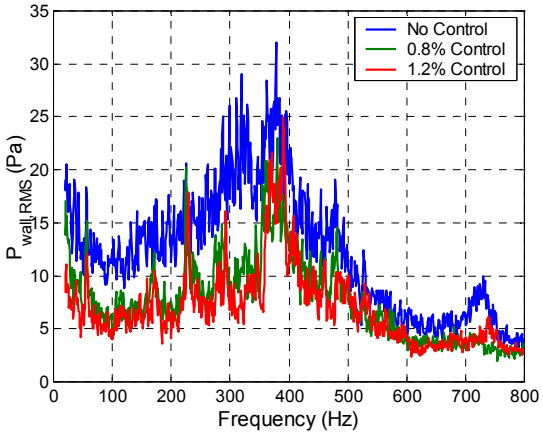

(i) 54°

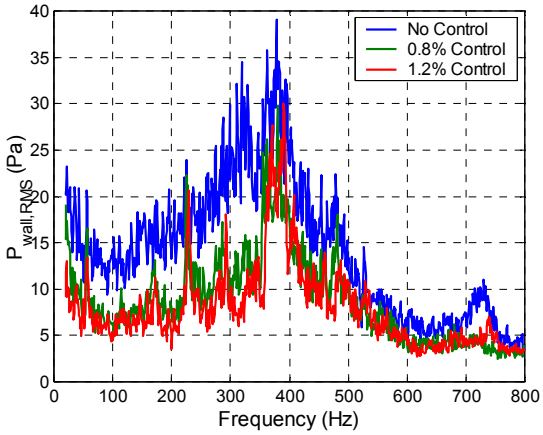

(j) 57°

Figure B.1: RMS Pressure Spectra for 12-microphone Array Varied Control Efforts at Mach 0.55

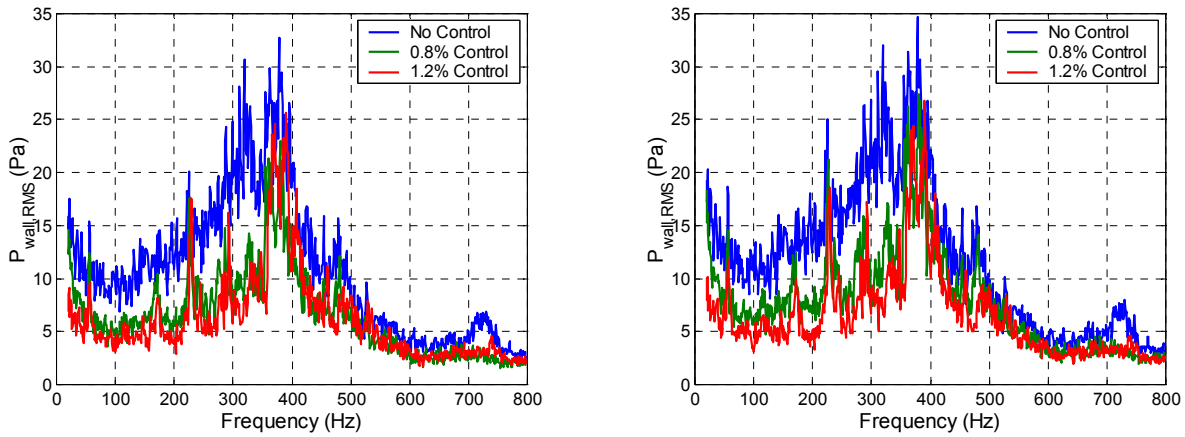

(k) 63° **(l)** 69°

Figure B.1: RMS Pressure Spectra for 12-microphone Array Varied Control Efforts at Mach 0.55

The stationarity of the wall-pressure spectra was then analyzed to quantify the repeatability of these wall-pressure measurements. This analysis considered wall-pressure signal time histories of 60 seconds sampled at 2400 Hz for control efforts of 0% and 1.0%. Sixty Fourier transforms were computed from the 60-second time histories, which provided a frequency resolution of 1 Hz. The average and the standard deviation of the 60 RMS wall-pressure spectra for each flow condition from each microphone were computed. From these two statistical parameters, the coefficients of variation were computed. Low coefficients of variation were desired, because that would indicate that the wall-pressure signals were repeatable.

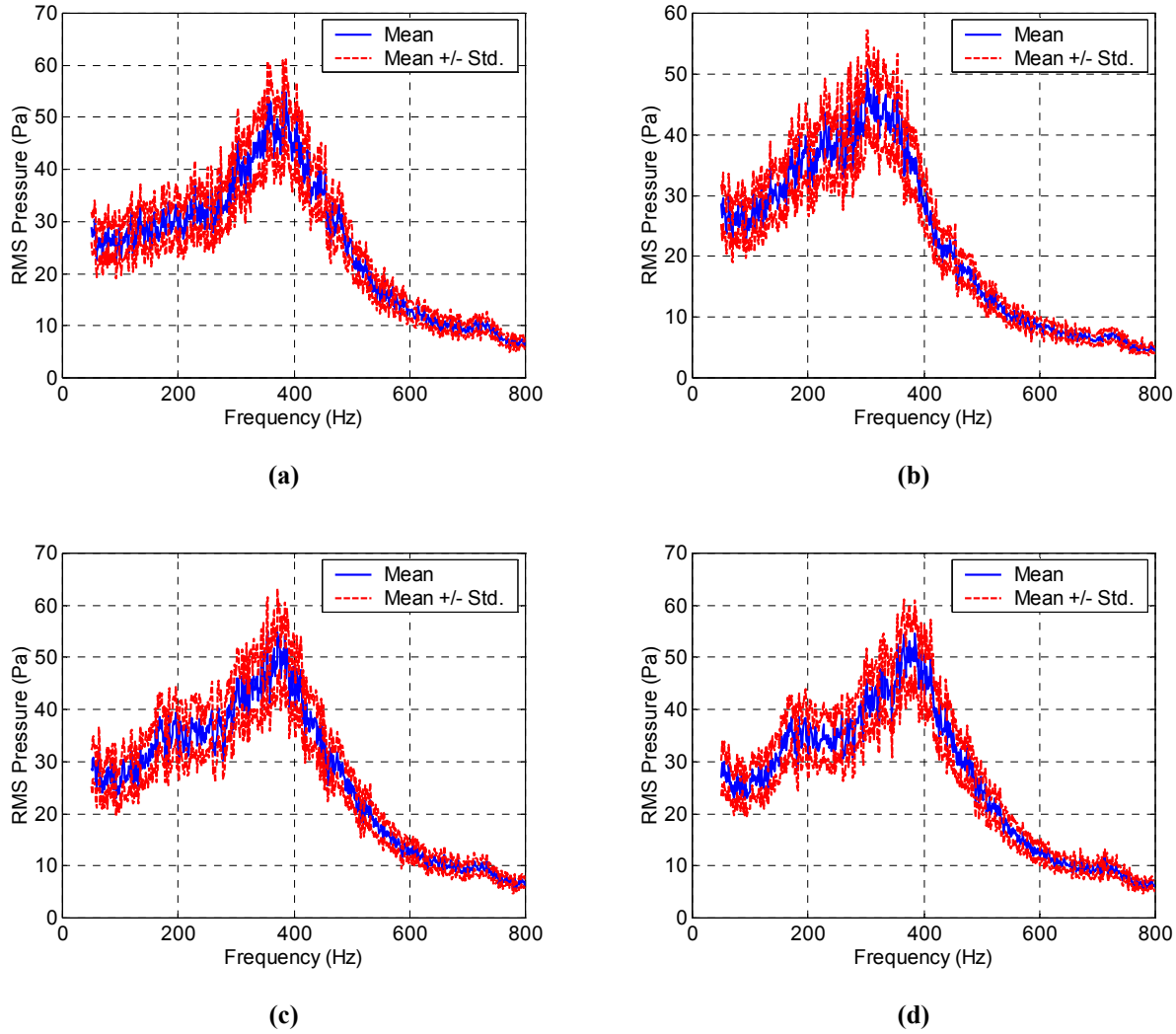

Figure B.2: Mean and Mean ±Standard Deviation RMS Pressure Spectra for No Flow Control at **(a)** 3^{o} , **(b)** 9^{o} , **(c)** 63^{o} , and **(d)** 69^{o}

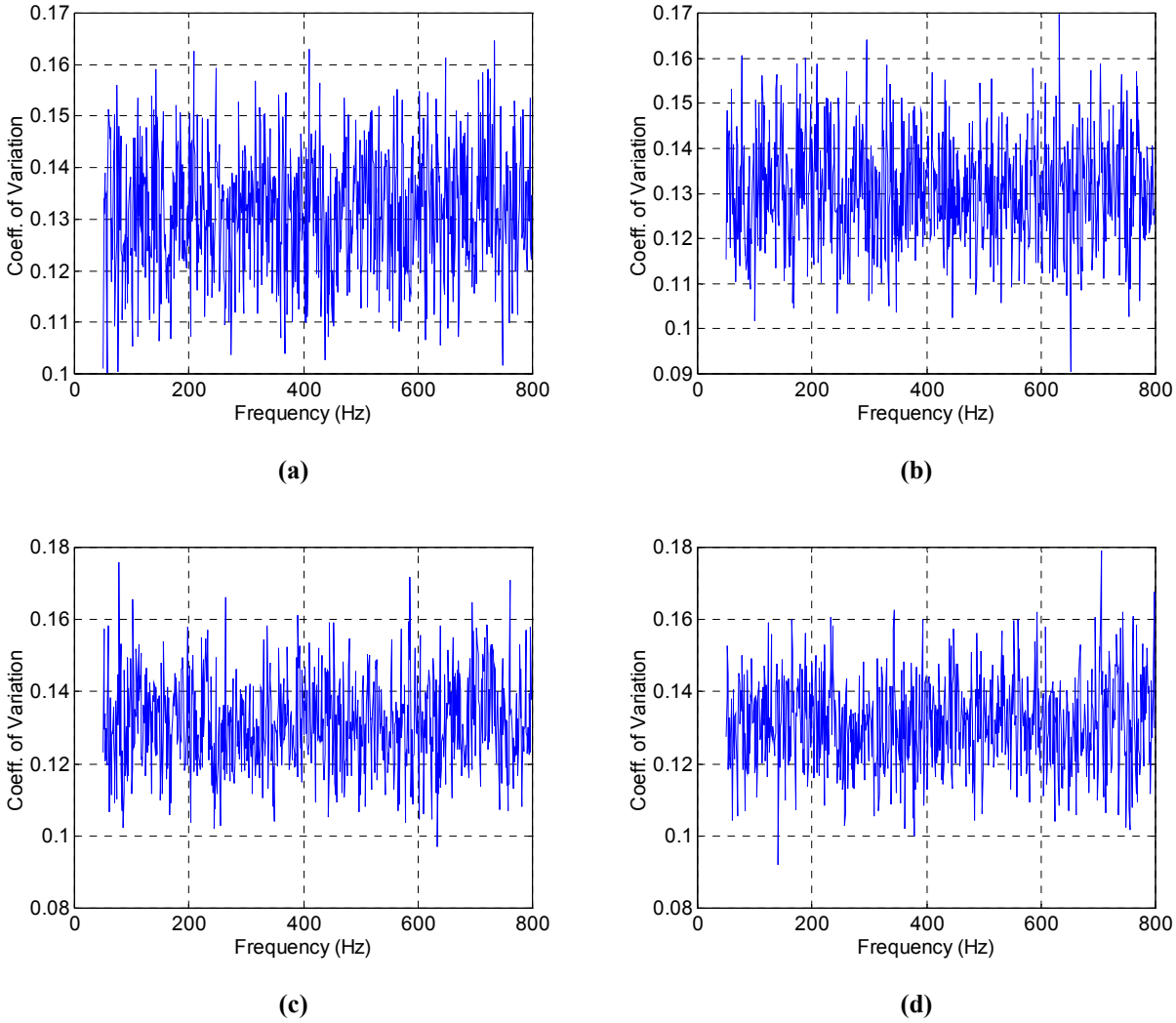

Figure B.3: Coefficient of Variation for RMS Pressure Spectra for No Flow Control at **(a)** 3^o , **(b)** 9^o , **(c)** 63^o , and **(d)** 69^o

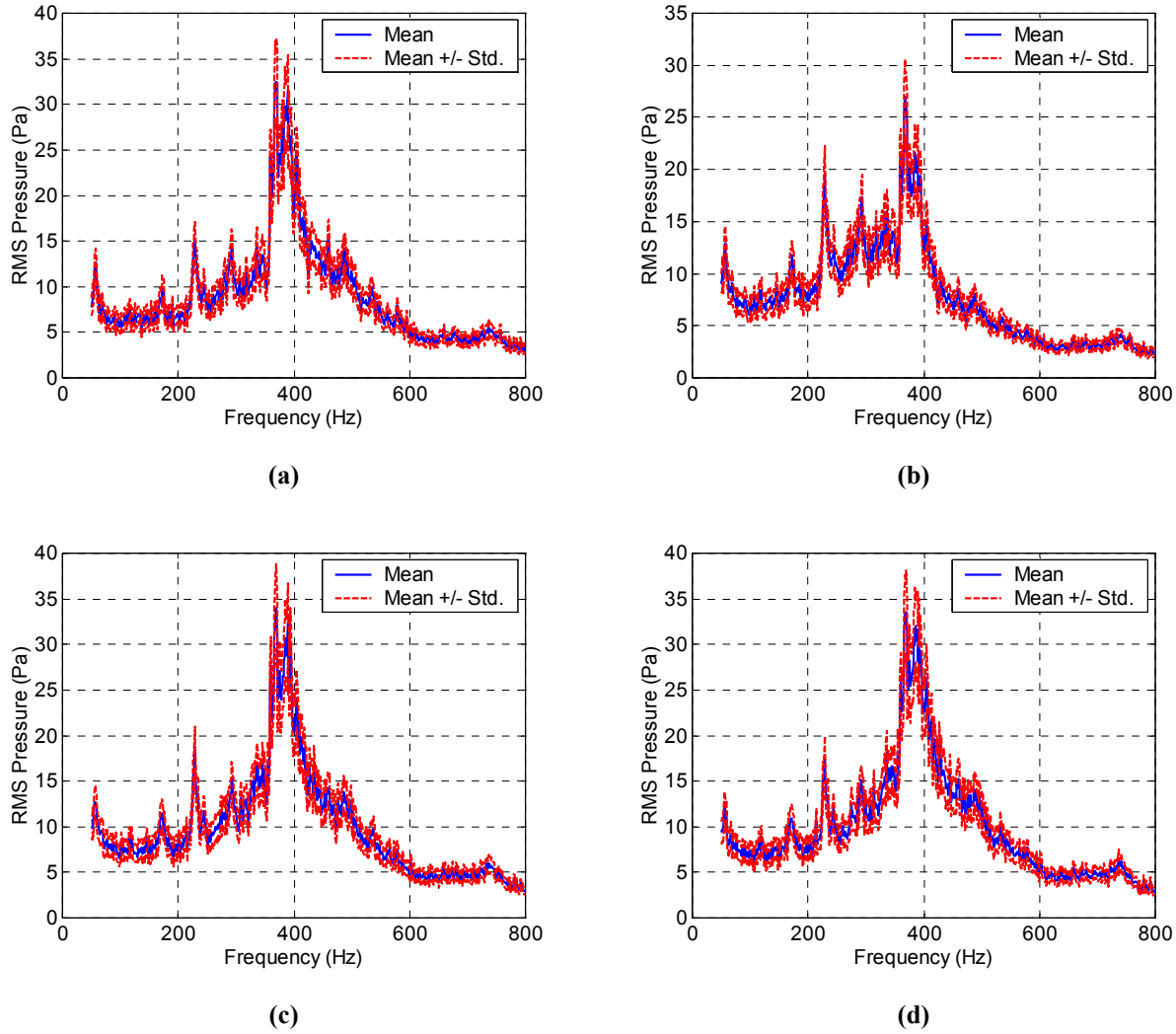

Figure B.4: Mean and Mean ±Standard Deviation RMS Pressure Spectra for 1.0% Flow Control at **(a)** 3^{o} , **(b)** 9^{o} , **(c)** 63^{o} , and **(d)** 69^{o}

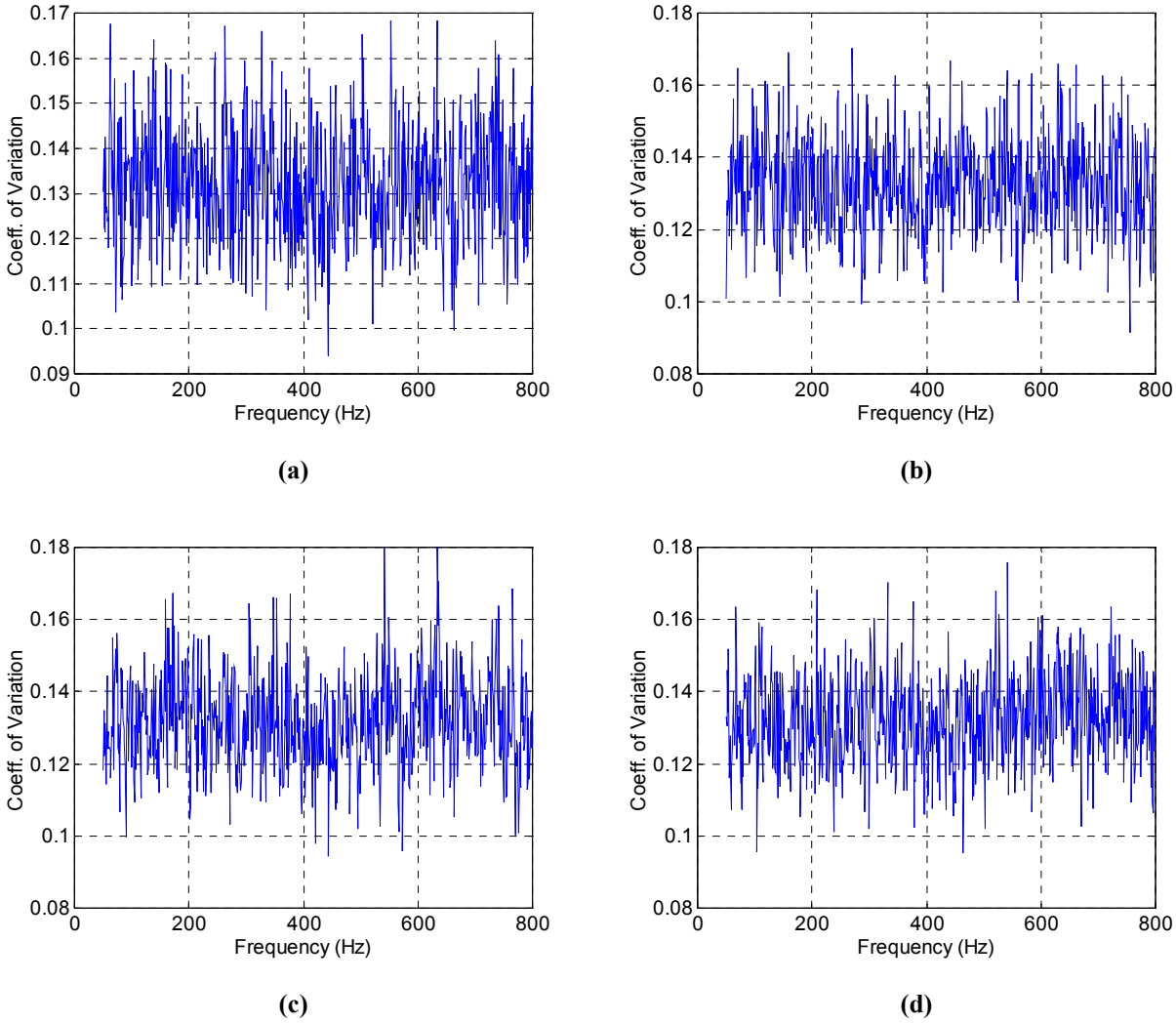

Figure B.5: Coefficient of Variation for RMS Pressure Spectra for 1.0% Flow Control at **(a)** 3^o , **(b)** 9^o , **(c)** 63^o , and **(d)** 69^o

Appendix C Spectral Results of Acoustic Filtered Measurements

Appendix C presents a comparison of the spectral results for the acoustic-contaminated and the acoustic-filtered microphone measurements that comprise the H_1 and H_2 signals in Chapter 5. This comparison shows the effectiveness of the adaptive filter network in removing the acoustic-related content from the sensors.

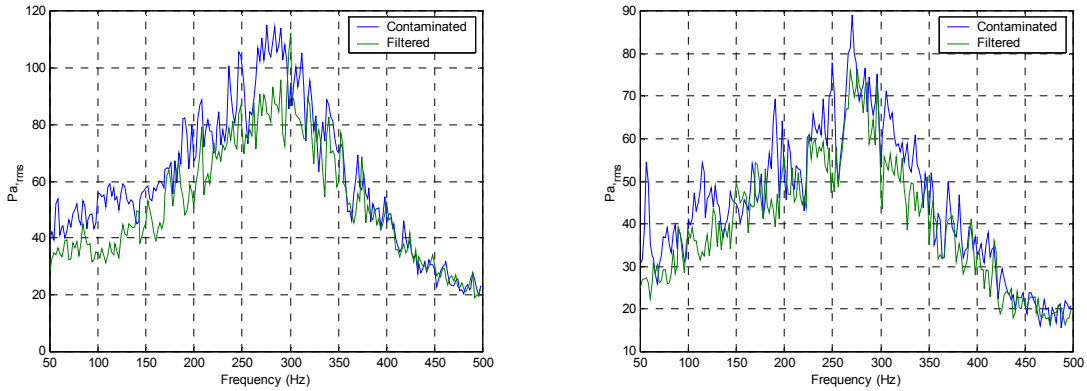

0°

12°

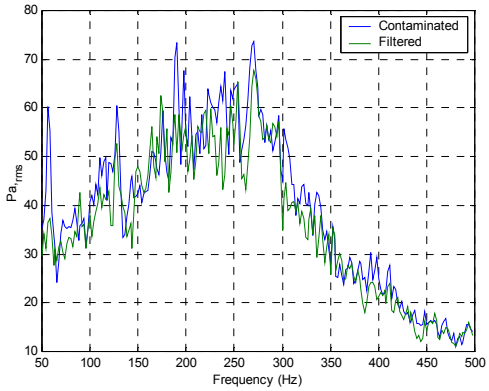

24°

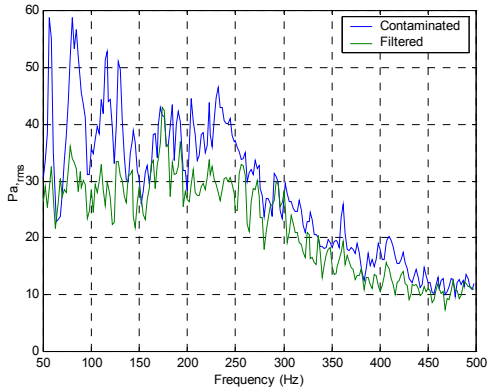

132°

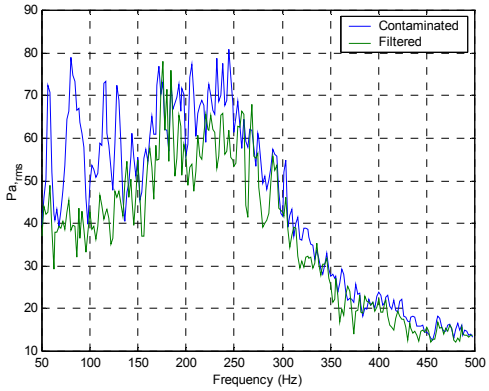

144°

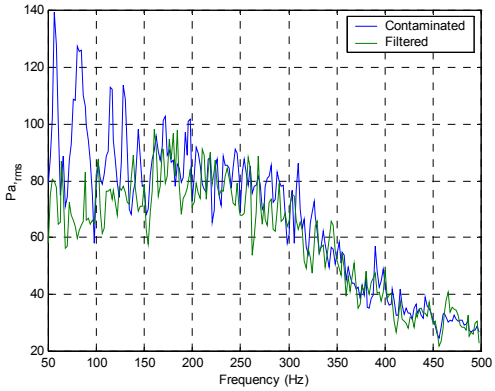

156°

Figure C.1: Comparison of Contaminated and Filtered RMS Pressure Spectra, Mach 0.7 Minimal Flow Control

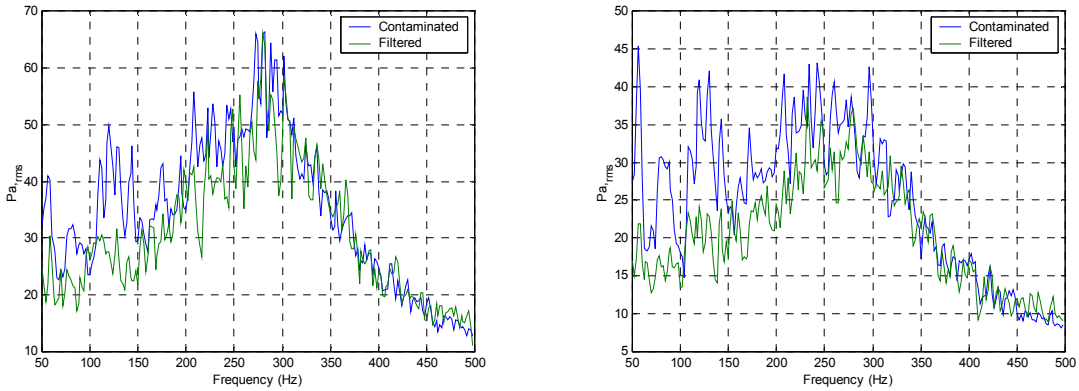

0° 12°

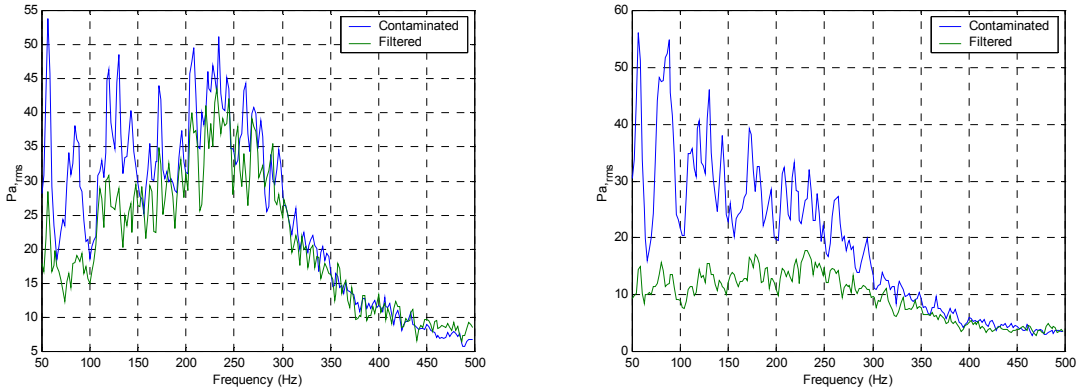

24° 132°

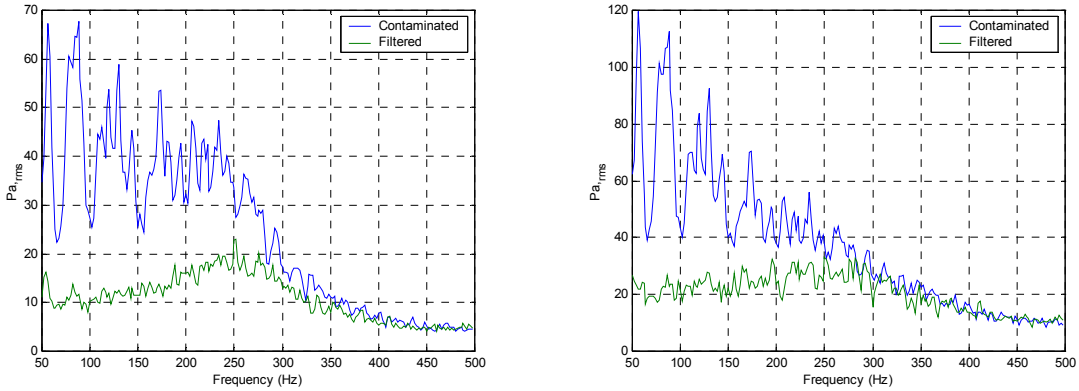

144° 156°

Figure C.2: Comparison of Contaminated and Filtered RMS Pressure Spectra, Mach 0.7 High Flow Control

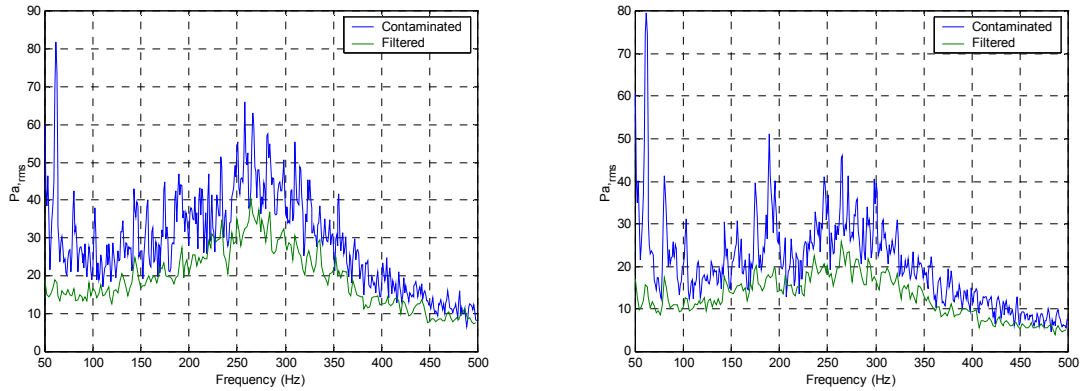

0°

12°

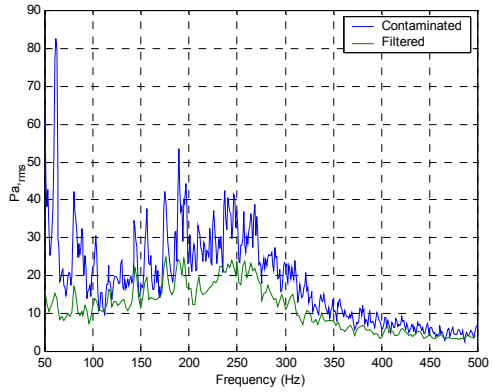

24°

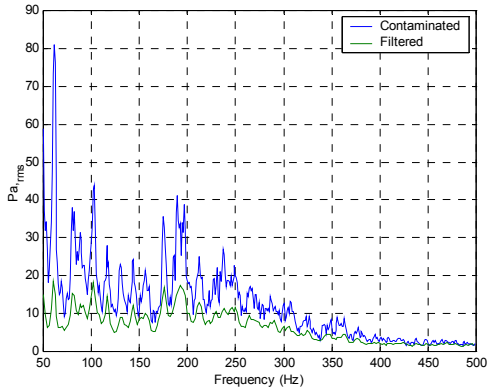

132°

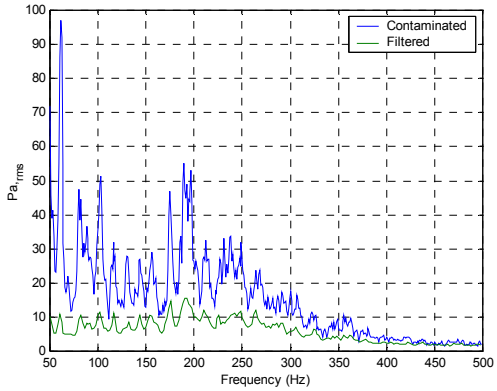

144°

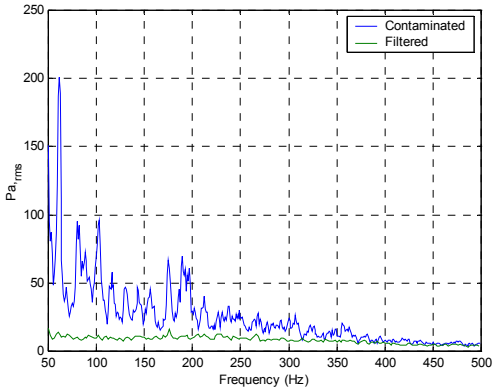

156°

Figure C.3: Comparison of Contaminated and Filtered RMS Pressure Spectra, Mach 0.5 Minimal Flow Control

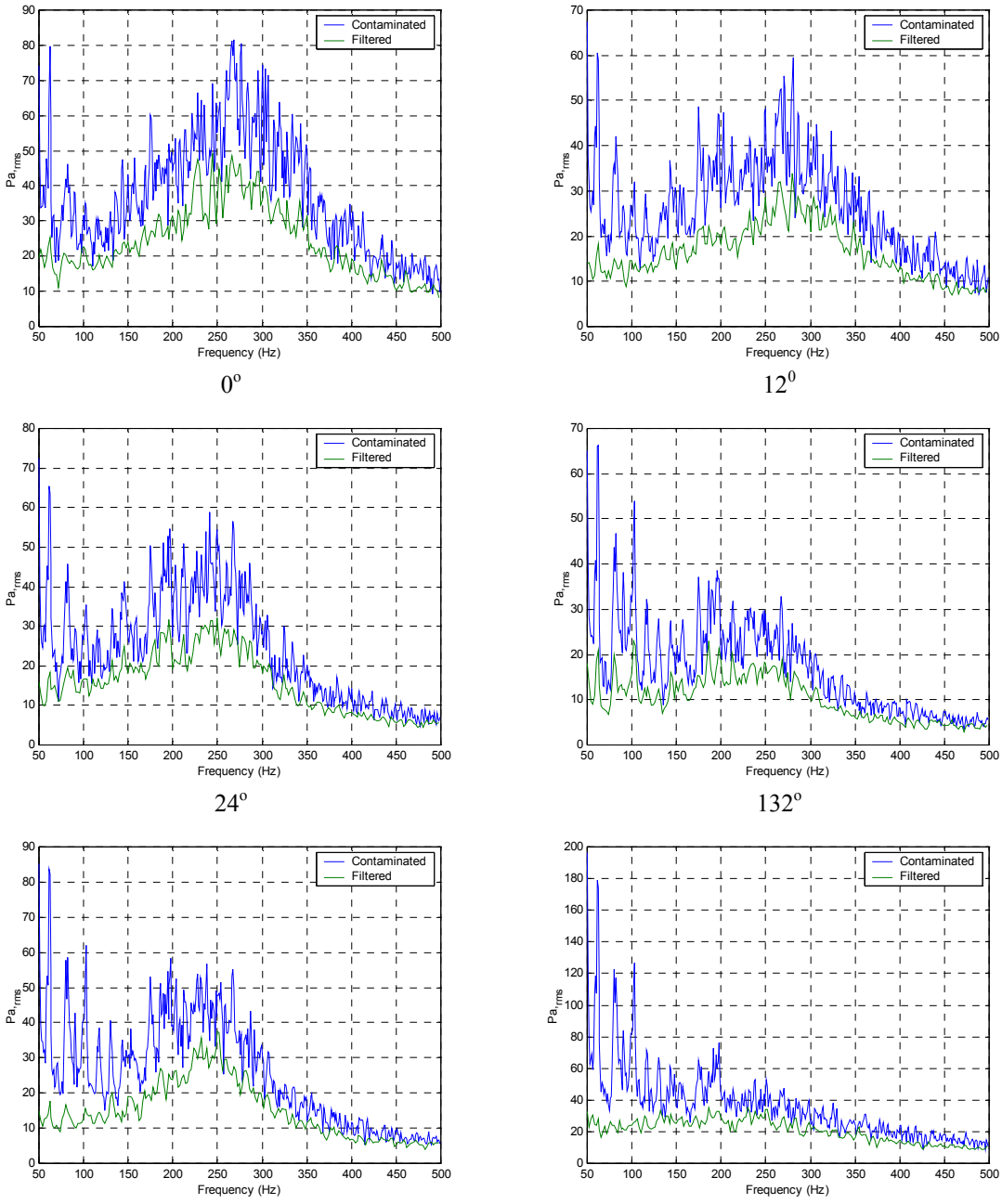

0° 12° 24° 132° 144° 156°

Figure C.4: Comparison of Contaminated and Filtered RMS Pressure Spectra, Mach 0.5 High Flow Control Effort

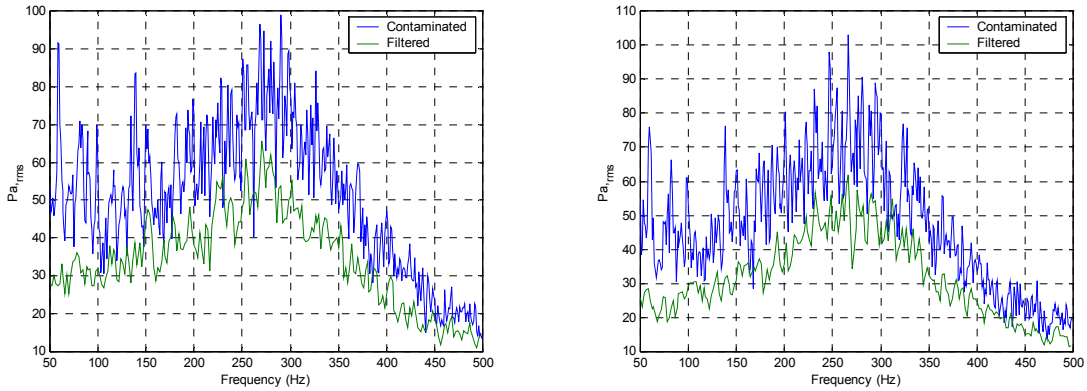

0° 12°

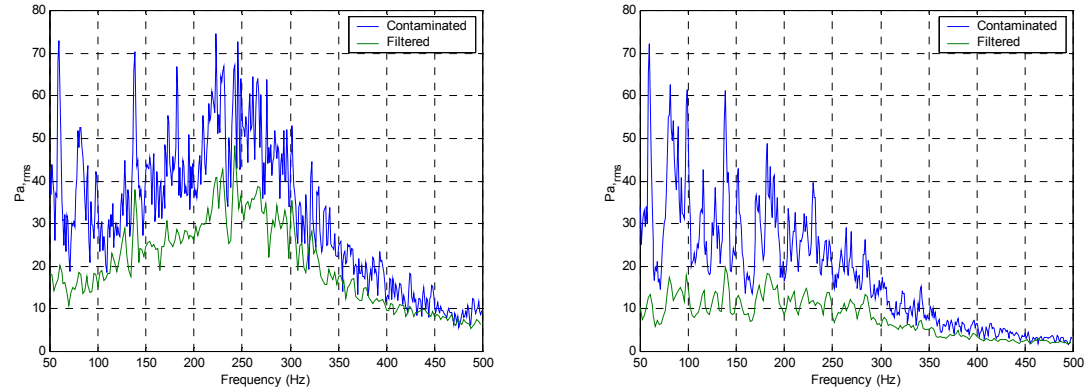

24° 132°

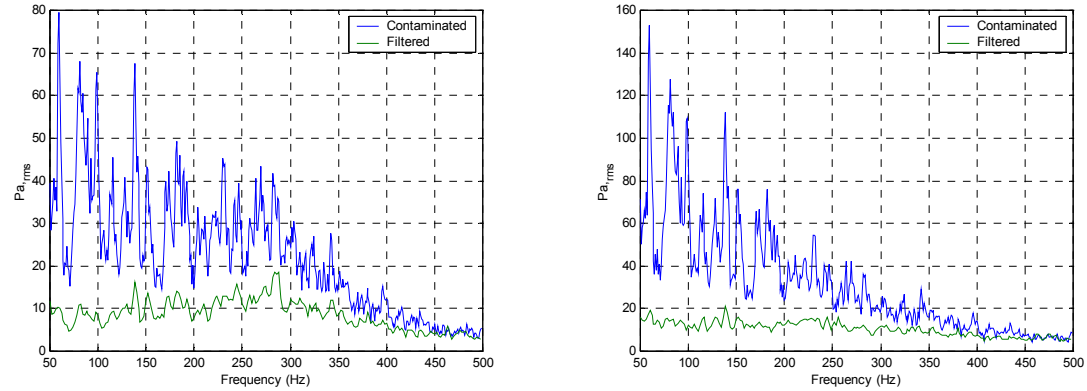

144° 156°

Figure C.5: Comparison of Contaminated and Filtered RMS Pressure Spectra, Mach 0.6 High Flow Control Effort

The remainder of Appendix C presents adaptive-filtered results from the 12-microphone array used in the research that was explained in chapters 3 and 4. The Mach 0.55, 0.8% flow control effort case was selected to illustrate the effectiveness of the adaptive filtering technique to remove acoustic background disturbances.

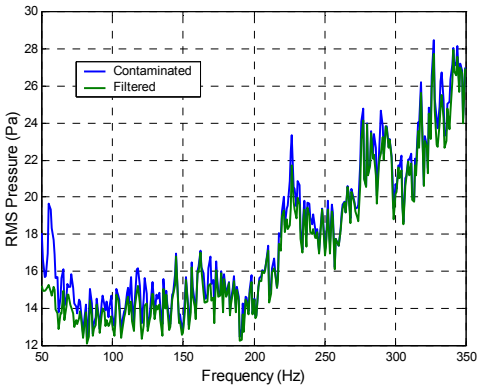

(a) 3°

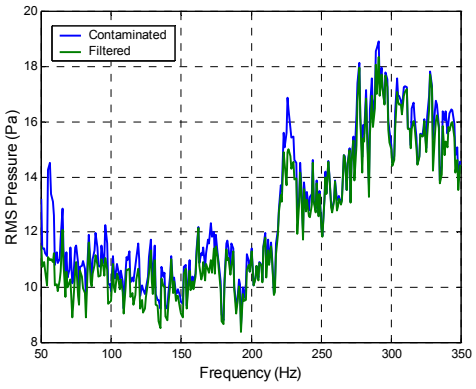

(b) 9°

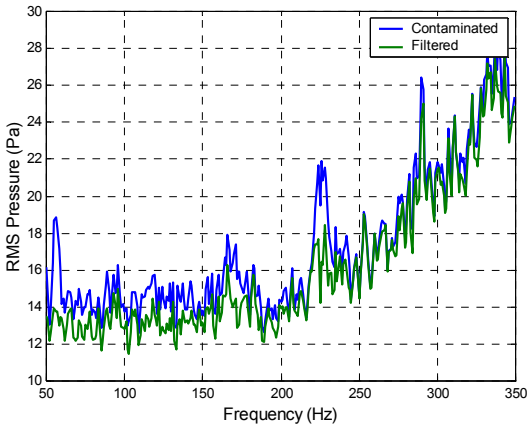

(c) 15°

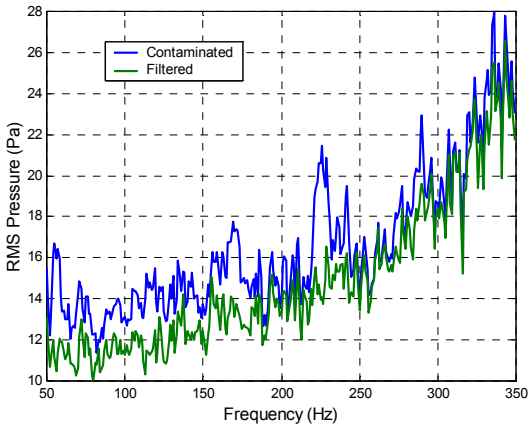

(d) 21°

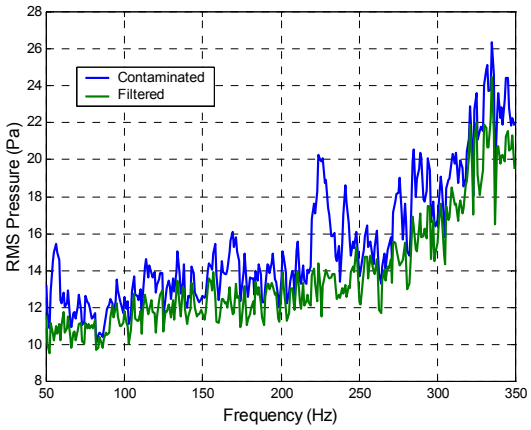

(e) 27°

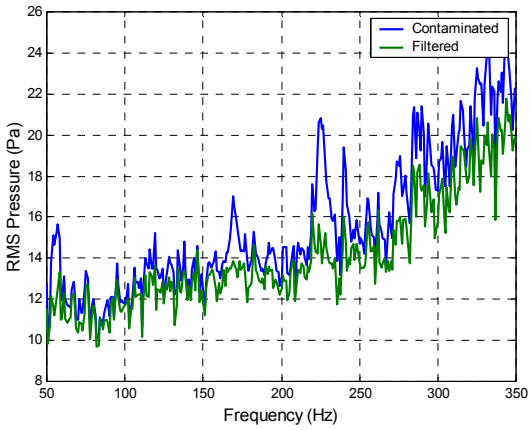

(f) 33°

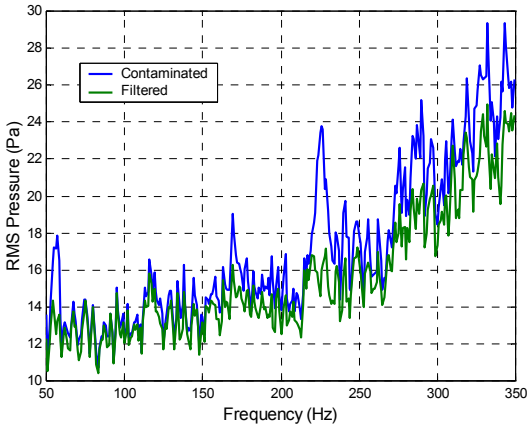

(g) 39°

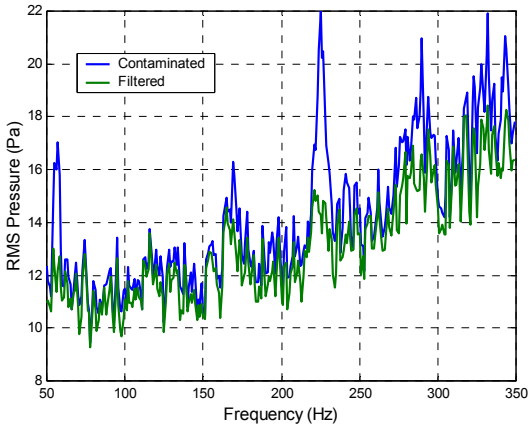

(h) 45°

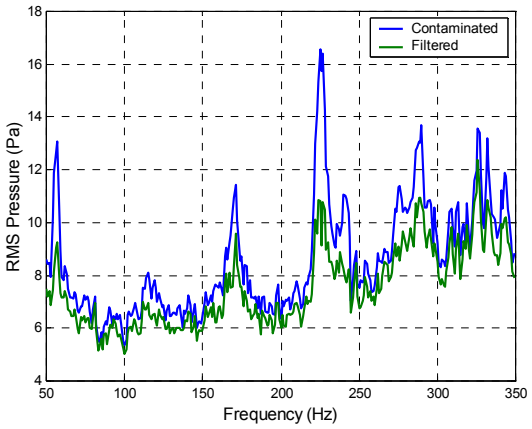

(i) 54°

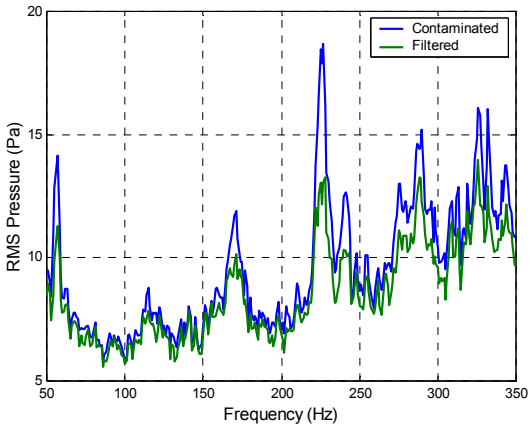

(j) 63°

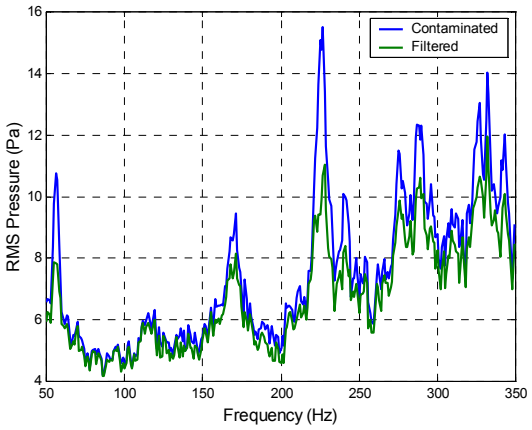

(k) 69°

Figure C.6: Comparison of Contaminated and Filtered Pressure Spectra for 0.8% Flow Control at Mach 0.55, Sensor Spacing of 48° used for Adaptive Filtering

Appendix D Optimal Sensing Results

The optimal feedback signals y_1 and y_2 are presented in Appendix for Mach numbers 0.5 and 0.6, which were not presented in the body of the dissertation.

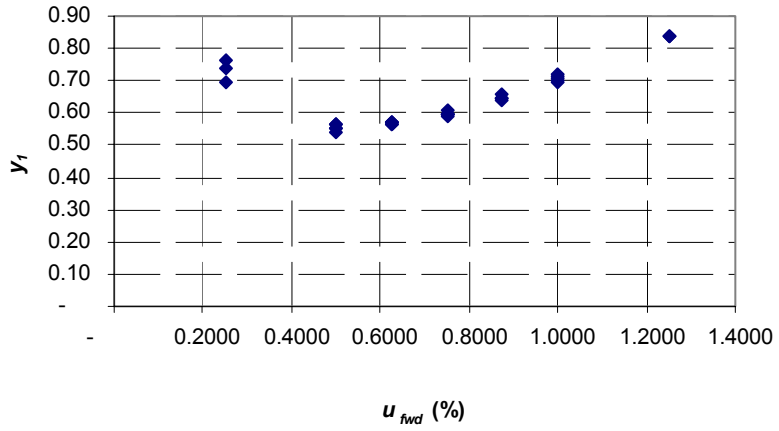

(a)

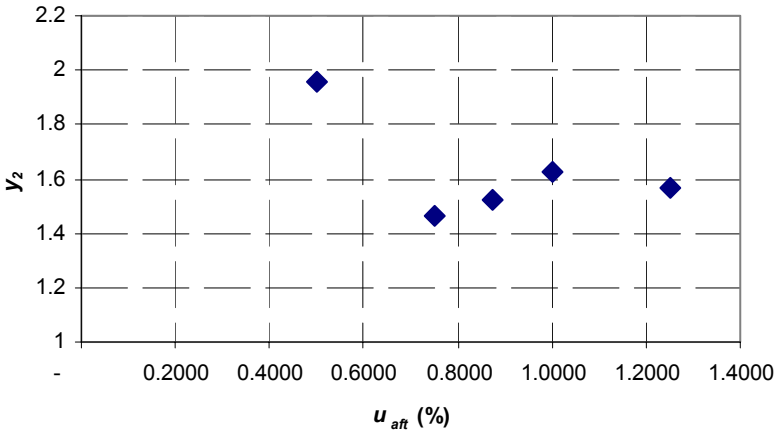

(b)

Figure D.1: Optimal Feedback Results for Mach 0.5 **(a)** y_1 vs. u_{fwd} and **(b)** y_2 vs. u_{aft}

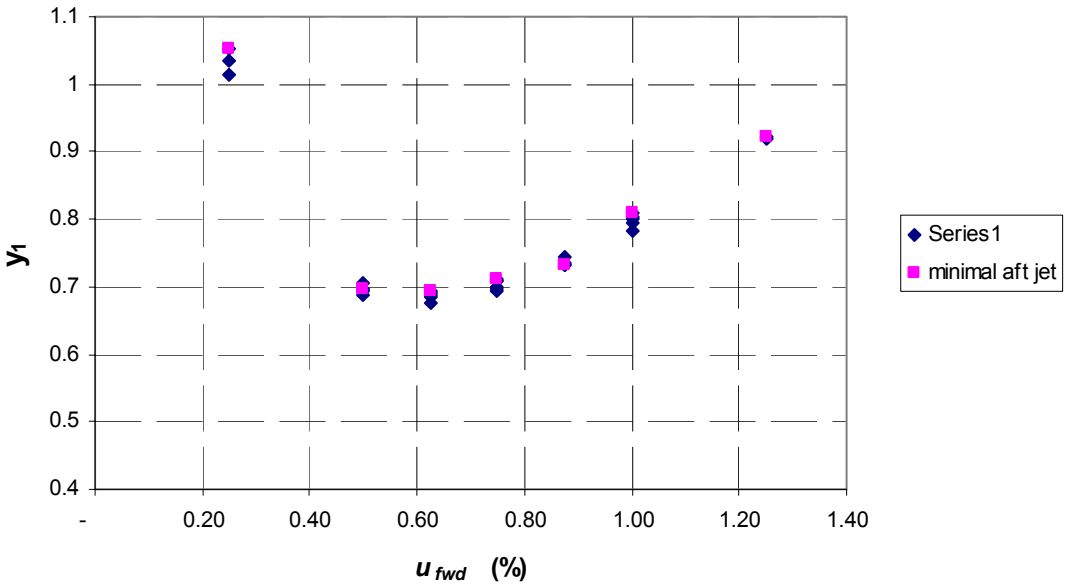

(a)

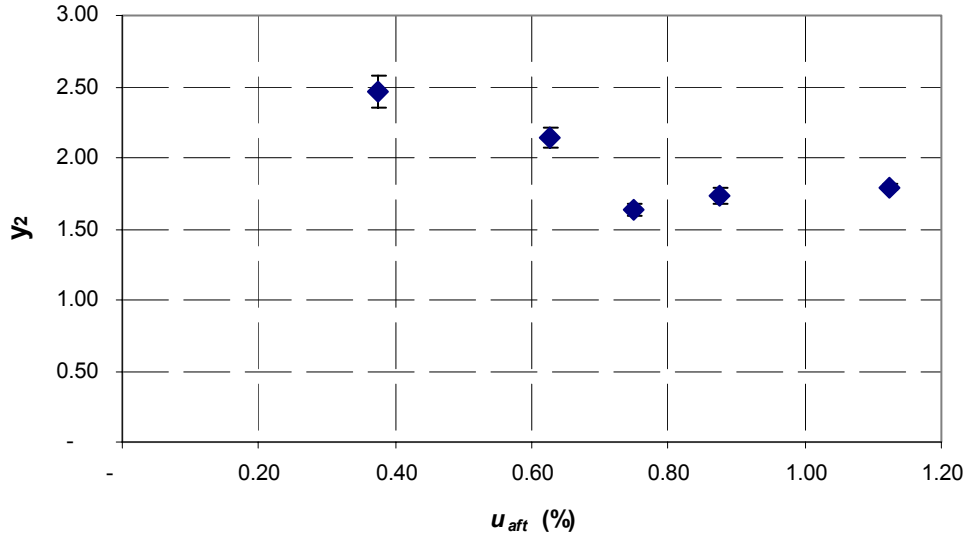

(b)

Figure D.2: Optimal Feedback Results for Mach 0.6 **(a)** y_1 vs. u_{fwd} and **(b)** y_2 vs. u_{aft}

Vita

Jason Anderson was born on March 23, 1978 in Montgomery County, Maryland. He earned his Bachelor's of Science degree in Mechanical Engineering at Virginia Tech in May 2000. Upon completion of his B.S. degree, he entered the Master's degree program in Mechanical Engineering at Virginia Tech. In 2001, Jason opted to forego a Master's degree and entered the Ph.D. program in Mechanical Engineering at Virginia Tech. His research on non-intrusive sensing and flow control in serpentine inlets yielded two conference papers. The latter paper received the best paper award in the Noise Control and Acoustics division of the ASME IMCE in November 2002. Jason is a student member of ASME and AIAA.